Department of Precision and Microsystems Engineering

Examination of large amplitude vibrations of a nonlinear oscillator for energy harvesting

S.T. Molenaar

Report no : 2021.008
Coach : T.W.A. Blad
Professor : P.G. Steeneken
Specialisation : DMN
Type of report : MSc Thesis
Date : 11 January 2021

TU Delft Delft University of Technology

Challenge the future

Examination of large amplitude vibrations of a nonlinear oscillator for energy harvesting

Examination of large amplitude vibrations of a nonlinear oscillator for energy harvesting

MSc Thesis

to obtain the degree of Master of Science
at the Delft University of Technology,
to be defended publicly on Monday January 25, 2021 at 1:30 PM.

by

Stefan Thomas Molenaar

Born in Amsterdam, the Netherlands.

Report no.	2021.008
Mentor	T.W.A. Blad
Professor	P.G. Steeneken
Specialization	DMN
Type of report	MSc Thesis
January 25,	2021

This thesis was approved by the thesis committee:

Prof.dr. P.G. Steeneken	Chairman
	DMN, PME, 3mE, TU Delft
Ir. J.W. Spronck	MSD, PME, 3mE, TU Delft
Ir. T.W.A. Blad	MSD, PME, 3mE, TU Delft

Keywords: Energy harvesting, nonlinear dynamics, large amplitude vibrations

Printed by: Repro van de Kamp

Front & Back: Stefan Molenaar

Everybody is a genius.
But if you judge a fish by its ability to climb a tree,
it will live its whole life believing that it is stupid.

Albert Einstein

Summary

Vibration energy harvesting is a promising step towards a more sustainable society. The world is getting more and more connected through electronic devices, which all require electrical energy. A battery can deliver electrical energy; however, such a battery needs to be replaced or recharged; this is where energy harvesters become interesting. Energy harvesters convert energy from ambient sources to electricity; this source can be, for example, solar or thermal energy but also vibrational energy.

Extensive research has been done in vibrational energy harvesting so far. The subject of human motion energy harvesting is increasing interest. An energy harvester for human motion can be used to power health monitoring devices. However, there is one significant problem; human motions are dominantly low-frequency with high amplitude motions, while energy harvesters tend to work better on high frequencies. A limiting factor for successful experimental research is the equipment. The lack of sufficient stroke, controlled and low-frequency excitation impede research regarding human motion. In this research, a new test setup is developed for experimental research. A linear air-bearing stage is used to reproduce the human motions with an amplitude up to 500 mm. The air-bearing stage has an incremental encoder to ensure a precision of at least 20 μm. This stage may be used for many different testing situations ranging from vibration testing to impact testing. The stage can reproduce motions that were impossible to reproduce with a shaker, for example.

The research is expanded with a nonlinear oscillator to assess its performance on large amplitude motions. A transducer can be attached to the oscillator to transduce the vibrational energy into electrical energy. By using an oscillator, the frequency is increased, causing a higher energy output at low frequencies. The dynamics of the nonlinear oscillator are numerically calculated. For which a new method is proposed to simulate the bouncing behavior in the spring numerically, called the bounce loss coefficient. The new method shows better results than the traditional model used to simulate the bouncing behavior (coefficient of restitution). The numerical model is experimentally verified on the newly developed testing setup. It was shown that using a new model for the bouncing behavior, the dynamical behavior of the nonlinear oscillator can be reproduced when excited at a large amplitude motion.

Samenvatting

Een groot hedendaags probleem is het gebruik van energie. De wereld raakt steeds meer en meer verbonden met elkaar door middel van elektronische apparaten welke vaak gevoed worden door een batterij. Deze batterij kan leeg raken en moet dan weer vervangen of opgeladen worden. Dit is waar een energiewinning door middel van externe bronnen interessant worden. Dit kan bijvoorbeeld het winnen van energie door middel van zonne-energie zijn, maar ook door middel van trillingen.

Er is al veel onderzoek gedaan naar het winnen van energie door middel van trilling. Ondertussen wordt er steeds meer en meer onderzoek gedaan naar het winnen van energie uit menselijke bewegingen. Wanneer energie uit menselijke bewegingen wordt gewonnen kan dit bijvoorbeeld gebruikt worden om een apparaatje dat toezicht houdt op onze gezondheid van stroom te voorzien. Alleen er is een probleem; het winnen van energie uit trillingen gaat efficiënter op hoge frequenties dan op lage frequenties wat vaak menselijke bewegingen zijn. Momenteel is er nog een limiterende factor in het onderzoek naar energiewinning uit menselijke trilling en dat is het tekort aan testopstellingen. Voor veel dynamisch onderzoek wordt gebruikt gemaakt van zogenaamde shakers, shakers hebben geen grote amplitude en zijn lastig aan te sturen op lage frequenties. Daarom wordt er in dit onderzoek gebruikt gemaakt van een nieuwe meetopstelling waarmee grote bewegingen kunnen worden nagebootst. De meetsopstelling bestaat uit een luchtlager welke een slag kan maken van 500 mm, met een nauwkeurigheid van minimaal 20 µm. Deze nieuwe meetopstelling kan veel verschillende condities nabootsen, van trilling tot schoktesten, metingen die voorheen onmogelijk waren.

Het onderzoek is uitgebreid met een niet lineaire veer, waarvan het dynamische gedrag wordt bepaald wanneer geëxciteerd op grote amplitude bewegingen. Op de veer kan een module worden gezet die de daadwerkelijke trillingen omzet naar elektrische energie. Door het gebruik van de niet lineaire veer, kan de grote (langzame) beweging worden omgezet in een kleinere (snellere) beweging, welke beter om te zetten is naar elektrische energie. De veer is eerst numeriek gesimuleerd, om het stuiter gedrag van de niet lineaire veer te simuleren is er een nieuwe methode geïntroduceerd genaamd de bounce loss coefficient. Deze methode toont betere resultaten dan de traditioneel vaker gebruikte methode. Het numerieke model is experimenteel geverifieerd op de nieuw gebouwde setup, waarna aangetoond is dat het dynamische gedrag door middel van de methode gesimuleerd kan worden.

Preface

If you asked me when I was young, what I wanted to be when I grow up? Probably a firefighter. What if you asked my high school mentor? He would probably be surprised that I even graduated high school. Being a more practical person than an academic, it somewhat even surprises me this thesis is here in front of you.

Engineering fascinates me since I was a young boy. It started at a young age where my grandpa took me to steam engine shows. I was intrigued by all the moving parts working together. If only one part failed, the machine would stop working, but it never did (well ... at least as far as I could judge).

At the time I went to high school, my interest in engineering increased. When anything was broken, the first thing I did was taking it apart, learning how it works, and sometimes even fixing it (or breaking it further). By doing this several times, I began to see similarities in the mechanics and started learning how it works. At this point, I learned that engineering could make my life easier. I'd rather be lazy than tired. It started with a simple system turning on the lights automatically, which extended to almost an entire home automation system.

My affinity with electronics and moving parts turned out to be a winning combination. I was able to combine both my fascination for moving parts with my knowledge of electronic systems. During this project, my knowledge was extended further, getting a closer insight into the working principles. I am grateful for the opportunities I had throughout this project. This thesis might be the closing chapter of my academic career. However, I will never stop learning because life never stops teaching.

Stefan Thomas Molenaar
Delft, January 2021

Contents

Chapter 1
Introduction

Education is what remains after one has forgotten
what one has learned in school.

Albert Einstein

In this chapter, the subject of this thesis is discussed. Starting with a brief introduction to energy harvesting, what is it, and why do we want to use it? After that, the subject of low motion ratios or large amplitudes will be discussed. Finally, the structure of this thesis is given.

1

1.1 Relevance and applications

Energy is all around us, sometimes without us even noticing. Energy can be in the form of light, sound, vibrations, or electricity. Only the last source is well known and widely used. The electrical grid provides almost every household with electrical energy. Energy is generated on a large scale by power plants, dams, nuclear plants, solar panels, or windmills. All these energy sources have one thing in common; they turn an alternative energy source into electrical energy. However, not everything can be connected to the electrical grid; this can be, for example, remote places, but this can also be devices that you do not want to be wired (for example, a mobile device). Therefore we make use of batteries.

Batteries are small energy storing devices, which can be divided into two main categories: rechargeable and single-use cells. Wearables and smart devices often use rechargeable batteries. Low energy consumption devices often use single-use batteries since they are cheaper than rechargeable ones. Changing a remote battery is rather annoying, but replacing a battery can also be costly or even dangerous. Replacing a battery in a remote place would require a worker to go there and switch the cell. While the battery only costs a small amount of money, the entire operations cost a lot more. Sometimes it is even cheaper to swap the device as a whole (including the battery) instead of only the battery.

It is sometimes even more expensive for medical applications to replace a battery, take, for example, a pacemaker. Pacemakers have a single-use battery, which needs replacement after around 7-10 years. Replacing the battery is a dangerous and costly operation. Thus arises the question, is it possible to generate electrical energy using the ambient energy sources from human motions.

The human body transduces lots of energy from, for example, food to motion. This motion can be the swinging of the arm, to walking, to the beating of the heart. The human motions with the highest amount of energy are often the large motion amplitude; thus, the walking, swinging of the arm, and other large motions. If there is a way to convert these motions into electrical energy, the energy could be used for medical applications (sensors, pacemakers) and wearable devices. Such an energy harvester would remove the need ever to change the battery of a pacemaker.

This research's primary focus is to investigate the dynamics of energy harvesters when excited at large motions. One possible solution for harvesting energy from large motions is by using a nonlinear oscillator. Such a nonlinear oscillator has two stable states. Due to the snapping between the two stable states, more energy can be generated. First, a brief introduction to the design process of an energy harvester will be given.

1.2 Turning vibrations into energy

When turning vibrations into energy, it is essential to analyze the system and generate design requirements. One crucial design parameter is the dimension of the energy harvester. It is way easier to design an energy harvester with a large volume instead of a small volume. Blad et al. [6] described a relation between the dimension of the energy harvester and the amplitude of the displacement signal; this will be discussed more in-depth in section 1.3.

The dimension of the energy harvester is also crucial in picking a transducer. The transducer converts the kinetic energy into electrical energy, which will be discussed next.

1.2.1 Transducer

There are two common ways to turn vibrations into electrical energy. The first and most well-known way is using magnetic induction. An electromotive force is induced by varying the magnetic field (the magnet moving through the coil). This system is widely used in large scale applications (the most well-known example is a generator) but is rather hard to use on the MEMS scale.

The second option for a transducer is a piezoelectric element. The working principle is called the direct piezoelectric effect, a reversible process (electric energy can be converted into mechanical and vice versa). By resonating with the piezoelectric element, mechanical stress is induced that generates a charge in the piezoceramic layer. The main advantage of using piezoelectric elements is the ability to downsize. However, the downside of a piezoceramic material is the higher resonating frequency.

The piezo ceramic transducer works best when excited on higher frequencies (where the maximum amount of energy is reached at the transducer's eigenfrequency). However, these frequencies are often in the range of 100 Hz and above. This research focuses on energy harvesting for human motion; the human motion often has a large amplitude; however, with low frequencies. The beating of the heart, for example, is between 1 and 2 Hz. Walking is also around the 2 Hz region (100-130 steps per minute). At this point, the nonlinear spring comes into play. The nonlinear spring is used as an oscillator for the large amplitude motions.

1.2.2 Oscillating mechanism

The oscillating mechanism is used as a frequency upconverter; the input frequency is the frequency of the human motion; the output vibration is the frequency to which the transducer is excited. A frequency up-converter has several use cases; it increases the frequency at which the transducer resonates, and it makes it possible to vibrate longer at impacts. A frequency up-converter is based on multistability. A multistable system has more than one stable point and tends to have low stiffness, making it easy to snap between stable points. When the system is impacted, the frequency up-converter starts resonating with the electrical transducer attached to it. One way to induce multistability is by prestressing a flexure, which causes it to buckle. The simplest form is bistability, which can be thought of as a buckled beam. When the buckled beam is pushed through its unstable point, it will snap towards the other side. The multistable system has complicated dynamics, which makes it hard to find the performance of the system. This research tries to find the dynamics of such a nonlinear oscillator.

1.3 Low motion ratio

This research's primary focus is to investigate the dynamics of nonlinear oscillators when excited to large motions. Blad et al. [6] introduced the term motion ratio as a metric for quantifying the internal displacement limit relative to the applied displacement. The motion ratio (see Eq. 1.1) describes the relationship between the driving motion amplitude and the dimension in the driving direction. There are two ways to create a low-motion ratio energy harvester by decreasing the driving motion dimension or increasing the driving amplitude. This research focuses on increasing the driving amplitude, which results in low frequencies (around 1 Hz).

$$\lambda = \frac{L_z}{2Y_0} \tag{1.1}$$

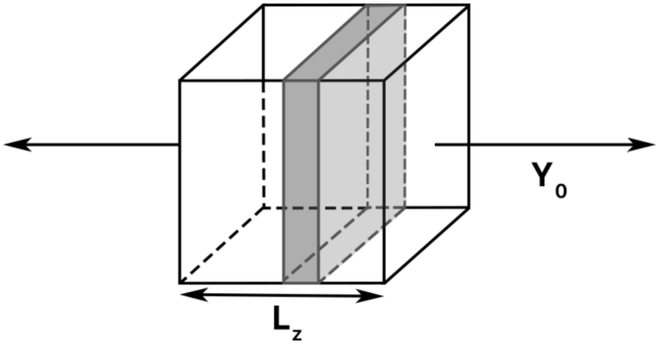

Figure 1.1: Imaginary generator with a certain motion ratio, where L_z is the dimension in the driving direction and Y_0 is the amplitude of the driving motion, the mass (indicated in dark grey) is able to move within L_z.

The first step is to create a numerical model that can simulate a nonlinear oscillator's behavior when excited on large-amplitude vibrations. Experimental testing for such large amplitude motions was almost impossible before. Small amplitude oscillators are tested on shakers, which are limited to an amplitude of around 20 mm. To experimentally test, a novel test setup is used to test with amplitudes up to 250 mm.

1.4 Thesis outline

This research focuses on investigating the dynamics of a nonlinear oscillator when excited to large amplitude motions. This investigation is done by first looking at the numerical model and the governing equations of motions. Next, a setup is investigated, set, and verified to test for such large amplitude vibrations and lastly, the numerical model found in the beginning is expanded to simulate the bouncing behavior and verified by testing an experimental model in the test setup. This thesis's goal is formulated as: "Investigate the dynamics of an oscillator when excited to large-amplitude vibrations.".

The second chapter of this thesis presents a guide on simulating energy harvesters; this was part of the literature phase and extended further with optimizations. When simulating energy harvesters, some significant side-effects begin to play a role that needs to be considered. By performing this step, broader knowledge of energy harvesters was gained.

The third chapter describes the linear air-bearing stage, which was built to verify the nonlinear oscillators' behavior experimentally. A lot of time and effort went into getting the stage to work. A short chapter was written looking into the working principle and the stage's dynamic behavior after that.

The fourth chapter combines the numerical model with experimental testing on the air bearing stage. A nonlinear oscillator is chosen from which the mechanical behavior (force-deflection curve) is known. To simulate the dynamical behavior of the oscillator a new method is introduced to simulate the bouncing behavior; the bounce loss coefficient. The dynamics and the newly added method are then verified using experimental data.

The fifth and final chapter concludes the research done throughout this master thesis. It also discusses the personal process and the personal study goals learned throughout this research.

The appendices are split into two main subjects; the first five appendices are mainly focused on the air-bearing stage. The following three chapters are mainly focussed on simulating the nonlinear oscillator. The first appendix (App. A) describes the working principles of the components used in the stage. Appendix B focuses on the safety features used in the stage to ensure a safe working environment. After that, the software setup in the servo driver is discussed in appendix C. Since there was insufficient documentation on the air-bearing stage, appendix D is added to describe the electrical wiring used in the stage and the added components. To conclude the stage, a how-to-use guide was added in appendix E. Appendix F describes how the simulation of the two different load paths is performed. During the simulation, damping became a critical issue; therefore, appendix G was added, describing all different damping kinds. Finally, appendix H) was added, showing the results when influencing the design parameters of the oscillator.

Chapter 2
Multistable energy harvester performance estimation based on mechanical properties

When you want to know how things really work,
study them when they're coming apart.

William Gibson

In this chapter, the literature study is shown in the form of a paper. The literature study's goal was to investigate the effects of a nonlinear spring used for energy harvesting. A numerical model is constructed for a dynamical system that is excited to forced vibration. The influence of a nonlinear spring and transducer parameters on the output energy are found and discussed.

Multistable energy harvester performance estimation based on mechanical properties

S.T. Molenaar, T.W.A. Blad and P.G. Steeneken

2

Abstract

A lot of research is done in nonlinear energy harvesters, requiring a lot of experimental testing to check whether a design performs well. This research focuses on how well a system can be simulated using only the mechanical properties which are easy to measure. The research focuses on 3 side effects; hardening/ softening, damping and electromechanical coupling. The use of a softening spring is advantageous over a hardening spring since it brings a wider frequency bandwidth which tends to lower frequencies and has better performance under white noise excitation. The lack of a damping factor causes problems on estimating the performance looking at the power output, however an estimation can be made on the bandwidth of the system. The electromechanical coupling factor brings extra damping and is also crucial to the system, when the damping factor is too low it will not use the full potential of the system. When the coupling factor is too high it will cause too much damping losing its nonlinear properties and increasing the resonance frequency. It is hard to give an appropriate estimation of the performance of an energy harvester knowing only the mechanical properties. The lack of damping and electromechanical coupling factor will bring an uncertainty in the system which causes the user not to know whether the system is in the linear or nonlinear regime, which affects the power output tremendously. However, a rough estimation of the bandwidth can be made.

Keywords

Energy Harvesting, nonlinear dynamics, forced vibrations, multistability

2.1 Introduction

Over the last couple of years, research interest has gained in energy harvesting devices [23]. The use of energy harvesting devices allows the user to scavenge energy from ambient vibration sources. While ambient vibration sources are often low power energy sources [8], they allow harvesting energy in places where energy might be scarce. This can be, for example, a sensor to monitor the movement of a bridge [4]; traditional sensors would require a battery to power the sensor; however, since a battery has a limited lifetime, it needs to be replaced, which is labor-intensive and therefore an expensive process [34]. Real-life vibrations are often low-frequency high-amplitude vibrations, which are rather hard to harvest [18]; therefore, low frequencies are converted to higher frequencies using a frequency up converted which are then converted into electrical energy using a piezo element or magnets and coils. This research focuses on the use of piezo electric elements due to their efficiency at small scale [38]. Frequency up-conversion mechanism often consist of nonlinear springs [13] (based on multiple magnets or buckled structures). Tremendous work has been done by researchers on bistable systems [22] [40] [49] but also on higher-order stable systems, for example tristable [32], quadstable [52] or even up to pentastable systems [51] with the attempt to increase efficiency.

Early research focuses primarily on bistable mechanisms based on magnets, only in the last few years research interest has gained in mechanical based nonlinear springs (often buckled beams) [13]. Much research is done in compliant nonlinear springs [11], which has potential to be used for nonlinear energy harvesters as well. However, this research focuses purely on the mechanical properties of the spring rather than the dynamical behavior. The use of compliant systems also bring the ability to downsize the system significantly making it suitable for microsystems [1]. To estimate the performance of energy harvesters, both theoretical and experimental research is performed. Experimental work requires a lot of testing, time and specialized equipment; it is rather hard to test a new type of frequency up converter using a different nonlinear spring. It would be way more time efficient to use dynamical simulations before testing on a prototype. Dynamical simulation also brings the ability to adjust different parameters to get a better understanding of the system. However, there is no clear guideline in theoretically finding the performance, especially when side effects such as hysteresis and nonlinearities begin to play a role. The goal of this research is thus to find the techniques used to simulate a energy harvester using a frequency up-conversion mechanism based on nonlinear springs.

This research summarizes the techniques used to estimate the performance and dynamical behavior based solely on the mechanical properties of a nonlinear spring. First, the base model based on a mass-spring-damper model will be elaborated in 2.2, then three side-effects will be investigated (hysteresis, damping and electromechanical coupling), the resulting behavior due to the side effects will be shown in the results (see section 2.3), which will be elaborated in the discussion afterward.

2.2 Methods

To describe the dynamical system, a forced mass-spring-damper model is used; the system thus consists of a mass, spring and a damper to which an external force is applied. The spring (F_s) is modeled as a force that is displacement dependent (see eq. 2.4), since it is a nonlinear spring, Hooke's law does not apply. The mechanical damper (F_d) is given as linear damping; therefore, there is a constant damping factor; the effect of damping will be elaborated in section 2.2.2. The last force is the electromechanical coupling (F_{em}) , which relates the motion to the output voltage by a piezo element [16]; this can be seen as a nonlinear damper which is dependent on the output circuit. The system is forced by an input force (F) or acceleration; in this case, a sinusoidal wave with a constant acceleration is used as an input. A generic model is given in figure 2.1.

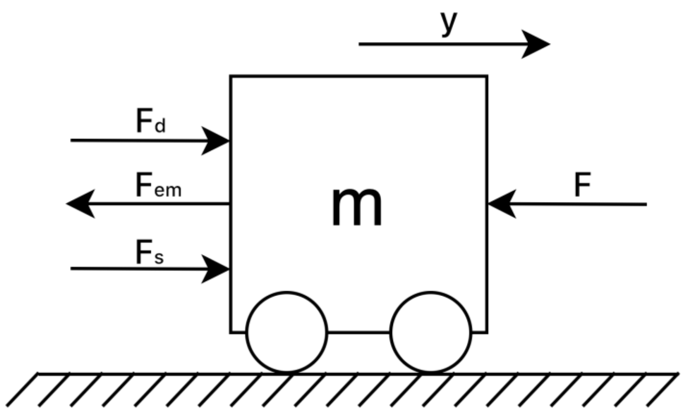

Figure 2.1: Schematic model of the system, showing the forces used for the equations of motion.

2

Now that the system is simplified into a physical model, the equations of motion of the system are found [39]. The equations of motion are found below where m is the mass of the vibrating mechanisms, y is the displacement of the tip, c is the mechanical damping factor, F_s the spring force, θ the electromechanical coupling coefficient, v the voltage over the piezoelectric element, Z_0 the amplitude of the base displacement, ω_0 the base frequency, C_p the equivalent capacitance and R the load resistance of the attached electrical circuit. Where:

$$F_d = c\dot{y}(t), F_{em} = \theta v(t), F = mZ_0\omega_0^2\cos(\omega_0 t) \tag{2.1}$$

$$m\ddot{y}(t) + c\dot{y}(t) + F_s - \theta v(t) = mZ_0\omega_0^2\cos(\omega_0 t) \tag{2.2}$$

$$C_p\dot{v}(t) + v(t)/R + \theta\dot{y}(t) = 0 \tag{2.3}$$

Throughout this paper, each side effect (hysteresis, damping, and electromechanical coupling) will be discussed, the resulting dynamics of each side effect will be discussed in the results.

2.2.1 Hardening/ softening effect

The hardening/ softening effect is dependent on the type of nonlinear spring. In this paper, the spring-force is assumed to be a third order polynomial (see equation 2.4). However, it can be taken as any nonlinear function which can be fitted from a force-deflection curve. To discuss the difference between a linear-, hardening- and softening spring, the force deflection curve will be shown first. When looking at equation 2.4, there are 2 terms, the linear term (α) and the nonlinear (β) term. When the nonlinear term is zero ($\beta = 0$), it is a linear spring (see fig. 2.2). However, when the nonlinear term is larger than zero $\beta > 0$, it becomes nonlinear with a hardening effect. When the nonlinear term is smaller than zero $\beta < 0$, it becomes nonlinear with a softening effect. The hardening/ softening can be best described by the stiffness curve (see figure 2.2b). In the case of softening the stiffness decreases when moving away from the origin, in the case of hardening the stiffness increases when moving away from the origin.

$$F_s = \alpha x + \beta x^3 \tag{2.4}$$

The hardening and softening effect can be seen in the difference between frequency up- and down sweep in the displacement amplitude due to nonlinearities [39]; this will be discussed in the results. To create a frequency upsweep, the simulation is started at the lowest base frequency and simulated until a steady-state is reached. The next simulation step is performed using the final state as initial parameters; however, this time, the base frequency is increased. This process is performed until the final frequency is reached. The same process is performed for a frequency down sweep; only this time, the first frequency is the highest frequency. In the results 3 different plots will be shown for the normalized tip displacement (this result has indirect relation to the output voltage). The result will be plotted for a linear, a hardening and a softening spring. For the nonlinear springs an up and down sweep will be performed which will be plotted in the same figure. The unstable region (dotted line) is fitted between the 2 final states.

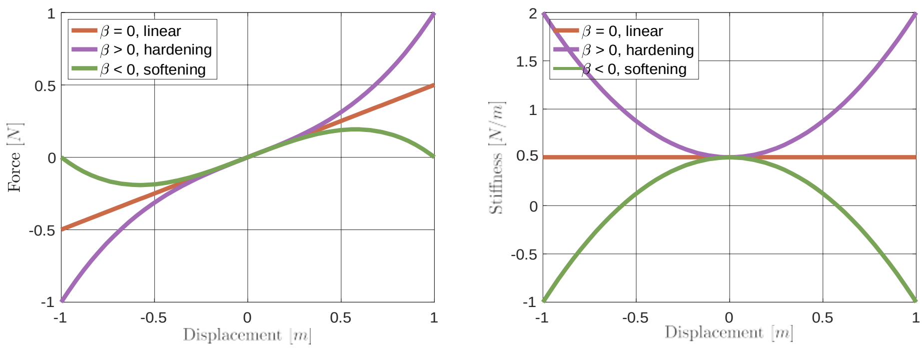

(a) Force displacement curve

(b) Stiffness displacement curve

Figure 2.2: Normalized stiffness and force-deflection curves for different types of imaginary springs (linear, nonlinear hardening and nonlinear softening)

2.2.2 Damping

One of the most critical factors of dynamically simulating an energy harvester is the damping factor [12]. The damping factor is a constant parameter that is used to find a compromise between bandwidth and power output. When a linear system is highly damped, it will cause a broader bandwidth with lower peaks, when the system is damped very little, it will cause a narrow bandwidth with higher energy peaks [10]. The amount of damping thus has a direct relation to the type of signal; it is important to know the primary goal of the energy harvester. When the system needs to be very effective in a small region, low damping might be preferred, however when the system is used for a wide bandwidth, higher damping be used.

However, damping is bound to material properties and the geometry of the system, the question arises: what is a fair assumption for damping when the parameter is unknown and how will this affect the end result? Dynamic simulation is run for several damping factors to see how damping affects the energy output and the dynamics of the system.

2.2.3 Electromechanical coupling

An energy harvester has no purpose without its piezoelectric element. The piezoelectric element converts vibrations (kinetic energy) into electrical energy. The piezoelectric elements also adds damping due to the presence of a resistor [46] and stiffness due to the capacitance; therefore, equation 2.3 is used [39]. As can be seen from the equation, there are three relevant parameters. The first is the electromechanical coupling (θ); this parameter describes how strong the connection between the system and the piezoelectric element is. The second parameter is the equivalent capacitance (C_p); this is caused by the piezoelectric itself and the output circuit which is attached and adds stiffness to the system. The last parameter is the electrical load of the attached circuit (R) which adds damping to the system. Every energy harvester has an optimal performance at some electrical resistance. Most often, the electrical resistance is determined by trial and error due to its complex dynamical behavior [44]. Therefore, the load is varied until an optimal voltage is found. The effect of the electromechanical coupling factor (θ) on the dynamics of the piezoelectric element with constant resistance (R) and equivalent capacitance (C_p) will be discussed in the results.

2.3 Results

In this section, the resulting effect on the dynamics of each side-effect will be shown. The impact of the side effect on the performance will be discussed as well. The impact of each side effect on the overall performance will be discussed to elaborate whether it is possible to make a good estimation of the overall performance.

2.3.1 Hardening/ softening effect

The effect of 3 different types of springs can be seen in figure 2.3. The value for α (linear stiffness) is taken as a constant value. The value for β (nonlinear stiffness) is tuned for 3 different cases, 0 for the linear case and a constant negative and positive value for the nonlinear case. It can clearly be seen that the displacement (and thus power output) of the linear spring is the highest, however it has quite a narrow bandwidth. The bandwidths of the nonlinear springs are slightly wider. In the softening case, the nonlinear spring tends to the lower frequency range, which is an advantage since these are more commonly found in real world applications. The bandwidth of the nonlinear springs can potentially be even larger; however, there is always some uncertainty due to the numerical simulation. The type of spring is thus related to the desired bandwidth, in this research a softening spring is used since it tends to lower frequencies. Nguyen et al. [31] also showed that softening type springs perform better under white noise excitation, since vibrations are almost never perfect sinusoidal waves, this can be very advantageous.

2.3.2 Damping

The effect of the damping factor can be seen in figure 2.4. A softening spring is simulated for different damping factors. As can be seen from the figure, the system behaves linearly until the critical damping factor is reached. When the spring reaches the nonlinear state, the power output increases when the damping factor is decreased, forming a vast unstable region. By simulating an up- and down sweep, a clear area can be observed where the system can be in two states; this is called the unstable region. The unstable region can be used to create high power outputs since there is a large displacement with zero to none force (it is unstable).

It can clearly be seen that the damping factor has a large impact on the dynamical behavior of the system. However, it gives a good approximation of the bandwidth of the system (a fair estimation can be made). The tip displacement (and thus also power output) is harder to estimate not knowing the damping factor since there is no way to tell whether the critical damping is reached and the system is thus in it's unstable region. The damping factor should be measured before giving a fair approximation of the performance of the system.

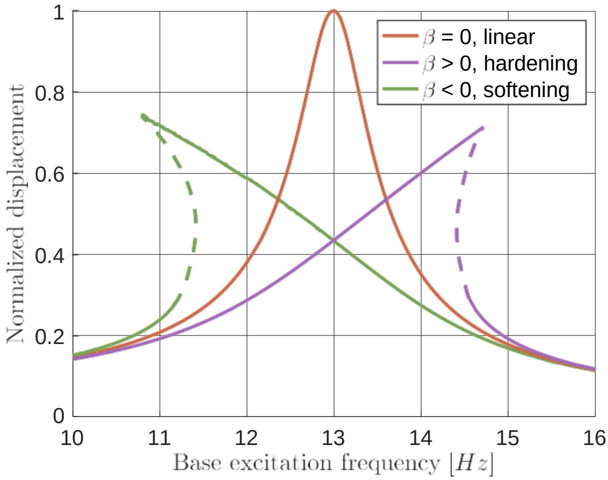

Figure 2.3: Normalized displacement for 3 different types of springs (linear, nonlinear hardening and nonlinear softening) for different base frequencies, damping and linear stiffness term are kept constant

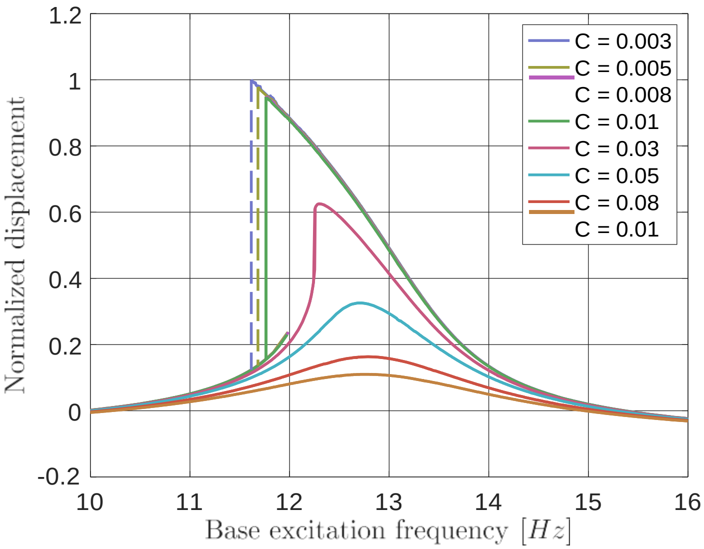

Figure 2.4: The effect of different damping factors on normalized displacement for a range of base frequencies. Increasing the damping factor will decrease the peak normalized displacement and the bandwidth

2.3.3 Electromechanical coupling

As discussed earlier, the electromechanical coupling adds additional damping to the system. The effect of the coupling factor can be seen in figure 2.5. There is an optimal point for the coupling factor. When the coupling factor is too low, only little energy is generated, the system is not used at its full potential. As the coupling factor increases, the power output increases significantly. However, when the optimal is reached, the system tends to get overdamped (since there is additional damping due to the resistor), it loses its nonlinear characteristics. With an increasing coupling factor, comes an increase in resonance frequency (since there is additional stiffness due to the presence of capacitance) and a decrease in power output, this is also noted by [12]. The power output is thus susceptible to changes in the coupling factor. Therefore it is hard to make an appropriate estimate of the performance of the system when not knowing the exact coupling factor.

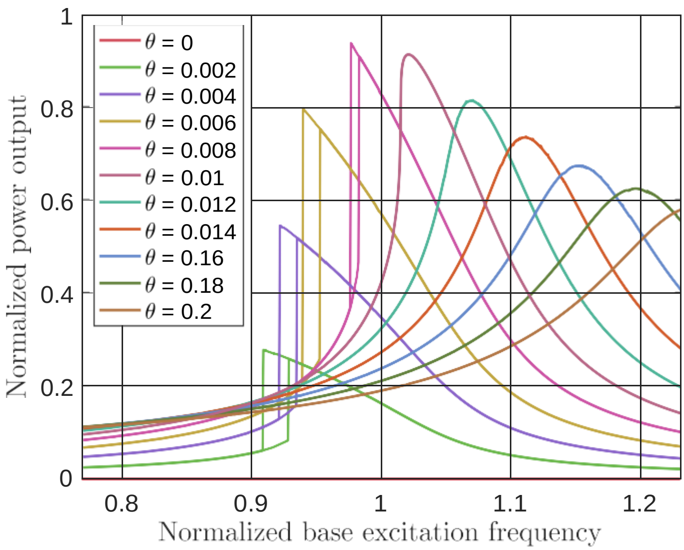

Figure 2.5: Increasing the electromechanical coupling factor will result in a change in power output. When the coupling factor is too high the system will lose it's nonlinear properties and increase in resonance frequencies. When the coupling factor is too low it will not use the system to its full potential.

It was noted by Kamalinejad et al. [25] that the power output is more dependent on the dynamics of the system, then the dependence of the dynamics on the power output. Therefore additional damping could be added to the mechanical system, neglecting the equations of motion for the power output, which would reduce calculation time significantly. However, there is no clear guideline in doing so.

2.4 Discussion

This research has only focussed on theoretical systems and data. Expanding the scope of the research to experimental data would give a better feeling for the values which are commonly used. Using experimental data would give the chance to do an estimation of the performance and see how good the estimation truly is. The values which are used to create the figures are taken from previous research and do not actually have to hold true for real-life systems. Furthermore, the system could be extended to a higher-order polynomial, which is more representative for real-life systems.

2.5 Conclusion

When simulating the dynamics of an energy harvester based on nonlinear springs using only the mechanical properties, some crucial side-effects begin to play a role. The hardening and softening effect will play a role in both energy output and bandwidth. When using a linear spring, there is a narrow bandwidth and a high energy peak. When using a hardening spring, there is a wider bandwidth compared to linear systems (leaning towards higher frequencies). Using a softening spring will also cause a wider bandwidth compared to linear systems; however, leaning towards lower frequencies, previous research showed that these also perform better under white noise excitation. The damping factor is often critical for a good performance estimation; a rough estimation can be made on the bandwidth of the system but not so much at the performance. When the damping factor is unknown, it is hard to guess whether the system even reaches the nonlinear state; the dynamics of the system can, however, be studied. By performing simulations, an optimal damping factor can be calculated. The power output of the system is primarily dependent on the coupling factor. When the coupling factor is too high, the system will be overdamped. When the damping factor is too low, the system will not be used at its full potential. Overall it is hard to make a reasonable estimation of the performance of a dynamical system knowing only the mechanical properties, especially with nonlinear mechanics.

2.6 Further research

The next step is to use experimental data to verify whether it is really true that you can not make a good approximation of the power output of the system using only mechanical properties. The literature review can also be extended by making a dataset from previous research data for dynamical properties, to see how much they differ from each other and whether this will help to make a good estimation of the performance of the system. Furthermore the model easily be expanded with additional side effects (for example hysteresis).

Chapter 3
A new setup for analysis of oscillators under large-amplitude motions

Manufacturing is more than just putting parts together.
It's coming up with ideas, testing principles
and perfecting the engineering, as well as final assembly.

James Dyson

The next step in this research was to investigate large amplitude vibrations. A new piece of testing equipment was necessary to replicate these large-amplitude vibrations. As discussed in this chapter, the air-bearing stage was delivered; however, it was not working. The first goal was to get the stage working; after that, a brief paper was written to verify the stage's working principle. This chapter discusses the dynamics of the stage; when dynamically testing a prototype.

3

A new setup for analysis of oscillators under large-amplitude motions

S.T. Molenaar, T.W.A. Blad and P.G. Steeneken

Abstract
In this research, a new setup is proposed for vibrational analysis based on a linear air-bearing stage. The stage is capable of speeds up to 5 m/s and accelerations up to 10 g. The dynamics are measured using a Polytec Doppler laser vibrometer. The stage is controlled using a PID controller utilizing a linear incremental encoder. A linear oscillator is attached to assess the performance of the stage. The performance of the stage is verified using three methods. First, the theoretical Root Mean Square velocities are compared to the measured velocities. The RMS velocities show a small difference (1%-5%) due to an overshoot in the system. The RMS velocity measured by the Polytec Doppler laser vibrometer is almost identical to the RMS velocity measured using the built-in linear incremental encoder. Next, the signals are processed using a Fast Fourier Transform. The Fast Fourier Transform of the velocity of the linear oscillator shows clear peaks at the eigenfrequencies. A Fast Fourier Transform is also made of the base displacement of the stage when performing a sinusoidal sweep (with constant peak amplitude). This FFT shows a relatively straight line representing the system's constant peak amplitude (as demanded). Lastly, the linear oscillator's mode shapes are measured and compared to the numerical calculated model found using COMSOL. The mode shapes can easily be found and are representative; however, there is a small shift in eigenfrequencies.

Keywords
Energy Harvesting, nonlinear dynamics, forced vibrations, multistability

3.1 Introduction

Over the last couple of years, research interest has been gained in energy harvesting or energy scavenging. One way to harvest energy is by vibrational energy harvesting. A prototype for a vibrational energy harvester is made based on dynamical analysis and calculations. This prototype needs to be tested and verified to check whether it performs as well in practice as it does in the calculations / simulations. Therefore a testing setup is required.

There are two common ways of vibrational testing; real-life testing and a controlled environment (using a shaker, for example). Real-life testing is often used for vibrational energy harvesters since they perform testing for the intended use case [17, 19, 27]. The downside of real-life testing is the lack of repeatability and the disability to tweak the testing conditions. For example, it can be interesting to see a system's performance when altering the base excitation; this is hard to do when performing real-life tests. The second and most common way of testing is by using a shaker. Shakers consist of large coil and magnets, which can vibrate at a frequency range between 0 Hz and 5000 Hz with a maximum stroke of around 45mm. The downside with shakers is their lack of controllability and small displacement [26, 41, 50]. It is almost impossible to get exactly the desired accelerations in a time-domain signal. A controller is necessary to achieve a constant acceleration signal when using a shaker at low frequencies (0 Hz to 30 Hz). Where shakers only have a displacement of several centimeters, the newly proposed test setup can displace up to 50 cm.

In this research, a test setup is proposed based on a linear-air bearing stage from which the dynamics are measured using a Polytec Dopler laser vibrometer (see Fig. 3.1). For verification, a linear oscillator with a low eigenfrequency is attached. The setup is verified using several experiments that verify the performance of the setup:

1. The setup is verified based on the stage's RMS velocity compared to the calculated RMS velocity.
2. A closer look is taken into the Fast Fourier Transform of the stage's velocity and the linear oscillator attached to it.
3. The mode shapes of the oscillator are determined and verified using experiments.

In the next section, the methods will be discussed. First, a brief description of the hardware setup will be given. Next, the different techniques will be discussed, used to verify the stage's dynamical behavior. The experiment results will be shown in the results section, which will be discussed in the following section. The conclusions of the stage will be drawn after that.

Figure 3.1: Experimental setup with the linear oscillator attached to the stage

3.2 Methods

The linear air-bearing stage has a maximum displacement (pk-pk) of 500 mm, a maximum velocity of 5 m/s, and a maximum acceleration of 5 g. The linear air-bearing stage has a feedback system using a linear incremental encoder (with up to 1 nm resolution). The signal is interpolated using a sine interpolator. The ironless motors of the stage are controlled using an AKD servo driver. The servo driver processes the position and acts as a PID controller. Using the AKD controller, it is possible to use the stage in force mode, velocity mode, and displacement mode. In this experiment, the setup is used in

3

displacement mode to prevent run-away. The input displacement is sent to the servo driver as an analog signal.

The stage's dynamical behavior is verified by attaching a linear oscillator (see fig. 3.2). The linear oscillator has a very low eigenfrequency (around 2Hz), which may influence the dynamical behavior significantly if the stage is not valid. The dynamical behavior of the mass-spring system is measured using a Polytec doppler laser vibrometer. The laser vibrometer measures the linear oscillators' velocity at several points (a 9 x 5 grid shown in figure 3.3). The linear oscillator consists of a 0.1mm thick laser-cut plate of spring steel (E=190GPa). This leaf spring attaches to the base by being clamped between 2 aluminum blocks. On the other end is a proof mass (16.8 g) made of aluminum, which is clamped onto the leaf spring. The linear oscillator is depicted in figure 3.2.

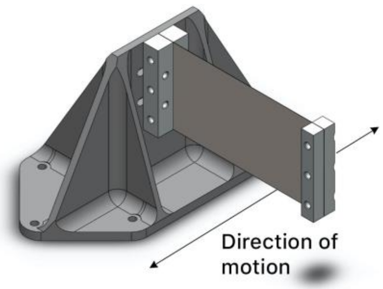

Figure 3.2: Design of linear low frequency oscillator attached to a solid frame with a natural frequency around 2Hz

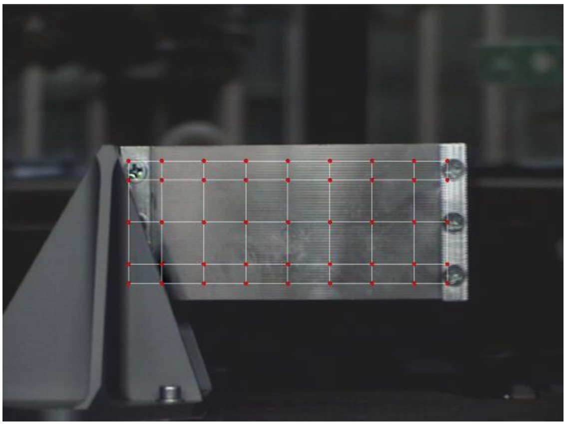

Figure 3.3: Grid of scan points used by the Polytec laser doppler vibrometer

As said earlier, three methods will be used to verify the dynamic behavior of the stage. Each method will be discussed below.

3.2.1 Root Mean Square velocity

The first method for verifying the stage is by looking at the root mean square velocity of the stage when the linear oscillator is attached. Different signals are used, two sine waves with different frequency and amplitude and two square waves with different amplitudes (which have a triangular velocity profile). The testing conditions are tabulated in table 3.1. It is important to note that the stage's input signal is a displacement command instead of a velocity command. The analytical equations are thus given with a displacement amplitude (see Eq. 3.1 & 3.2). The frequencies are at the eigenfrequencies of the linear oscillator, which influence the dynamics of the system. By using the eigenfrequencies of the linear oscillator, the stage is tested at the most challenging conditions.

The RMS velocity is analytically calculated for different signals with the formulas shown below.

$$\mathrm{RMS}_{v,\mathrm{sin}} = \frac{A2\pi f}{\sqrt{2}} \tag{3.1}$$

$$\mathrm{RMS}_{v,\mathrm{square}} = 4Af \tag{3.2}$$

The RMS velocity of the stage is measured using two methods. First, the velocity of the stage is measured using the incremental encoder, which measures the position. This position is numerically differentiated after which the RMS velocity is calculated. The second way of measuring the stage's velocity is by measuring the moving base's velocity with the Polytec doppler laser vibrometer. The experiments are performed at least five times, after which the mean RMS velocity is determined.

3.2.2 Fast Fourier Transform

The second validation method is by looking at the Fast Fourier Transform (FFT) of the velocities. Two methods are used to do this. First, the linear oscillator dynamics are measured using the Polytec (with a 9 x 5 grid) and processed into an FFT. The Fast Fourier Transform should show peaks (high velocities) at the eigenfrequencies of the oscillator. These peaks are also used in the next section to find the mode shapes of the oscillator. The next validation step is by measuring the displacement of the base when performing a sine sweep from 0 Hz to 20 Hz with a constant displacement peak. The built-in incremental encoder measures the displacement signal. This displacement signal of the stage is processed by performing a Fast Fourier Transform. Since the input is a constant peak to peak displacement with different frequencies, the measured FFT should be horizontal, which means that the peak-peak displacement is the same for different frequencies.

3.2.3 Mode shape

The last verification step is by looking at the mode shapes of the linear oscillator. First, the mode shapes of the linear oscillator are calculated using COMSOL. The mode shapes are shown below in figure 3.4. The first mode shape is located at 2.04 Hz, the first bending mode (see Fig. 3.4a). The second mode shape is the linear oscillators' torsion mode (see Fig. 3.4b); located at 11.66 Hz. The third mode is located at 33.5 Hz, the bending mode where the beam itself is buckled (see Fig. 3.4c). The mode shapes are measured using the Polytec Doppler laser vibrometer. The velocity of each scan point is measured for about 8 seconds before moving to the next point. The eigenfrequencies are determined

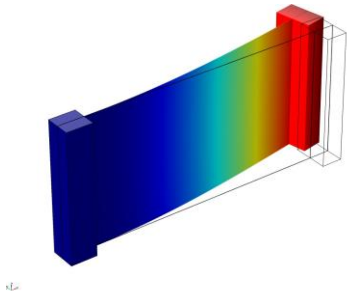

(a) 1^{st} mode shape located at 2.04 Hz

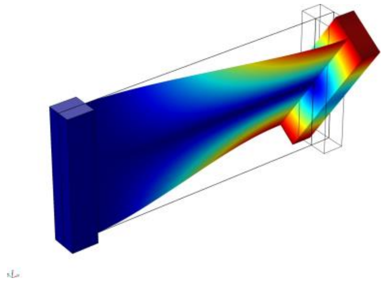

(b) 2^{nd} mode shape located at 11.7 Hz

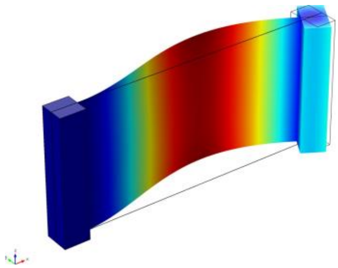

(c) 3^{rd} mode shape located at 33.5 Hz

w

Figure 3.4: Mode shapes as calculated by Comsol

using the FFT of the velocity signal. The Polytec software makes it possible to animate the mode shapes of the system. Looking at the mode shapes does not directly evaluate the performance of the stage itself. However, it gives a fair estimation of the entire experimental setup and how well it can be used for experimental dynamical analysis.

3.3 Results

Several measurements were performed; each result (RMS velocity, FFT, and mode shapes) is described individually.

3.3.1 Root Mean Square velocity

Four different experiments are performed, and the results are shown in table 3.1. The analytical RMS velocity is measured using the formula given in section 3.2.1. The third column shows the measured RMS velocity of the incremental encoder. The last column shows the RMS velocity measured by the Polytec.

Table 3.1: Root mean square error for different velocity profiles

Signal	Analytical RMS	Optical encoder RMS	Measured Polytec RMS
Sine A=0.6mm f=1.8Hz	4.7717 mm/s	4.8350 mm/s	4.9047 mm/s
Sine A=1.5mm f=10.75Hz	71.6415 mm/s	80.1380 mm/s	79.5240 mm/s
Square A=0.3mm f=1.8Hz	2.16 mm/s	2.2624 mm/s	2.2750 mm/s
Square A=0.45mm f=1.8Hz	3.24 mm/s	3.3392 mm/s	3.3913 mm/s

3.3.2 Fast Fourier Transform

The first FFT is the linear oscillator's average velocity spectrum when excited to a chirp signal. The Fast Fourier Transform of the velocity signal for a chirp signal is shown below (see Fig. 3.5).

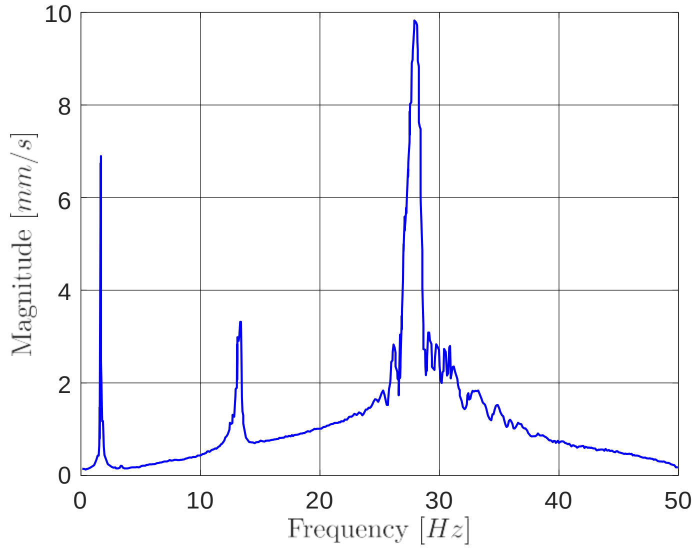

Figure 3.5: Fast Fourier Transform of velocity signal exciting a chirp signal

The second Fast Fourier Transform is calculated from the stage's displacement when performing a frequency sweep. The time displacement signal is shown in figure 3.6a, the corresponding FFT is shown in figure 3.6b.

3

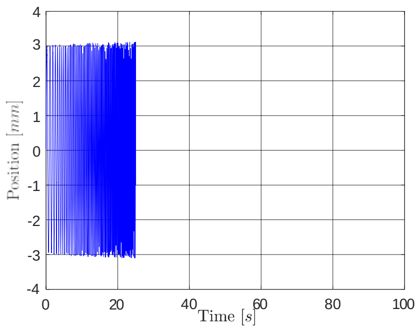

(a) Time displacement signal when a frequency sweep from 1 to 20 Hz is performed with a constant peak-peak displacement of 30 mm.

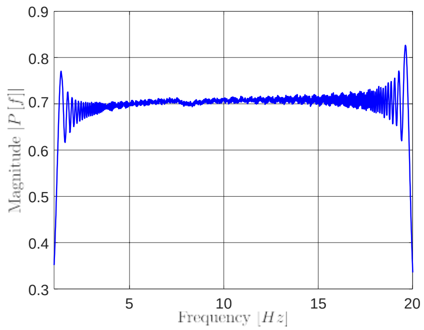

(b) Fast Fourier Transform of the displacement of the air bearing stage exciting a 0 Hz - 20 Hz sine sweep

Figure 3.6: Response of a frequency sweep from 1 to 20 Hz with a constant displacement, when a linear oscillator is attached to the stage.

3.3.3 Mode shape

The last step is to check the linear oscillator's mode shapes. Using the Polytec measurement, the mode shapes of the systems are determined. The mode shapes are animated using the Polytec software. The eigenmodes are located at 1.75 Hz, 12.6 Hz, and 30.6 Hz (see Fig. 3.5). An animation of the signals is shown in figure 3.7, measured when performing a square wave signal.

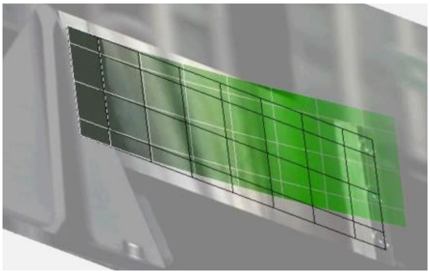

(a) 1^{st} mode shape $f = 1.75Hz$

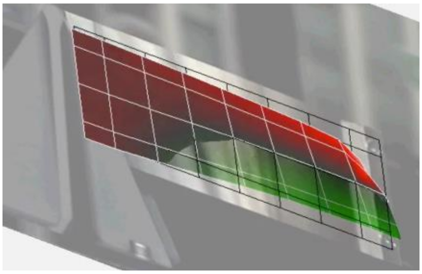

(b) 2^{nd} mode shape $f = 12.6Hz$

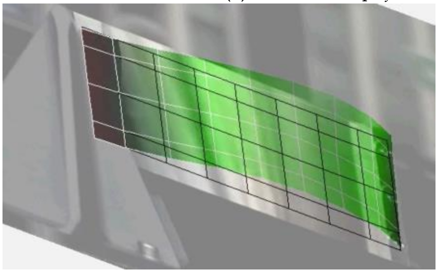

(c) 3^{rd} mode shape $f = 30.6Hz$

Figure 3.7: Mode shapes measured using the laser vibrometer

3.4 Discussion

Each of the results will be discussed individually, after which some general points will be discussed.

3.4.1 Root mean square velocity

There is a small error between the analytical and the measured signal. When looking at the frequency signal, the error tends to increase when the excitation frequency increases. When looking into the time domain signal, this error was caused by an overshoot in the system. When the system has a slight overshoot, it will result in a larger RMS velocity. One should, however, note that the stage is made for lower frequencies. Increasing the frequency requires a stiffer controller. The controller is currently set to be slightly less stiff to ensure noise from the analog input is not amplified. When the controller would be set stiffer, the error decreases; however, audible noise increases, which can be overcome by controlling the stage using a digital input instead of analog.

The RMS velocity measured by the Polytec is almost identical to the measurements by the incremental encoder; there is only a small error between the two. This accordance confirms both the working principle of the incremental encoder and the Polytec.

3.4.2 Fast Fourier Transform

The first Fast Fourier Transform (see Fig. 3.5) represents the oscillator's velocity. The FFT shows three clear peaks, representing the linear oscillator's eigenmodes; these will be discussed in subsection 3.4.3.

The second FFT (see Fig. 3.6b) shows the displacement of the stage when excited at a constant peak-peak displacement for different frequencies. As can be seen from figure 3.6b there is a relatively horizontal line when performing the sweep. There is an overshoot at the beginning and the end of the window. This overshoot can be removed by performing a longer sweep or using a smaller FFT window. It is interesting to see no apparent effect of the linear oscillator's resonance at 2 Hz or 12.6 Hz. The linear oscillator has an amplitude that is around 100 times as large as the base amplitude.

3.4.3 Mode shape

When looking at the mode shapes (see Fig. 3.7), a difference can be seen in the mode shapes' location. The first mode shape was located at 1.75 Hz, where the theoretical mode shape was located at 2.04 Hz, which is approximately a 15 % error. The second mode shape was found at 12.6 Hz, where the theoretical mode shape was located at 11.7 Hz, an error of approximately 8 %. The third mode shape has an error of approximately 10 %. Despite the frequency error, the measurement's form and motion accord with the analytical model (see fig 3.4).

The difference in eigenfrequencies can be due to fabrication errors. The COMSOL model consisted of two solid blocks of aluminum, while the experimental model had screws to clamp the blocks together. These screws add extra weight and a disbalance; one side has slightly more mass than the other. The leaf spring was cut using a mechanical plate shear; this caused some stress in the material, causing it to buckle slightly. These fabrication errors may cause a slight shift in eigenfrequencies; the mode shapes themselves were evident.

3.4.4 General remarks

The stage itself is designed for large-amplitude low-frequency vibrations. The testing performed on the stage had a relatively small amplitude and a relatively high frequency. The stage is capable of movements up to 500 mm with a low frequency, which is not tested in this experiment. However, by testing with such small displacements and high frequencies, the controller was tested in the most challenging conditions.

3.5 Conclusion

The goal of this research was to introduce and verify a new testing setup for vibration testing. The new test setup is tested in 3 ways; first, by looking at the stage's RMS velocity when performing a motion. There is a small difference between the theoretical RMS velocity and the experimental RMS velocity of the stage. This difference can be eliminated by tuning the PID controller to be stiffer.

The second way is by attaching a linear oscillator and finding the Fast Fourier Transform of both the oscillator and the stage itself. From the FFT of the linear oscillator, the eigenfrequencies of the system could easily be found. When looking at the FFT of the base of the stage, there were no apparent effects of the oscillator's resonance on the base velocity.

The last method is a more practical method by looking at the mode shapes of the linear oscillator. By doing this, it can be assessed whether the setup can be used to find the dynamical behavior. There was a small error in the eigenmodes' frequency; this can be due to fabrication errors in the experimental model.

The stage was tested at relatively high frequencies with low amplitudes, while this is not primarily the use-case. The system was therefore stress-tested by testing it at higher frequencies. The stage held up pretty well, and a good dynamical analysis of the system could be made.

Chapter 4
Dynamics of a nonlinear oscillator excited to large amplitude excitations

Engineering is the art of modelling materials we do not wholly understand,
into shapes we cannot precisely analyse
so as to withstand forces we cannot properly assess,
in such a way that the public has no reason to suspect the extent of our ignorance.

Dr. A. R. Dykes

The last and most important paper is a combination of theoretical and experimental work. This paper investigates the dynamics of a nonlinear oscillator when excited to large amplitude vibrations. The dynamics are first investigated numerically, for which a new method to simulate the bouncing behavior is introduced (the bounce loss coefficient). After that, the oscillator is verified on the stage, as discussed in the previous chapter. The nonlinear oscillator is also compared to a linear variant, after which it is shown that the nonlinear oscillator performs better in the large amplitude regime.

Multistable energy harvester performance estimation based on mechanical properties

S.T. Molenaar, T.W.A. Blad and P.G. Steeneken

Abstract
This research investigates the dynamics of a nonlinear oscillator when excited to large amplitude motions. The nonlinear oscillator is a flexure clamped in a frame to create a bistable system. The dynamics are first determined using numerical simulation and are then confirmed by experimental testing. A new method is proposed to simulate the bouncing behavior, called the bounce loss coefficient, which also takes the dynamics beyond the stable point into account. The performance of the system is based on the maximum total energy of the system during the motion. Numerical simulations showed an underestimate of the energy output and a higher acceleration needed to snap in-between states. This may be due to the system's rotation, which was not accounted for in the simulations. The excitation acceleration primarily influences the energy output of the nonlinear oscillator. When the excitation amplitude is smaller than the displacement between the two stable points, the energy output increases significantly. A linear resonator has a smaller bandwidth; however, it has a higher energy output for low amplitude application.

Keywords
Energy Harvesting, nonlinear dynamics, forced vibrations, multistability

4

4.1 Introduction

Research interest is gaining more and more in the energy harvesting field to convert vibrations into electrical energy [28, 42]. Energy harvesters are used for low-power autonomous systems [7, 43], IoT applications [24], and medical applications [3, 5, 33, 37]. They allow for remote monitoring, which improves the safety and reliability of systems and structures [29]. Vibration energy harvesters capture the vibration energy with an oscillator. The conversion to electrical energy is done using piezoelectricity, magnetic induction, or electrostatics.

There are three main goals in designing an energy harvester; making it as small as possible, have large bandwidth [9, 15, 20, 45], and have a large energy output [47, 48]. Earlier work on energy harvesters was primarily in the higher frequency range, from 100 Hz and up [53]. However, current research shows that most of the dominant frequencies found in human motion applications are more often lower frequencies from 0 to 30 Hz [28, 36]. Therefore more and more effort goes into making an energy harvester for lower frequencies. A possible solution for an energy harvester in the ultra-low frequency domain (below 1 Hz) is utilizing a bistable element as an oscillator [21]. Utilizing a novel testing setup, qualitative experimental research could be performed, which was almost impossible before.

Blad et al. [6] introduced the term motion ratio as a metric for quantifying the internal displacement limit relative to the applied displacement. The motion ratio (see Eq. 4.1) describes the relationship between the driving motion amplitude and the dimension in the driving direction. There are two ways to create a low-motion ratio energy harvester by decreasing the driving motion dimension or increasing the driving amplitude. This research focuses on increasing the driving amplitude, which results in low frequencies. Due to the ability to test using large amplitudes (up to 500 mm), the frequency decreases to below 1 Hz (using an acceleration of 1 g).

$$\lambda = \frac{L_z}{2Y_0} \tag{4.1}$$

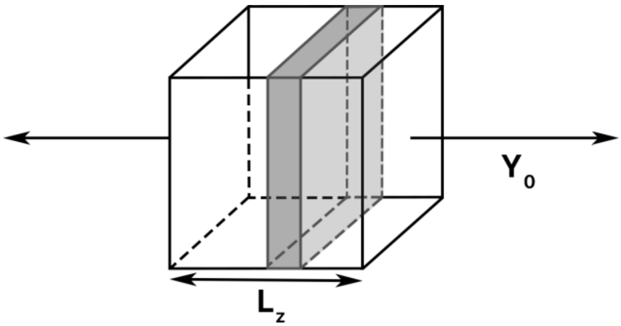

Figure 4.1: Imaginary generator with a certain motion ratio, where L_z is the dimension in the driving direction and Y_0 is the amplitude of the driving motion, the mass (indicated in dark grey) is able to move freely within L_z.

An energy harvester generates electrical energy based on its relative velocity [30]. It is hard or even impossible to attach the energy harvester to the real world in many human motion applications. Take, for example, walking; the energy harvester can be attached to the person walking but not to the ground. Therefore a nonlinear oscillator is needed with a high relative velocity when excited to a large amplitude vibration. To this nonlinear oscillator, a transducer can be attached. The nonlinear oscillator consists of a preloaded flexure and a proof mass, which are attached in a frame. Experimental testing is a costly process; therefore, numerically calculating the dynamics is preferred. However, these large-amplitude motions bring new challenges due to the snapping behavior. A new method is proposed to simulate the damping behavior, the bounce loss coefficient, which describes the velocity after hitting the oscillator's outer limits. The research is done using numerical calculations, after which it is experimentally verified.

The different methods are discussed in section Methods (Sec. 4.2), starting with the bistable mechanism's mechanics (Sec. 4.2.1) and how the performance is evaluated (Sec. 4.2.2); next comes a linear system for comparison (Sec. 4.2.6) . After that comes the dynamics of the bistable unit (Sec. 4.2.3) and the experimental verification (Sec. 4.2.5). In the results section (Sec. 4.3), the different results found from the experimental (Sec. 4.3.2), bistable (Sec. 4.3.3), and the linear model (Sec. 4.3.4) will be shown, which will be discussed afterward in section Discussion (Sec. 4.4). Some recommendations will be given in the recommendations section (Sec. 4.4.5), and lastly, conclusions will be drawn in section conclusions (Sec. 4.5).

4.2 Methods

4.2.1 Bistable mechanics

A flexure is introduced to create a nonlinear oscillator. Due to the nonlinearity in the oscillator, there are two stable points. The interwell motion is used to retrieve high velocities for a broad frequency bandwidth by snapping between the two stable points. The flexure is made from a 0.2mm sheet of spring steel (1.4310 CrNi steel alloy (AISI 301), $E = 185GPa, \rho = 7.9g/cm^3$), cut in the form, as shown in figure 4.2a.

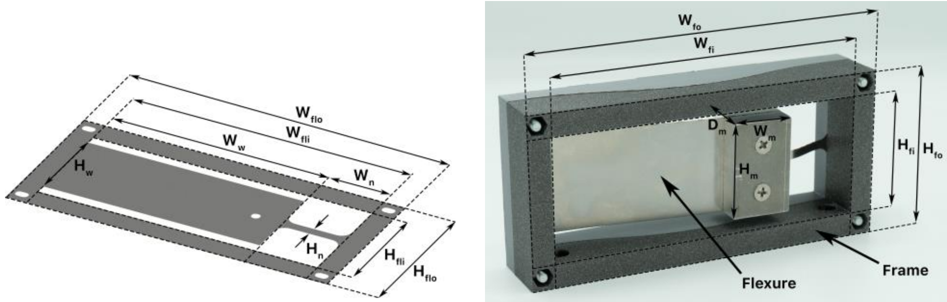

(a) Flexure when it is not preloaded with the relevant parameters.

(b) Assembled mechanism consisting of the flexure clamped into the frame. The flexure is bistable due to preloading and is shown in one of the stable states in this figure. A proofmass is attached to the flexure to the decrease the acceleration necessary for snapping between the two stable states.

Figure 4.2: Nonlinear oscillator used in which the flexure depicted in the left picture is clamped.

By clamping the flexure in a curved frame, the flexure's outer end is forced in the curvature and buckled. The inner part of the flexure is also buckled but still free to move. This way, a nonlinear oscillator is created. A proof mass is attached to the oscillator to decrease the acceleration needed to snap from one stable to the other stable state. A simplified view of the flexure is shown in figure 4.3. By preloading the flexure in the frame, the flexure buckles. The buckled flexure now has two stable states, with an unstable state in between. The bistability of the oscillator is used to snap between the stable states and retrieve high velocities. The relevant parameters for the prototype used are tabulated in table 4.1.

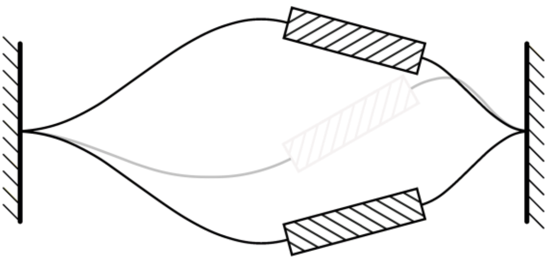

Figure 4.3: Working principle of the bistable flexure. By clamping the flexure in the frame it becomes preloaded (buckled). Due to this buckling there are two stable states, with one unstable state in between.

Table 4.1: Relevant design parameters used throughout this paper. The parameters are primarily shown in figure 2 and 3.

Parameter	Symbol	Value
W_{flo}	Width outside of flexure	152.04 mm
W_{fli}	Width inside of flexure	132.04 mm
H_{flo}	Height outside of flexure	70 mm
H_{fli}	Height inside of flexure	50 mm
W_w	Width wide area of flexure	102.463 mm
H_w	Height wide area of flexure	40 mm
W_n	Width narrow area of flexure	29.577 mm
H_n	Height narrow area of flexure	4 mm
t_s	Thickness of flexure	0.2 mm
W_m	Width of proof mass	25 mm
D_m	Depth of proof mass	20 mm
H_m	Height of proof mass	40 mm
M_m	Weight of proof mass	58.9 g
W_{fo}	Width outer frame	150 mm
W_{fi}	Width inner frame	130 mm
H_{fo}	Height outer frame	70 mm
H_{fi}	Height inner frame	50 mm

The force-deflection curve of the system is found using Ansys. The material is assumed to be perfectly elastic with the following properties ($E = 190GPa, v = 0.34, \rho = 7.82g/cm^3$). The flexure is preloaded, and a displacement is subsequently imposed in the specified points to move between the stable equilibria. During this, the reaction forces are recorded at regular intervals to determine the force-deflection behavior. This force-deflection curve is also used in the numerical model to find the system dynamics (see Sec. 4.2.3).

The force-deflection curve is verified by measuring the prototype's force-deflection curve in a displacement controlled force-deflection setup (see Fig. 4.4). A PI M-505 motion stage with an internal encoder is used to apply the displacement. A FUTEK LRM200 force sensor measures the force required for applying the displacement to the mechanism. The force sensor is attached to the proof mass using a ball magnet to create a rolling contact. The rolling contact ensures that the force sensor remains attached in the unstable region. The data is recorded using a NI USB-6008 in 100 steps with a resolution of 750 μm.

4.2.2 Performance evaluation

The nonlinear oscillator dynamics are evaluated from the nonlinear oscillator as described above (see Sec. 4.2.1). The dynamics are investigated when the system is undergoing a forced vibration perpendicular to the flexure (out of plane). The system is tested for the motion path described in Eq. 4.2 for half a period (thus going back and forth). The motion path describes a motion similar to human motion, for example, walking. A gives the peak displacement of the motion, ranging from 0.001m to 0.35m. The peak ac-

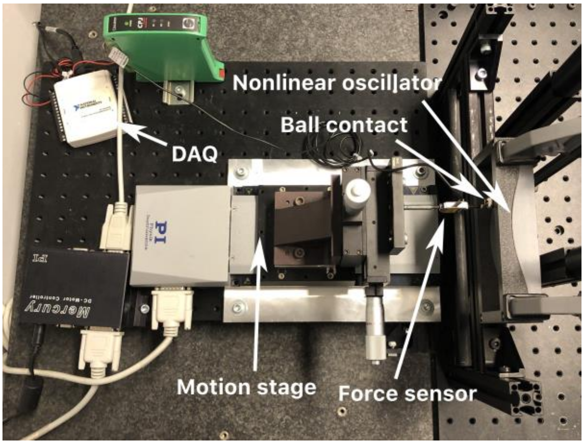

4

Figure 4.4: Experimental setup used for validation of the mechanics. The force sensor is attached to the PI stage and the flexure using a ball contact.

celeration is a_{max}, which is the peak acceleration when performing the motion, ranging from 0.01g to 5g. The range for A and a_{max} are chosen such that experimental testing can be performed (see Sec. 4.2.5). Both the energy and motion of the system will be determined/measured during and after the motion.

$$x = 1 - A * \cos(\omega t) \tag{4.2}$$

For both the linear and the nonlinear system, a numerical model is described and evaluated. Only the bistable system is tested experimentally due to its complex dynamics. The dynamics of the experiment will be compared to the numerical model for validation (see Sec. 4.2.5).

The energy levels (potential and kinetic) of both systems are investigated. The potential energy relates to the oscillator's energy stored. The kinetic energy is the energy that also relates to the system's power output. The two energy levels are added up to find the total energy of the oscillator. This total energy is also the theoretical maximum amount of energy that can be transduced by a transducer.

4.2.3 Bistable dynamics

A numerical model is made to determine the dynamics of the system. The equations of motion are based on the lumped model, where the system is simplified into a mass-spring-damper model. The mass-spring-damper model is extended with the bounce loss coefficient, which will be discussed in section 4.2.4. F_d represents the force exerted due to linear damping ($F_d = c\dot{u}$). The linear damping coefficient is determined from the prototype using the logarithmic decrement method (c = 0.0745 Ns/m). The damping force is calculated using the relative damping between the frame and the proof mass. The spring force is depicted as F_s, a linear interpolation fitted function from the force-deflection curve found in Ansys (see Sec. 4.2.1). The force is not only position-dependent but also history-dependent. The load path is dependent on the initial condition, thus from which stable point the motion starts. When the oscillator snaps from one to another stable state, the other load path is followed. The proof mass's position is depicted as x, the position of the driving motion is depicted as Y, and the relative displacement between the frame and the proof mass is depicted as u ($u = x - Y$).

$$m\ddot{x} = -F_s(x - Y) - c(\dot{x} - \dot{Y}) \tag{4.3}$$

To determine which load path is being used, an output function determines the position after each successful iteration step. The output function compares the stable position (stored in a global variable) with the current position. When the current position is beyond the other stable point, there is a snap through. When such a snap through happens, the global variable is changed, changing the system's load path. The relative tolerance of the ODE solver was decreased to 1e-5 to prevent errors at the snapping point.

The system's kinetic energy is based on the relative velocity between the frame and the proof mass. The force-deflection curve is integrated, starting from the stable points to determine the system's potential energy. It is again essential to know when the system snaps through since the other energy path needs to be used. The same mechanisms, as discussed above, is therefore used.

4.2.4 Bounce loss coefficient

A new method is proposed to simulate the impact behavior, called the bounce loss coefficient (BLC). The bounce loss coefficient is inspired by the coefficient of restitution. The coefficient of restitution is often used for end-stops [2]. It determines the relation between the velocity before impact and after impact.

One might use the coefficient of restitution for a nonlinear system such as described above in section 4.2.1. The stiffness beyond the stable points is higher than the stiffness when moving towards the other stable point. However, the coefficient of restitution neglects all the dynamics happening beyond the stable point. One could argue that the location of the coefficient of restitution should be set further; however, there is no clear guideline in what is the correct distance. Therefore the bounce loss coefficient is proposed. Instead of inverting the velocity right after reaching the stable point (as if it was a ball bouncing off the floor), the velocity is multiplied by the BLC when moving through the stable point towards the other stable point. This way, the dynamics of the system, when beyond the stable point, are not neglected. One might argue that there is additional damping since it has a longer motion path; however, the damping is marginal compared to the effect of the bounce loss coefficient.

The bounce loss coefficient is determined in the same manner as the coefficient of restitution. The prototype is impacted such that it hits beyond the stable point. The velocity peak velocity for the impact is determined, and the peak velocity after impact is determined. In the results section, a comparison between the experimental, coefficient, and bounce loss coefficient will be shown.

4.2.5 Experimental verification

The numerical model of the system is verified using an experimental setup. A linear air-bearing stage is used to accomplish large amplitude motions with high precision. The air-bearing stage has a maximum stroke of 500 mm and has a feedback system using an incremental encoder. The incremental encoder has a pitch width of 20 µm, which is interpolated up to 5 nm precision. Linear ironless motors power the stage, which are controlled by a servo driver. The air-bearing stage allows for creating large amplitude motions. As discussed in Sec. 4.2.1, the prototype is attached to the moving bed of the stage.

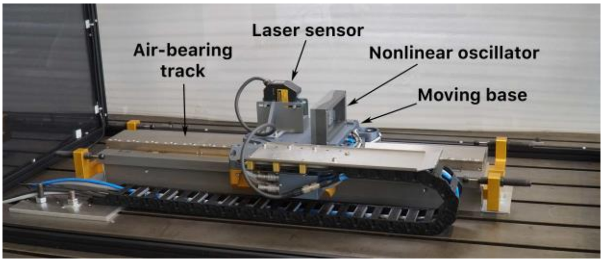

Figure 4.5: Experimental setup used for validation, a linear air-bearing guide with a maximum stroke of 500mm. The frame is attached to the moving base as well as the laser sensor. The frame is attached such that the driving motion is out of the plane of the flexure.

The displacement of the proof mass itself is measured using a Keyence LK-H052 laser sensor. The Keyence laser sensor is attached to the moving bed of the stage and has a measuring range of +/- 10 mm with repeatability of 0.025 um, precisely within the oscillator's range of motion. A figure of the experimental setup is shown below. The data is measured using a NI9215 analog input module attached to a cDAQ-9174 chassis.

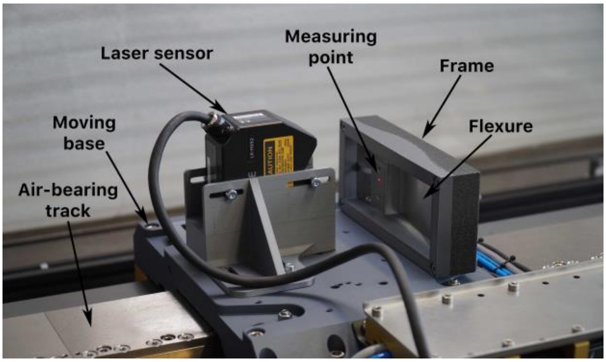

Figure 4.6: Close-up of the moving base. The frame in which the flexure is clamped is bolted to the moving base. The laser sensor is also attached to the moving base and measures the center of the proof mass. The red dot can be seen from the laser sensor from where it measures.

The incremental encoder feedback is also recorded as a reference signal of the motion stage. Since there is the possibility of an overshoot in the system, it is crucial to record and verify the stage's dynamics. Both the laser sensor and incremental encoder measure a displacement. The displacement signal is numerically differentiated to obtain the velocity signal. The stage follows the same motion path as described in section 4.2.2 (see Eq. 4.2).

4.2.6 Linear comparison

A linear system is used as a benchmark to compare the performance of the nonlinear oscillator. The same equations of motion and ODE solver are used as they have been used for the nonlinear oscillator. However, the spring force is now only taken as a linear spring force and not history-dependent.

The most challenging of using a linear spring is the spring constant. When the spring is too soft, it will hit the end-stops, causing fatigue. However, when the spring is too stiff, it will barely move. Therefore the optimal spring stiffness needs to be chosen for comparison where the spring is just high enough not to hit the end-stops. In real-life scenarios, an energy harvester is designed for a specific use case; therefore, it would be a fair comparison to use an optimized spring stiffness for the use case. However, the spring won't work optimal slightly below or above these conditions. In this experiment, the lowest possible spring stiffness is chosen such that it will never exceed the range of motion using the conditions discussed in section 4.2.2.

4

4.3 Results

First, the prototype's force-deflection curve is shown and compared to the force-deflection curve found using Ansys. After that, the numerical model will be compared with the experimental model in the time domain to validate the simulations and the bounce loss coefficient. Next, the performance based on the total energy will be shown. Lastly, the comparison will be made with the linear model.

4.3.1 Mechanical behavior

The figure below shows the prototype's measured force-deflection curve using the red line; the blue line indicates the force-deflection curve found using Ansys. The dashed lines indicate the force required to snap between the two stable states.

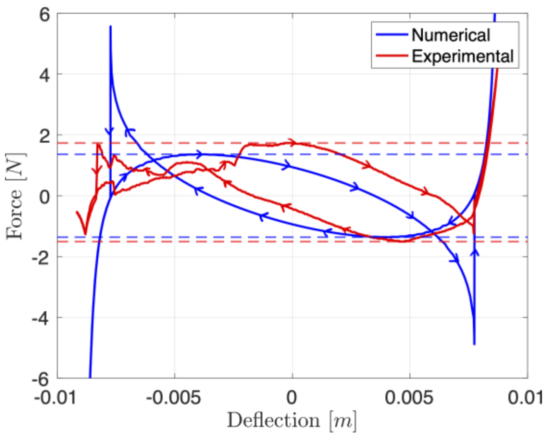

Figure 4.7: Comparison of the numerical and experimental force-deflection curve measured using a displacement controlled force-deflection setup.

4.3.2 Experimental verification

Figure 4.8 shows the numerical and experimental displacement of the proof mass compared to the frame when excited at a displacement of 0.3 m with a peak velocity of 1.95 m/s. Both the methods are shown; the coefficient of restitution is shown using the blue line, the bounce loss coefficient is shown using the red line.

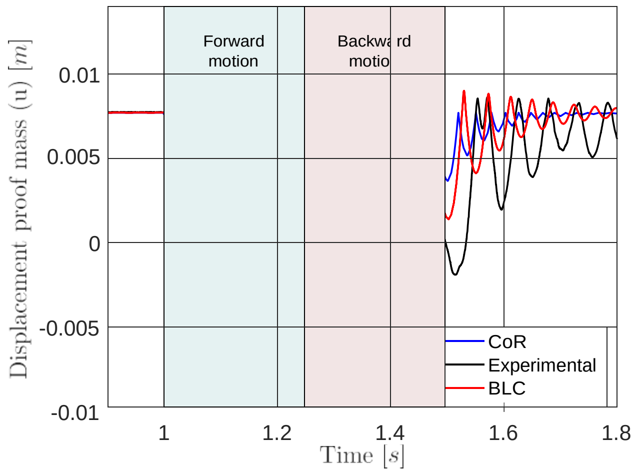

Figure 4.8: Time displacement signal of the experimental and numerical model when performing a motion with a 0.3 m amplitude with a peak velocity of 1.95 m/s. The areas depicted in blue and red are the areas where the base is moving. The blue area depicts the moving forth and the red area moving back. The blue line shows the coefficient of restitution method, the black line shows the experimental data, and the red line shows the bounce loss coefficient.

During experimental testing, torsion modes are noted, the torsion mode interchanges between displacement and torsion. The torsion modes are not measured since the laser sensor measures the center of the proof mass around which it twists (see Fig. 6). A comparison is also made of the numerical energy compared (both coefficient of restitution and bounce loss coefficient) to the experimental energy. The total energy is shown in figure 4.9.

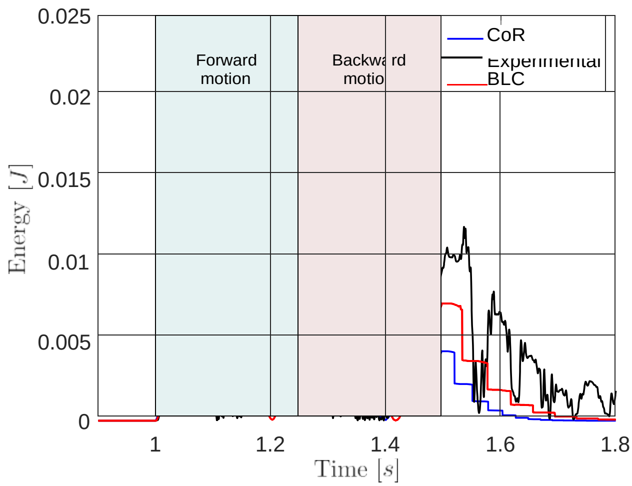

Figure 4.9: Total energy signal of the experimental and numerical model when performing a motion with a 0.3 m amplitude with a peak velocity of 1.95 m/s. The areas depicted in blue and red are the areas where the base is moving. The blue area depicts the moving forth and the red area moving back. The blue line shows the coefficient of restitution method, the black line shows the experimental data, and the red line shows the bounce loss coefficient.

The numerical model is calculated for different forced motions, ranging from 0.1 m to 0.5 m input amplitude and 0.1 g to 5 g acceleration. The results are shown below, with the experimental data plotted as red dots. This figure does not show the influence of the input amplitude since the influence is limited. The influence of the input amplitude can be seen in the next section.

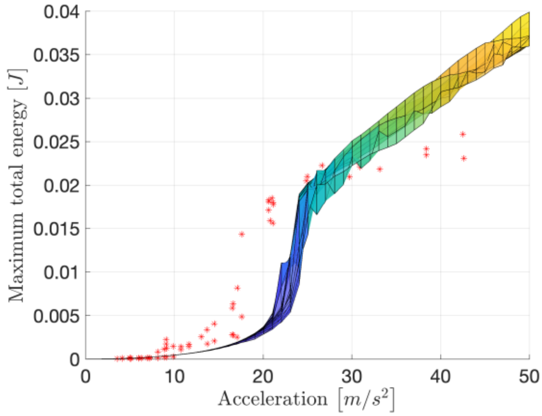

Figure 4.10: Total energy when performing a motion with a peak amplitude of 0.1 m to 0.5 m with an acceleration ranging from 0.1 g to 5 g. The experimental data is depicted with red dots.

4.3.3 Bistable performance

The performance is calculated for a displacement amplitude ranging from 0.001 m to 1 m (logarithmic) with an acceleration ranging from 0.1 g to 5 g. The total energy is shown below. The red dots indicate the experimentally found data.

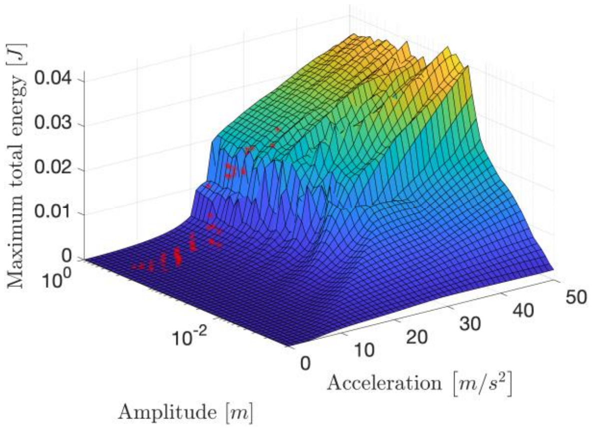

Figure 4.11: Total energy when performing a motion with a peak amplitude of 0.001 m to 1 m with an acceleration ranging from 0.1 g to 5 g. The experimental data is depicted with red dots.

4.3.4 Linear comparison

The bistable system is compared to a linear equivalent. The maximum total energy is shown for the linear system in blue and the nonlinear system in red in the figure below.

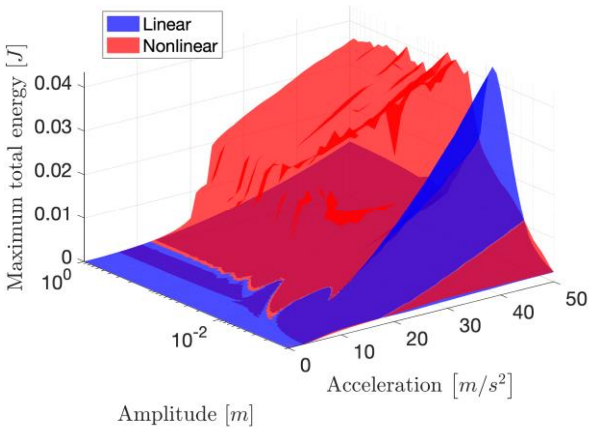

Figure 4.12: Energy levels of the nonlinear and the linear system.

4.4 Discussion

Each of the results, as shown in chapter 4.3, will be discussed below. First, the mechanical behavior of the nonlinear oscillator. After that, the numerical model and the bounce loss coefficient will be discussed. Finally, the nonlinear oscillator's performance is evaluated and compared to the linear equivalent; after that, final recommendations will be drawn from this research.

4.4.1 Mechanical behavior

The first step is to verify the prototype's mechanical behavior since the numerically found force-deflection curve is used for further calculations. From the experimental force-deflection curve, it can be seen that the magnet went loose on the left-hand side (between -0.01 m and -0.002 m), causing the force to drop. However, this does not influence the results significantly since the peak-force was already overcome.

The force necessary to snap between points is indicated with the dashed lines. From the figure, it can be seen that there is a slight difference of approximately 20 % between the forces necessary to snap between stable points. This difference in force might be caused by production imperfections or how the sensor is attached to the prototype. When the force-sensor is not in line with the prototype, it might cause a difference in measured force.

The stiffness in the stable point for the numerical model is 1550 N/m, while the prototype has a higher stiffness of 2783 N/m. This difference might be due to how the force sensor is pushing the oscillator. When the force sensor is slightly off, it might cause a higher force resulting in a higher stiffness.

4.4.2 Experimental verification

The first step is to verify the bounce loss coefficient compared to the coefficient of restitution. The characteristic of the coefficient of restitution is that it will never pass the end-stops which are located at the stable points of the nonlinear oscillator. This behavior is also seen in figure 4.8; the blue line never passes the stable points (located at + 0.0077 m and - 0.0077 m).

It might be interesting to investigate the effect of the position of the end-stop on the dynamics. When the end-stops are set further outwards (beyond the stable points), they will replicate the nonlinear behavior in the oscillator too. However, when the end-stops are set too far outwards, the coefficient of restitution will never be triggered since the proof mass will never reach the end-stop position.

The first apparent difference that can be seen between the coefficient of restitution and the bounce loss coefficient is the effect of damping. The blue line (thus the CoR) seems to be overdamped compared to the experimental model. The red line (the BLC seems to follow the experimental model pretty well, right after the first impact. The most significant difference is when the forced motion stops and the proof mass is free to vibrate. The peak at $t = 1.5$ s of the experimental model is the largest; after that comes the BLC, and lastly comes the CoR. The BLC seems to follow the experimental model better at that point.

Even when the system is not forced, the BLC matches the experimental model better. There is, however, one crucial thing to notice, which is the difference in eigenfre-

4

quency. When the nonlinear oscillator is free to vibrate, the experimental model shows a lower eigenfrequency than the numerical model. This difference in eigenfrequency would imply a difference in stiffness between the numerical and experimental models. This difference in stiffness does not comply with the higher stiffness found using the force-deflection setup. The experimental model has a lower eigenfrequency, which would result in a lower stiffness. However, when looking at the force-deflection curves, the experimental model has a higher stiffness. During testing, rotation of the proof mass was noted; this rotation seems to have a considerable influence on the system.

When looking at the numerical and experimental energy, there is a small overestimate when looking at the total maximum energy for both the coefficient of restitution and the bounce loss coefficient (see Fig. 4.9). Since the velocity is squared to find the kinetic energy (which has the most considerable component), a small difference in velocity will lead to a large energy difference. The BLC has slightly higher overestimates compared to the CoR. However, only by looking at the peak energy of the method does the BLC short. The shape of the CoR is pretty similar to the shape of the BLC. However, the BLC matches the experimental model right after the motions stop (at $t = 1.5$ s) better.

Another interesting thing to note from figure 4.9 is that the experimental energy level fluctuates up and down after the motion. Theoretically, it should only be able to decrease since no energy is supplied to the system. However, it is noted that the proof mass will rotate in the experiments. The flexure seems to hit an eigenmode where the proof mass starts rotating. Energy is transitioned between the mode where it rotates and where it displaces. The rotation is not measured since the laser sensor measures the center of the proof mass around which it rotates, and it will thus not be shown in the energy curve. The transition between the two modes causes the energy level to increase and decrease. The trend is that the total energy is decreasing over time (as expected).

Another interesting thing to see is the coefficient of restitution behavior in the numerical model. Every time an end stops is hit, the energy level decreases with a factor of 0.55 (CoR squared). Due to the coefficient of restitution, the energy of the numerical model has a stepping down behavior. In contrast, the experimental energy tends to decrease more smoothly (not including the energy dips due to rotation).

In figure 4.10, the experimental energy and the numerical energy is shown for multiple amplitudes and accelerations. The experimental model seems to snap from one to another state for a lower acceleration. Thus, the force needed to snap in the numerical model looks higher than the experimental model, which does not comply with the force-deflection measurements (see Fig. 4.7). One possible explanation is the addition of rotation; by rotating the proof mass, the force needed to snap from one to another state. When the system hits the system's resonating eigenmode, less force is needed to snap between the stable states. When the snapping barrier is exceeded, the numerical model has an overestimate compared to the experimental data.

4.4.3 Bistable performance

The performance of the bistable system is shown in figure 4.11. There are two main points, which can be seen from figure 4.11, the influence of the amplitude and the acceleration's influence. When the acceleration is too low, only a small force will be excited onto the oscillator by the proof mass due to acceleration. From the force-deflection curve (as discussed in Sec. 4.2.1), it can be seen that the force needed to snap between states is around 1.3 N. Using a proof mass of 57.8 g results in an acceleration of 24 m/s^2. As shown in figure 4.11, this acceleration corresponds with the increase of total energy after this acceleration.

The second thing to note is the amplitude's influence; when the amplitude is larger than 0.01 m, the influence becomes marginal. However, when the amplitude is smaller than 0.01 m, the energy begins to decrease drastically. This decrease in energy is possibly due to the amplitude being smaller than the distance between the two stable points.

4.4.4 Linear comparison

An important step is to compare the performance of the nonlinear oscillator to the linear resonator. The linear resonator is known to have a narrow bandwidth, while the nonlinear variant has a wide bandwidth. Figure 4.12 gives a good overview of the performance of both. The linear variant shows a clear resonance peak compared to the nonlinear system. The linear case's power output is higher in the resonance peak (at low amplitudes); however, it is much lower at higher amplitudes. When looking for a system with a broad amplitude bandwidth, the nonlinear oscillator is the best solution.

One could argue whether this is a fair comparison; the linear stiffness is chosen such that the displacement is not larger than the displacement of its nonlinear equivalent. The stiffness is relatively high such that the displacement peak in the resonance frequency does not exceed the maximum displacement. However, the energy output for the different input amplitudes may therefore be relatively low. One could argue whether end-stops should not be introduced; this is a fair argument and needs to be investigated whether this is a viable option.

4.4.5 Recommendations

During the experimental testing, rotation of the proof mass was noted. The rotation was due to an eigenmode of the system from which energy was transferred to another eigenmode (displacement). A logical step would be to investigate the influence of this rotation. Furthermore, nonlinear damping effects were ignored due to the inability to estimate the nonlinear damping values. It was early noted by Rayleigh et al. [35] that linear damping is insufficient when investigating impulse behavior. When a reasonable estimation of nonlinear damping can be made of the system, the nonlinear damping can be considered. As a final remark, it would be interesting to investigate the effect of the end-stop location when using the coefficient of restitution. Changing the end-stop location might replicate the oscillator's behavior better; however, there should be sufficient substantiation for where the end-stop is located.

4.5 Conclusions

In this work, the dynamics of a nonlinear oscillator excited to large amplitude vibrations were investigated. The nonlinear oscillator dynamics were simulated using a lumped parameter model with the addition of the bounce loss coefficient. The bounce loss coefficient matched the experimental data more closely compared to the coefficient of restitution. The numerical simulations overestimated the system's energy when it snaps from one state to another. The numerical model showed that the energy output is primarily based on the acceleration when the vibration's amplitude is larger than the distance between the stable points. Experimental research confirms that the energy level is primarily based on acceleration instead of the amplitude of the motion. The model was simplified into a one-degree system; however, during experiments, it was observed that rotations influence the system's dynamics. A linear system may be beneficial when working with small amplitude displacements. The comparison was made to a linear spring, which has a stiffness such that the maximum amplitude would not exceed the motion range of the nonlinear oscillator. The peak energy amplitude caused by the linear system's eigenfrequency was higher than the nonlinear system's peak energy. However, the linear system is more sensitive to changes in the frequency and acceleration than the nonlinear oscillator, making the oscillator better for a broader range of applications.

Chapter 5
Conclusion

Don't mistake activity with achievement.

John Wooden

5.1 Research activities

During the graduation project, multiple research activities were performed. The graduation project lasted 16.5 months from the 2nd of September 2019 until the 25th of January 2021. Due to the COVID pandemic, not all time was spent on the research project, but also 3 weeks were spent on Project Mask. A project to design a testing setup for facial masks during the outbreak of the pandemic. In figure 5.1, an overview of the research activities is given. The research started with analytical research, after which the experimental work began to arouse interest. The air-bearing stage was bought without proper documentation, and the stage didn't work yet. Lots of effort went into getting the air-bearing stage to work, after which it was documented precisely. The knowledge acquired from the analytical research was combined with the experimental setup to verify the analytical research in a paper combining both numerical and experimental work.

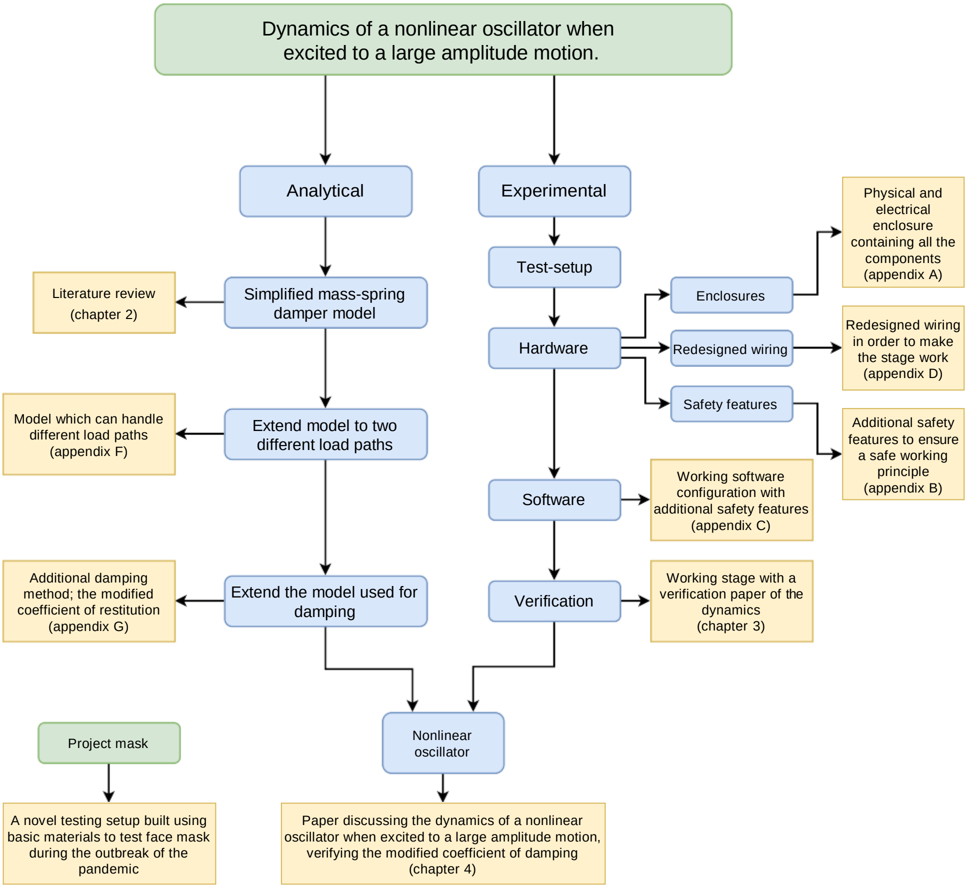

Figure 5.1: Research activities throughout the process, the green boxes indicate the projects, the blue boxes indicate a line of research, and the yellow boxes indicate the output in the research.

5.2 Successes

The project went with many ups and downs; many attempts were made, and it sometimes felt like going one step forward and two steps back. The successes of the process are described below. The unsuccessful attempts are also described in the next section.

5.2.1 Personal growth

During the project, personal growth was achieved in several fields. The biggest personal achievement was working without a clear goal. Working without a clear goal turned out to be rather challenging. Every time something was tried, new problems arose. However, by dividing the problem into smaller problems, it became easier and more fun to do. Having good planning helped during this process.

5.2.2 Project Mask

Right after the outbreak of the corona pandemic, project Mask started. There was a shortage of face-masks, and lots of companies producing shifty face masks arose. Single-purpose masks were even recycled to overcome the shortage. There was a need to test both the shifty masks as well as the recycled masks. The goal of Project Mask was to design a testing setup for face masks with limited resources.

The design phase of the project lasted 2 to 3 weeks, which were quite intense. Weeks of 60 to 80 hours were not uncommon. While it was a war of attrition, it was extremely grateful. Everybody was pushed over their limit; however, it resulted in a project to be proud of.

5.2.3 Air-bearing stage

The most challenging and exhausting part was building the stage. The stage was bought without extended documentation and a servo driver. Some people already built some components to get the stage running, but no one tried to combine them in a working system. The stage was handed to me as a project due to the practicality of it. The first estimation was that it would only take 2 to 3 weeks to get it running. However, it turned out to be three months to get it running and two more months to make it easy and safe to operate. While it took a lot of effort, it was rewarding to see such a valuable piece of equipment running.

5.2.4 Numerical model

Most of the time during this project went into building the stage. When it was done, there was a slight issue. Building such a stage is an accomplishment, but it is not thesis worthy. There was not enough academic value in only building it. The project needed to be extended by combining a theoretical oscillator with an experimental one.

Since there was some arrearage compared to other people, there was a fear of a significant delay. It was a sprint to catch up on the few months lost with the building of the setup. However, the numerical model made during the literature review, with some adjustments, turned out to be sufficient. Since the numerical model complied pretty well with the experimental model, the final steps went fast.

5.3 Unsuccessful attempts

For every successful attempt, there were often multiple unsuccessful attempts. Every unsuccessful attempt felt like a waste of time; however, it brought me closer to the final product, the thesis in front of you.

5.3.1 CompactRIO

The first plan was to control the stage using a CompactRIO. After waiting for two weeks on the cable to connect the CompactRIO to the stage, National Instruments did not update the software anymore. The CompactRIO was, therefore, useless for controlling the stage. At the same time, this was a shame since it would make for an excellent controller. It took two to three weeks to obtain the correct cable, which felt like a waste afterward. However, a more user-friendly and straightforward solution was found using the built-in servo driver software.

5.3.2 Damping

5

In the first model, linear damping was used, which turned out to be insufficient. After that, cubic damping was used, which turned out pretty well. After the simulations were run, the paper was written, and it felt like it was finished. It was noted that cubic damping was excellent. However, it needs to be fitted from the experimental data and thus was not a viable option. A new method had to be conceived, new results were made, and the paper had to be rewritten.

5.4 Conclusions

This thesis's main goal was to research energy harvester dynamics when excited at large amplitude motions. Unfortunately, the research was not extended to energy harvesters but only the nonlinear oscillator to which a transducer can be attached. This research was combined into two parts; the theoretical part and the experimental part.

A numerical model based on known equations of motions was researched to see the effects of different parameters on the system's energy output. The model was extended with nonlinear damping, the coefficient of restitution, and eventually the bounce loss coefficient. The numerical model was applied to a nonlinear spring with known mechanical behavior. A testing setup was built and used to verify the numerical model.

While it is not the most academic work, the most significant addition of this research was the air-bearing stage. The air-bearing stage was only several pieces of equipment that were not working together at the beginning of the project. At the end of the project, it is a novel testing setup that simulates motions that were impossible to simulate before. The stage is easy and safe to operate due to additional features built. The stage was used to verify the behavior found in the numerical simulations.

It was found from the numerical simulations that the numerical model can follow the experimental model pretty well despite fabrication impurities. When there is a slight increase in the modified coefficient of damping, the numerical model will follow the experimental results even better. However, there is still a difference in the acceleration where the oscillator snaps from one to another state. Also, rotation of the proof mass was noted during the experiments.

5.5 Recommendations

There are two main recommendations based on this research. The first recommendation is based on experimental work. National Instruments updated the toolbox for the CompactRIO, supporting the module to connect the servo driver again. Using the CompactRIO with Labview gives endless possibilities in designing an own controller. This controller can be built such that more information can be gathered and the controller can be adjusted to the system. However, making such a controller is almost a master thesis on its own.

The second recommendation is based on the dynamics of the system. Currently, a simplified model is used investigating only 1 degree of freedom. The next step would be to extend the model with a second degree of freedom. During experiments, the rotation of the proof mass was noted. During testing, it seemed like rotating the proof mass would influence the force needed to snap through. It would be interesting to investigate how this rotation influences the dynamics and if this can be modeled.

Acknowledgements

First of all, I would like to thank my daily supervisor Thijs Blad and my senior supervisor Peter Steeneken. For allowing me to create a project that fits my personality. During the project, I've received lots of feedback, helping me progress not only as an engineer but also as a person. The new view on problems helped me progress and stay critical of my research. Special thanks to Thijs for not only being there as a mentor but also as a friend. Being there 24/7, with lots of cheesy jokes and support even (or sometimes only) in the middle of the night.

Next, I would like to thank Armin for his mental support and friendship throughout the project. Since day one, we've been working together and made the promise to finish it together, well we did. Armin is always there to help, often putting others before himself. I would also like to thank Joeri for his companionship during the lab sessions. For always being there, turning on some music, drinking coffee together, eating cake, and getting each other through the setbacks we encountered in building setups. Furthermore, I would like to thank the stroomgraaiers group (Thijs, Armin, Erik, Joeri Kylian) for the numerous memes and for putting all the work in perspective.

During the lab sessions, we could not handle it without the lab support team. First of all, Patrick, for all the great fun we had in the lab, the good taste of music (not if you ask other people), craftsmanship, and always there to help. My graduation project would have been entirely different without him. Bradley, for the help with the electronics, no wonder you deserve the title of spark trigger. Gideon, the lost Brabander, always in for a joke but always there to help. Spiridon, for helping us with the materials we need. And Rob for supplying us with the equipment and keeping a high standard in the lab.

Furthermore, I would like to thank Eveline Matroos, the daily MSc coordinator. Since day one, you were there to guide us and listening to us. There are only a few people who care as much about their students as Eveline does.

The project brought the necessary stress and tension. Therefore I was always very grateful for my work at the fire department. The combination of academic work with no-nonsense work helped me get my mind off things and bring some peace of mind. My friends over at the fire brigade helped me get the mind off my study, laugh together, support each other, and making memories.

Lastly and most importantly, I owe the greatest expression of gratitude to my family. They were always these standing behind me, even in rough times. It is a burden off your shoulders, knowing they are there for you. My work at the fire brigade sometimes also had a significant impact at home; running away from dinner or being grumpy after a night without sleep, it was never a problem. I'm incredibly grateful for the support they've given me throughout.

Appendix A
Air bearing stage - mechanical setup and working principles

This appendix focusses on the specific parts used in the stage, their properties, and their working principles. The stage was designed and made by PM bearings. It consists of three main components, the air-bearing itself where an incremental encoder, and motors are built-in. The servo driver was configured to be used with the air bearing stage as it was not plug-and-play. The controller enclosure was designed to fit all the electrical components and prevent electrocution hazard. Lastly, the physical enclosure is used to provide both protection to mechanical and optical hazards.

Figure A.1: The stage as designed by PM bearings with small modifications. The stage is secured to a heavy metal table.

A.1 Linear motors

The linear motors used in the air-bearing stage are Tecnotion UL-6N ironless motors. The motors are 3 phase (120 degrees) synchronous ironless motors running on 300 V dc (230 V ac RMS). The motors can deliver a peak force up to 480 N, resulting in a maximum acceleration of approximately 10 g. Since the motors are passively cooled, they can't be used for an extended period of time. A temperature cut-off sensor (1000 ohm PTC sensor) is used to prevent the motors from overheating. The servo driver also has a builtin foldback system to prevent the motor from overheating. The motor has a built-in digital hall module for motor control. Both motor controls based on the hall-module and the incremental encoder are used. The working principle of the motors will be discussed in appendix A.1.1. The motor is attached to the moving base of the stage, which is approximately 5 kg. The magnet yokes are two different sized units, the largest one is 546 mm, which is butted together to a 210 mm unit, resulting in a total yoke length of 756 mm. Each magnet pair is 42 mm apart from each other. The moving base itself has a travel of a maximum of 500 mm. More relevant parameters can be found in the table below (see Tab. A.1). All the relevant parameters used in the motor settings can be found in the section software setup (see App. C).

A 33 ohm 500 W regen resistor is added to the system to prevent the motor from overheating and damaging the servo driver. The regen resistor is also called a braking resistor. When the motor needs to slow down very quickly, it needs to dissipate the moving base's energy. Without a regen resistor, it will dissipate the stage's energy in the Kollmorgen internally, causing it to heat up very quickly.

Table A.1: Relevant parameters for the linear motors (Tecnotion UL6n). Data provided by Tecnotion.

Parameter	Remarks	Symbol	Unit	Value
Motortype	3-phase synchronous Ironless			
Max voltage ph-ph	230Vac rms 300Vdc			
Peak Force @ 20°C/s increase	magnet @ 25°C	Fp	N	480
Continuous Force	coils @ 110°C	Fc	N	140
Maximum Speed	@ 300 V	vmax	m/s	5
Motor Force Constant	mount. sfc. @ 20°C	K	N/Arms	68
Motor Constant	coils @ 25°C	S	N^2/W	195
Peak Current	magnet @ 25°C	Ip	Arms	7
Maximum Continuous Current	coils @ 110°C	Ic	Arms	2.1
Back EMF Phase-Phase		Bemf	V/m/s	55.5
Resistance per Phase	coils @ 25C ex. cable	Rph	ohm	8.0
Induction per Phase		Lph	mH	6.5
Electrical Time Constant	coils @ 25C	tau e	ms	0.8
Maximum Continuous Power Loss	all coils	Pc	W	134
Thermal Resistance	coils to mount. sfc.	Rth	°C/W	0.65
Thermal Time Constant	up to 63% . max. coiltemp.	tau th	s	72
Temperature Cut-off / Sensor	PTC 1kohm/ NTC			
Coil Unit Weight	ex. cables	W	kg	0.47
Coil Unit Length	ex. cables	L	mm	190
Motor Attraction Force		Fa	N	0
Magnet Pitch NN		tau	mm	42
Cable Mass		m	kg/m	0.09
Cable Type (Power)	length 1 m	d	mm (AWG)	5.8 (20)
Cable Type (Sensor)	length 1 m	d	mm (AWG)	4.3 (26)

A

A.1.1 Motor principle

As discussed earlier, the ironless motors are 3 phase synchronous motors. The working principle of the motors is discussed below to get a better understanding. The motor has three coils (U, V, and W); these letters are also used in the servo driver. The motors move through a magnetic field. This magnetic field is generated by the stators (the magnetic yokes). Each magnet is positioned 21mm apart; thus, each magnet pairs are 42mm apart. The magnetic field is depicted in the figure below.

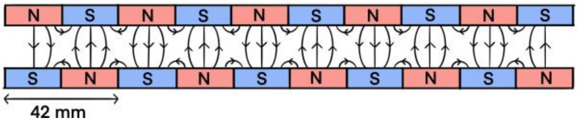

Figure A.2: The magnet field in the stators (magnet yokes). Magnets are spaced 21mm apart; the magnet pairs are spaced 42mm apart.

The working principle of a linear motor can be compared with the working principle of a rotating motor. The only difference is that a rotating motor has (in the most simple case) only two motor poles. By changing the current between the motor poles, the magnetic field changes, the poles are attracted or repelled with respect to the stator magnets. When the poles and stators are in the opposite direction, they will attract each other. A simple figure showing the working principle is shown below. By changing the current and thus the direction of the motor, it will start to turn.

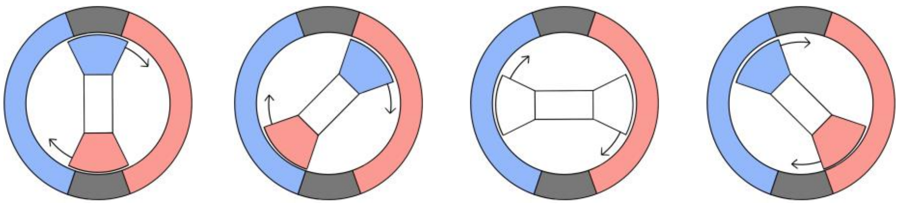

(a) Phase = 0 degrees, the magnets are pulled toward each other; this is the most effortless state since the magnets are exactly in between the states.

(b) Phase = 45 degrees, the magnets are still attracted as in state 1; however, with a lower force.

(c) Phase = 90 degrees, the magnets are in at the point where it needs to tip; when the motor is started in this state, it is not able to determine the direction. The motor keeps on turning due to the moment of inertia. There is a no force since there is no current.

(d) Phase = 135 degrees, this state is the same as state 45 degrees; however, with a different orientation of the magnetic field caused by the motors. The direction of the current has been changed, causing a change in the magnetic field's direction.

Figure A.3: Simplified working principle of a rotating electrical motor.

However, since a linear motor is being used, at least three poles are necessary. When there are only two poles, the system would not be able to start moving. It will keep on attracting itself between two stators. The three poles are positioned further apart from each other than the magnet yokes. By changing the current, the motors are repelled or attracted from the magnets. A servo driver is necessary for controlling the current to the motors. The current is 120 degrees phase-shifted, this causes the magnetic field from the motor poles to change in the correct order to move. The resultant force from 1 motor pole is not constant (it is continuously changing over time); however, the resultant force of the thee motors combined is constant. A clarification of the phase shift between the motor poles is being shown in the figure below.

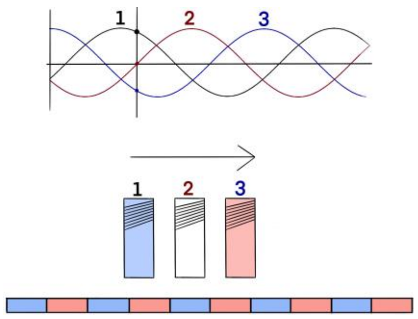

(a) State 1; motor 1 has a positive current resulting in a north-oriented magnetic field, which results in an attracting/ repelling field to the right. The second motor has 0 zero current resulting in no magnetic field. Since the motor is right above a magnet, no horizontal force can be generated. The third motor has a negative current resulting in a south-oriented magnet field; the magnet field is attracting/ repelling the stator magnets.

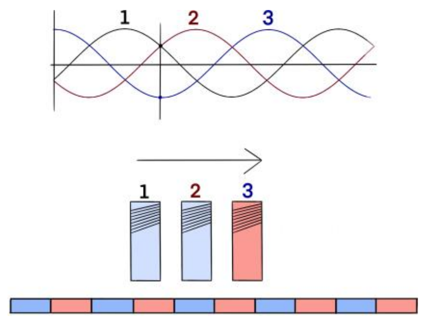

(b) State 2; all motors have a current and, thus, a magnetic field. Motor 1 and 2 both have a positive current resulting in a north-oriented magnet field. Both magnets are attracted/ repelled to the right. Motor 3 has a large negative current resulting in a sizeable south-oriented magnet field. The third motor is thus repelled/ attracted the strongest.

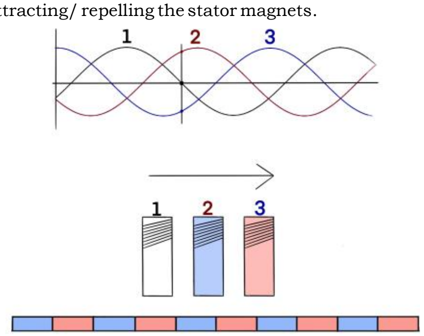

(c) State 3; this state is quite similar to state 1. However, in this state, motor 2 is north-oriented, and motor 3 is south-oriented. Motor 1 is right above a magnet, resulting in a force perpendicular to the motor.

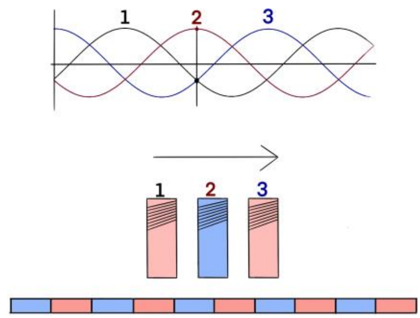

(d) state 4; in this state, all the magnets have a current and resulting magnetic field (just as state 2). The current of motor 2 is at its highest since it is right between 2 magnets, resulting in the highest force in motion direction.

Figure A.4: Simplified working principle of a rotating electrical motor for different example states.

As said earlier, a hall sensor is built in the motors. The hall sensor measures the magnitude of the magnetic field caused by the stators at each motor. The location of the motor poles with respect to the stators can be determined using the hall sensors. This process only gives a relative position of the motor and is not used for position control. The hall sensor is used to control the motors by knowing the relative location of the stators.

A.2 Incremental encoder

The actual position of the stage is determined using an incremental encoder. The incremental encoder has a 20 nm interpolator for increased resolution. The incremental encoder consists of three main parts; the scale, the readhead, and the interpolator. An incremental encoder gives a relative displacement from a reference point. Therefore, reference marks are installed on the stage. The scale is a gold scale provided by Renishaw (RGSZ20 scale). The scale has an ultra-low cyclic error (+- 30 nm) and resolutions up to 1 nm. The scale has a pitch of 20 µm and a linearity of 3 µm/m. There is one reference mark, and two limit marks attached to the scale (see Fig. A.5). The reference mark is used to calibrate the encoder. The limit switches are used to determine the stage's outer limits used for the homing procedure. The readhead used is a Renishaw TONiC T1000-05A, capable of speeds up to 10 m/s. The readhead can handle shocks up to 50 g, which makes it perfect for dynamic testing. A Renishaw Ti1000-0A interpolates the signal from the readhead. The output of the interpolator is an analog signal (sine and cosine). Since the Renishaw interpolator is not directly compatible with the stage, an additional termination resistance adapter is designed; this will be discussed in appendix D.

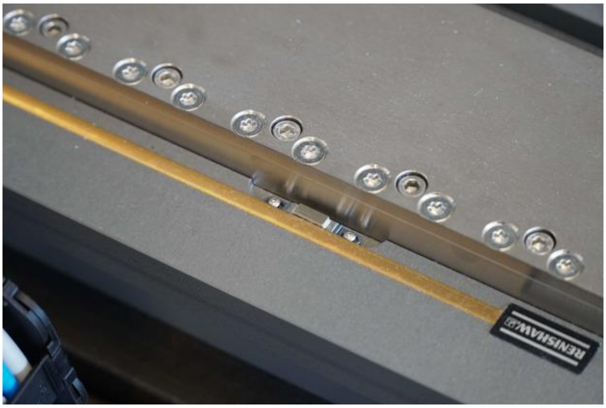

Figure A.5: One of the limit switches on the track.

A.2.1 Working principle

There are two main working principles; first is the readhead itself, then comes the interpolation. The readhead sends out a light source, from which the reflection is measured. The scale has reflecting parts and nonreflecting parts spaced 20 µm apart from each other. When the readhead moves over the scale, it will give pulses (one pulse every 20um). When measuring the pulses for a certain amount of time, the speed can be calculated. When the readhead moves over the scale and measures 30 pulses in 1 second, it moves 20 µm * 30 = 600 µm in 1 second, resulting in a speed of 600 µm/s. However, this only gives you the speed and not the direction of motion; therefore, a second scale is added. The second scale is shifted 90 degrees from the original scale. By comparing the two signals, the direction of the motion can be determined as well. An illustration of the signal is shown below.

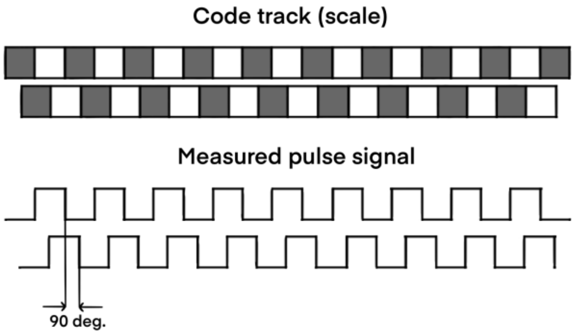

Figure A.6: The scale and working principle of the incremental encoder. The code track is measured using the readhead as pulses. There is a phase shift of 90 degrees between the two tracks. The pitch of the scale is 20um.

The resolution of the signal is improved by using a sine interpolator. The sine interpolator interpolates the digital pulses into an analog sine wave. The sine waves are again 90 degrees shifted. The peak to peak value represents the 20 µm scale. However, since it is a sine wave, it contains way more information than only the pulses. By interpolating the signal, the accuracy increases significantly. The reference signal, however, is still a digital (pulse) signal. The output of the interpolator is sent to the Kollmorgen servo driver.

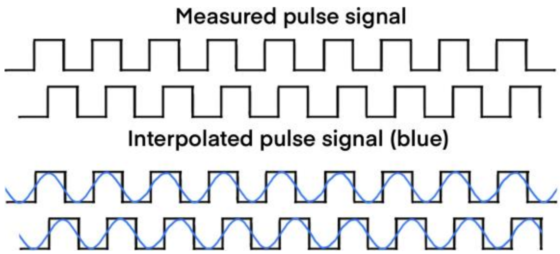

Figure A.7: The scale and working principle of the interpolator. The pulse signal is fitted with a sine wave to get a higher accuracy.

A.3 Air-bearing

PM-bearings designed the air-bearing and fabricated the stage (motors, incremental encoders, and air-bearing). The air-bearing is custom made for the stage; specific features are thus not available. The stage should be applied with at least 4 bar (400 kPa). Working at slightly higher pressures is less harmful than working at lower pressures. Since the air-bearing is sensitive to impurities in the air, it first goes through several filters. SMC Corporations supplied the air filters (see Fig. A.8). The air is provided by a centralized compressor, which has a working pressure of 8 bar.

Figure A.8: Air filters used for the stage, the air is flowing from left (compressor) to the right (stage)

The airline's first component is the filter regulator (SMC AW30-F03CE-B); this regulates the air pressure to the working pressure (4 bar). The maximum inlet pressure is 10 bar (1 Mpa). The filter has a nominal filtration ratio of 5 µm. Next in line is a micro-mist separator (SMC AFD30-F03-A). The separator has a nominal filtration rating of 0.01 µm (99.9 % filtered particle size). The outlet side oil mist concentration is max. 0.1 mg/m^3 (ANR). The air is again sent through an air filter through a micro-mist separator with a slightly higher nominal filtration rating of 0.3 µm (99.9 % filtered particle size). The outlet side oil mist concentration is max. 1.0 mg/m^3 (ANR). Lastly, the air goes through a membrane air dryer (SMC IDG10-F03), after which it goes to the air-bearing and a pressure relay for safety. The air dryer has a dew point indicator purge airflow rate of 1 L/min (ANR) and an outlet air atmospheric pressure dew point of -20 °C.

A.3.1 Mounting plate

The moving base has a large mounting plate on which the prototypes can be attached. It is crucial to notice that only these mounting holes can be used. There are multiple nuts on the stage used to adjust the air bearing; **these should not be adjusted without PM-bearings instructions**. A figure of the mounting plate is depicted below, where the mounting holes are type M4x0.7. The mounting holes are tapped in aluminum and are therefore not very strong. Helicoils can be applied; however, the holes should first be drilled out. Since this is not desirable, the screws should not be overtightened in the stage.

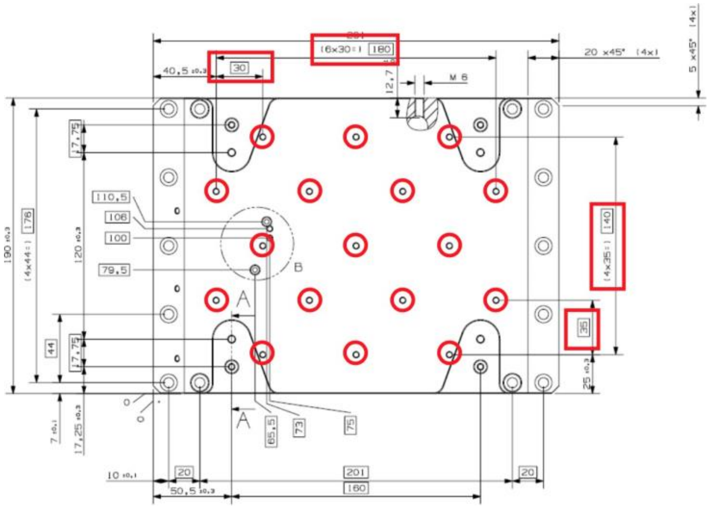

Figure A.9: M4 mounting holes on the stage, the holes encircled with red can be used. The mounting holes are 8mm deep.

A.4 Servo driver

The beating heart of the stage is the servo driver. It controls the motion and brings all the signals together. The servo driver has several inputs; the incremental encoder, the hall sensor, digital inputs, and an analog input. The output are several digital outputs, an analog output, and the power output to the stage's motors. For a servo driver, the AKD basic (AKD-p00306) is being used. The specifications are listed below.

Rated Data	Units	Value
Drive Continuous Output Power	Watts	1100
Rated supply voltage	V	240
Control logic, supply voltage	V	24
Rated output current (RMS value ±3%)	A	3
Peak output current (±3%)	A	9
Peak time	s	5
Current loop Bandwidth max.	kHz	2.5 to 4
Velocity loop Bandwidth max.	Hz	0 to 1000
Position loop Bandwidth max.	Hz	1 to 250
Update rate	MHz	1.5

The servo driver is mounted inside the controller enclosure. It is depicted in the figure below, as can be seen, there are several inputs and outputs. Each connector will be discussed briefly below and more elaborate in appendix D. Connector X1 is used for the logical power and the STO. The motors are connected through connector X2. Power is supplied to the driver by connector X3. Connector X7 and X8 are used for inputs and outputs. X10 is connected to the incremental encoder. Lastly, port X11 (ethernet) is con-

A

trolled for service. The servo driver uses a Field Programmable Gate Array (FPGA) to control the stage. There are four command sources and three operation modes. These modes will be discussed briefly below; the usage and settings will be discussed in appendix C and E. The first command source is the service mode; this controls the stage through the ethernet cable using Kollmorgen workbench. The second command source is the Fieldbus; this is not being used for this setup. The third mode is electronic gearing, where the position is proportional to the secondary feedback. This mode is also not used for the stage. The last and most used mode is the analog input mode. It measures the analog input voltage and converts this into a force-, velocity, or position command. The operation mode determines which control loop is being used for the command source. There are three operation modes: torque mode, velocity mode, and position mode. Each mode will be discussed below.

A.4.1 Current control loop

The lowest level of control is using the current loop. The driver controls the current passing through the motor. The current is proportional to the force the motor generates. A figure of the current loop is depicted below. The command source determines the amplitude of the current command. A current offset can be added to the system, which is added to the overall current loop feedforward value. The Coulomb friction component can also add friction. This friction requires a friction current and viscous feedforward gain; this is not used explicitly. Cogging compensation is used when the systems tend to have a stick-slip condition, however, is not used since the stage has an air bearing. The limiter determines the maximum current allowed to the motors. The maximum can be the peak value or a value below to prevent damage to the motors (foldback). The current feedback is subtracted to find the current difference that needs to be supplied to the motors. This difference is fed to the PI controller, which determines the voltage command. The PI controller has a proportional gain and parameters based on the motor properties.

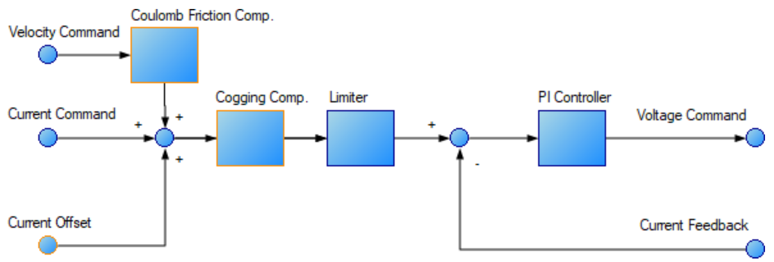

Figure A.10: Current control loop of the Kollmorgen servo driver, as depicted in Kollmorgen Workbench

A.4.2 Velocity control loop

When going one step further, the velocity loop is introduced. In the velocity mode, the controls are based on the stages velocity. A large control loop is involved, which is depicted below in figure A.11. On the upper side of the loop, the velocity profile and the fol-

A

lowing commands are shown. The velocity profile is determined for a motion task; these motion tasks are uploaded to the driver when in service mode. These values are directly added to the current command. However, since service motion is not the primary use case, it will not be discussed below. The values can all be found in the motion tasks and the selected profile. Let's discuss the primary velocity loop. First, the velocity signal is checked for the acceleration, whether it is not too large. When the acceleration is too large, it will be limited by creating a velocity ramp. The velocity clamp affects the maximum speed of the drive when the command source is in service mode. The feedback velocity is subtracted from the velocity command. AR3 (unity gain) and AR4 (Autotuned BiQuad) filter the feedback signal, which is observed by feedback 1, the incremental encoder. The observer mode should be set to 0; when the observer mode is set to 1, it will use a model to determine the velocity. There is no model for the stage; this mode should not be used; it needs to use the incremental encoder's actual feedback. Filter AR1 and AR2 filter the velocity error (velocity command minus feedback). Filter AR1 is a lowpass filter set at 675 Hz, AR2 is an autotuned BiQuad filter which is adjusted. Adjusting AR1 will adjust the audible noise by the stage. The filtered signal is sent to the proportional-integral controller, which gives the current command. The current command is sent to the current loop (see App. A.4.1), determining the motors' voltage.

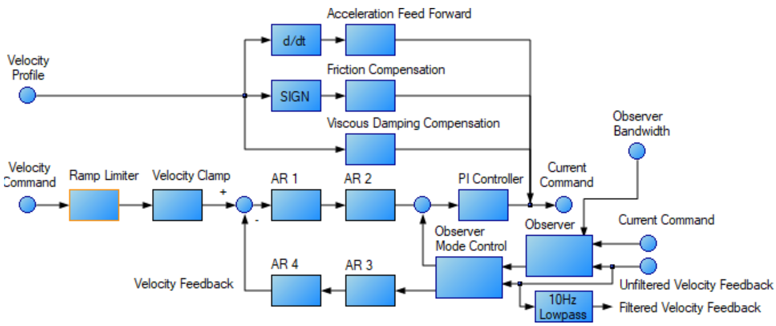

Figure A.11: Velocity control loop of the Kollmorgen servo driver, as depicted in Kollmorgen Workbench

A

A.4.3 Position control loop

The final control loop is the position control loop. In the position control mode, the drive's controls are based on the position of the motor. The loop is depicted below in figure A.12. The upper loop is used as a velocity feedforward loop. The desired velocity (based on the position) is determined by differentiating the position. This feedforward position is multiplied by a feedforward gain (this is often set to 1). The position error is determined by subtracting the position feedback from the command. The position error is first checked, whether it is not too large. When the position error is too large, it will result in a fault. The position error is set to a relatively small value to give a fault when run-away occurs. A PI controller processes this error signal. The damping is added by the feedforward gain, resulting in a PID controller. The velocity command is sent to the velocity control loop, which sends a current command to the current control loop. The stage is most often used in position mode due to the small chance of run-away. When the stage is used in velocity or force mode, it can run-away, resulting in hitting the end-stops.

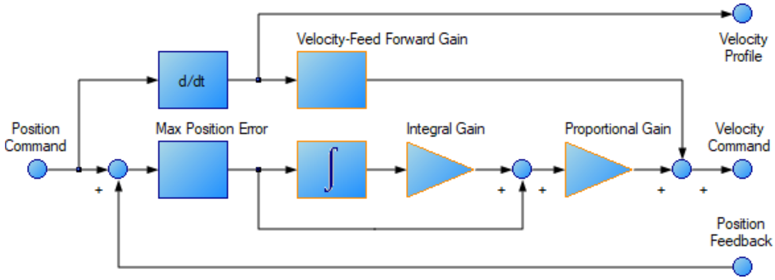

Figure A.12: Position control loop of the Kollmorgen servo driver, as depicted in Kollmorgen Workbench

A.5 Controller enclosure

All the electronics are built in a controller enclosure to prevent the danger of electrocution. The stage only works at 230 V AC; however, it is not desirable that the cables are open and free to touch. The controller enclosure is a Rittal AE1339.500. By using a controller enclosure, several interface features are added. The enclosure holds the main power switch, six indicator lights, and two buttons. A figure of the outside of the controller enclosure is shown below. The switch on the bottom acts as the main power switch; when the power is turned on, the white indicator light on the top left will light up. The green indicator lights indicate that the stage is turned on (loaded). The blue button will light up when the button can be pushed. By pushing the button, a fault in the servo driver will be reset. Next to the blue button is the red indicator for the safety circuit; when the safety circuit is interrupted, the light will turn on. The red indicator next to it is the fault indicator light; this led will light up when a servo driver fault is issued. Next to the main power switch is the power switch for the motor bus power; by turning on the switch, power is supplied to the servo driver. It is crucial to note that turning off the motor power button will not automatically mean there is no power going to the motors.

It will only cut the power supply to the Kollmorgen; the internal BUS bar can still hold voltage. The controller enclosure should remain closed when the main switch is turned on, and the stage is in use.

Figure A.13: Outside of the controller enclosure with the interfacing features.

The controller houses several components; Kollmorgen servo driver, regen resistor, National Instruments Compact Rio, 24v Power supply, relays, and an air-pressure relay.

A.6 Physical enclosure

The stage can generate a lot of force and is dangerous due to the moving parts. One can easily crush his hand by getting hit by the moving base; therefore, a physical enclosure is built. The physical enclosure is built up of Thorlabs aluminum profiles (see figure below). The enclosure has one large side door which can be opened to work on the stage (to attach prototypes, for example). When the door is opened, the safety circuit is interrupted, which will stop the stage's motion. The side panels are made out of 5mm thick polycarbonate, which is known for its high toughness. The physical enclosure is bolted onto the table to prevent any movement. One side of the enclosure has an extra black panel for when the Polytec laser is being used.

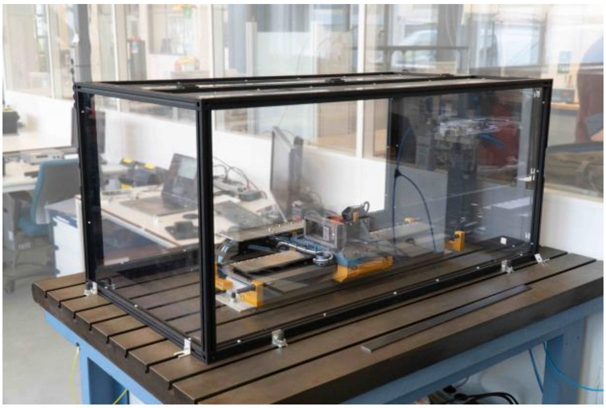

Figure A.14: Physical enclosure built around the stage to prevent any mechanical and optical hazard.

Appendix B
Air bearing stage - Safety features

Since the linear air-bearing stage is a very delicate, expensive, and possibly dangerous piece of equipment, several safety features are built-in. These safety features range from hardware to software solutions. First, the primary hardware features will be discussed (Sare Torque Off (STO), end-stops, and enclosures). Next, several software features will be discussed.

B.1 Safety Torque Off (STO)

The Safety Torque Off is a feature built-in the servo driver. The STO is a pin on the servo driver; when 24V is supplied to the pin, the stage can turn on. When there is 0V supplied to the pin, the stage will stop immediately (the pin has a reaction time of <10ms). Several safety features are connected in series; when one safety condition is not met, the wire will be interrupted. The first safety feature is the emergency button; the button has a normally closed contact (see Fig. B.1). The contact will normally be closed until the button is pushed, interrupting the 24v loop. The next safety feature is the switch in the physical enclosure; when the enclosure is opened, the loop is interrupted. The last feature in the safety circuit is the air-pressure relay, which measures the air pressure supplied to the stage. When there is no or insufficient air pressure supplied to the stage, it will not turn on. It is currently set to just slightly below 4 bar. When the Safety Torque Off loop is interrupted, a red indicator will light up on the controller enclosure.

Figure B.1: The emergency button connected to the STO circuit.

B.2 End-stops

The stage has dampers built on the outer limits of the track (see Fig. B.2). When it was to hit the end-stops, the shock will be absorbed. Two limit-switches are built-in at the end of both sides of the track. These limit switches are about 1 cm before the physical end-stops. When the base moves over the limit switches, they will be detected by the incremental encoder. The signal is connected to a high-speed digital input (update rate: 250us). Triggering the limit switches will cause an error in the servo driver software. No-fault is issued; thus, the axis will remain enabled. The limit switches are also used to determine the center of the stage. At start-up, the stage will start moving to the right until it finds the first limit switch, after which it will move to the center of the stage.

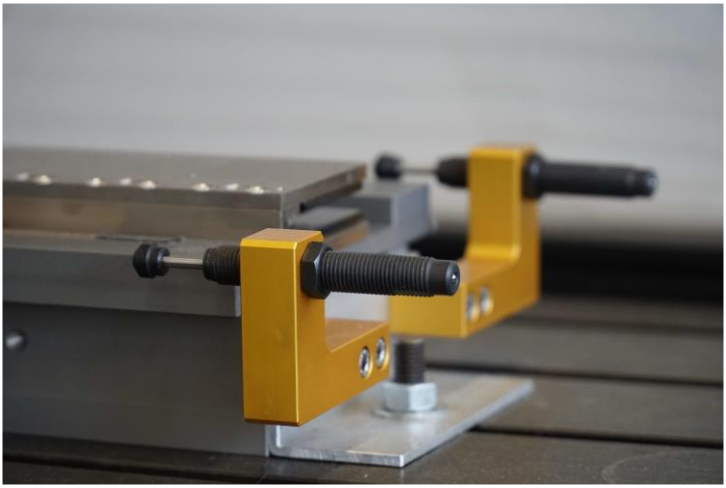

Figure B.2: End-stops attached to the end of the air-bearing track to absorb the moving base if it were to hit the ends..

B.3 Enclosures

There are two primary enclosures, the controller enclosure and the physical enclosure. The controller enclosure protects against electrocution danger. The physical enclosure protects against mechanical danger as well as optical dangers (laser). A more detailed description can be found in appendix A.6.

B.4 Switch off behavior

The axis can be disabled during operation due to several reasons. Disabling can be done, for example, on purpose when an experiment is finished but also for safety reasons. In both cases, it is essential to reduce the speed of the stage as fast as possible. When the stage is disabled, it will first decrease the speed to a threshold speed of 3.5 mm/s. Reducing the stage's speed will significantly reduce the danger of hitting the end-stops or, even worse, the person operating it. The velocity profile is depicted below.

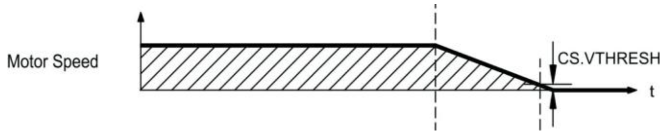

Figure B.3: Velocity profile when the motor is turned off.

B.5 Temperature cutoff

The linear motors have a built-in positive temperature coefficient (PTC) resistor. When the temperature of the motors exceeds a specific value, the resistance will increase drastically. When the PTC in the motor reaches 1000 ohm, the motor is overheated and needs to be turned off. This process is done automatically by the servo driver. Due to the presence of the regen resistor, the motors will tend to overheat less quickly. This safety feature is mainly to protect the stage itself from damaging.

B.6 Foldback

The motors are protected from too much current by several systems. The peak current is set to 7 A according to the motor specifications. The maximum allowable current is determined using a foldback mechanism. The peak current can only be applied for several seconds. A figure showing the working principle of the foldback is shown below. The maximum current can only be applied for a short amount of time, decreasing the current to its constant current value. It is essential to keep an eye on the foldback current since it decreases over time. When the current decreases, the force will also decrease. Therefore, it may seem like the PID controller can't hold up while the motors cannot deliver more power.

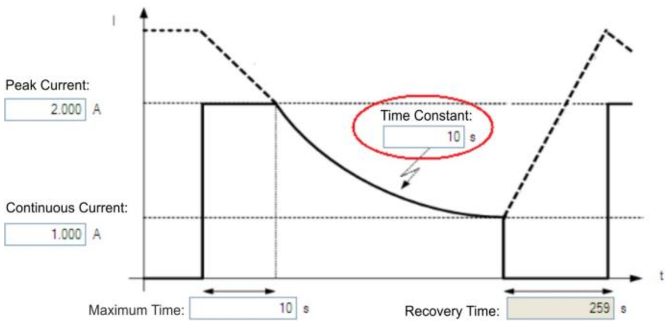

Figure B.4: Working principle of feedback. The motors can only a certain time on the peak current.

Appendix C
Air bearing stage - Software setup

This appendix describes the settings used in the Kollmorgen Workbench software and how they are determined. It will be a step by step guide on how to fill in the correct parameters. The settings are valid for the setup, as described in appendix A, using an AKD-P0306-NBCC servo driver. First, the device settings will be discussed; after that, the axis (motor) settings will be addressed. A practical guide on how to use the setup is given in appendix E.

C.1 Device settings

First, the device settings will be discussed; the device settings control the servo driver's inputs and outputs. Each settings tab will be addressed individually.

C.1.1 Communication

The first tab describes the type of protocol used in the device. This section is also used to communicate between the computer and the driver. In our case, the device type is set to "1 - Analog with position indexer".

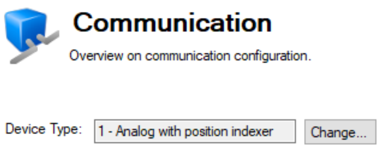

Figure C.1: Kollmorgen workbench communication settings.

C.1.2 Power

The power tab is used to monitor the bus voltage; this is not the output voltage on the motors. The bus voltage describes the voltage applied to the servo driver; the power is supplied through a relay module as described in appendix D. The under-voltage fault threshold determines when a fault is issued when there is too little voltage on the bus. A warning is given when the bus voltage is between the fault and warning threshold. The same holds for the overvoltage warning. An overvoltage can occur when there is a large back-emf, current fed back to the driver due to the motor braking. The under-voltage fault mode should be set to "1 - Only when drive enabled", and the operating voltage should be set to "0 - Full". A figure with the correct parameters is shown below.

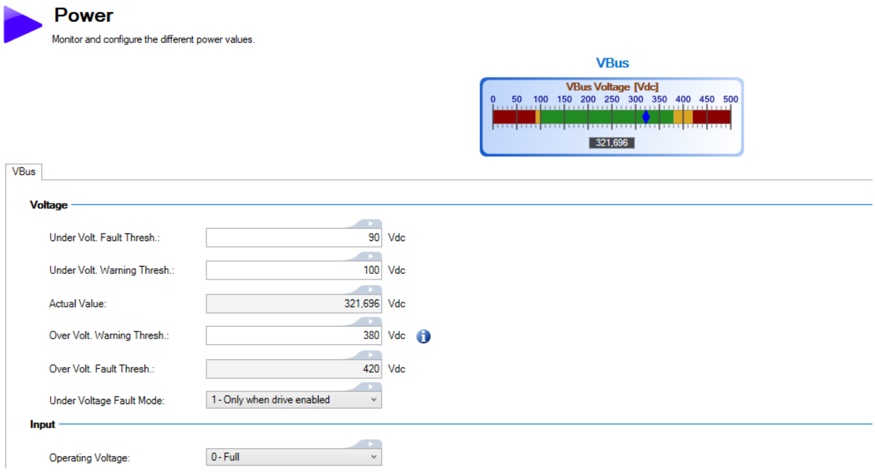

Figure C.2: Kollmorgen workbench power settings with relevant parameters.

C.1.3 Regen

An external regen resistor is attached to the system. A regen system is used when there is a large back EMF in the system, resulting in an overvoltage of the bus. The regen is nothing more than a resistor capable of large currents. A 33 ohm 500W regen resistor is chosen; however, since the "External Regen Heat up time" is unknown, the value is taken from the BAR-500-33 resistor, a similar model.

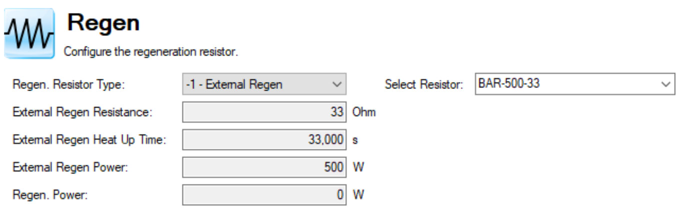

Figure C.3: Kollmorgen workbench regen settings with relevant parameters.

C.1.4 Feedback 1

Section feedback 1 is the primary feedback loop used in the system. Feedback 1 is the sine encoder (with the halls) connected to the AKD driver using connector X10. The feedback which is being used is the "20 - Sine Encoder with Halls". Since a third party motor is being used, the motor autoset should be turned off ("0 - Off"). The drive direction is set to 0, resulting in a positive direction when moving to the right (seen from the computer). According to the following calculations, the value for "Sine Cycles/ Magnet Pitch" is set to 2100. The magnet pitch is 42 mm, while the scale pitch of the optical encoder is 20 µm. Dividing the 42 mm by 20 µm will result in a "Sine Cycles/ Magnet Pitch" value of 2100.

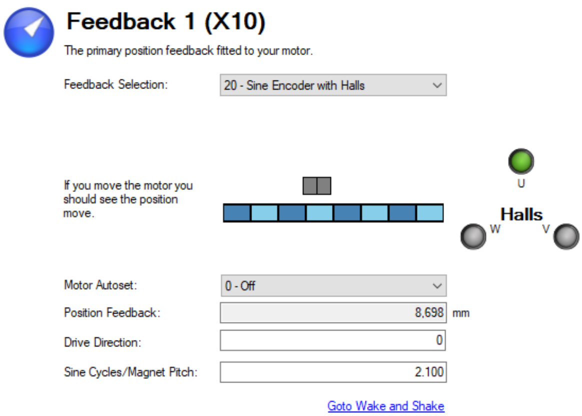

Figure C.4: Kollmorgen workbench feedback 1 settings with relevant parameters.

C.1.5 Feedback 2

Feedback 2 is not being used and will, therefore, not be discussed.

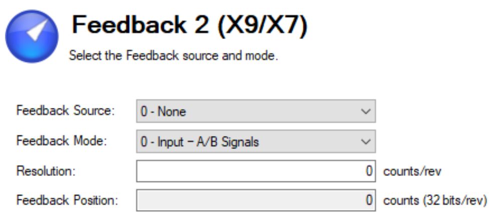

Figure C.5: Kollmorgen workbench feedback 2 settings with relevant parameters.

C.1.6 Encoder Emulation (X9cfg)

Emulation is not being used; therefore, the Emulation mode is set to "0 - Input (No EEO Output)".

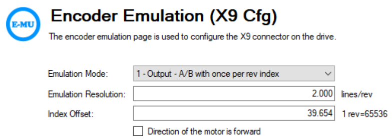

Figure C.6: Kollmorgen workbench encoder emulation settings with relevant parameters.

C.1.7 Analog input

Depending on how the stage is used, the analog input mode is chosen. The analog input cable is connected to connector X8 pin 9 and 10. More information on how to use the stage can be found in appendix E. When the stage is controlled using an analog input signal, it should be set to "1 - Command Source". When the stage is being used in service mode (using motion tasks), analog input mode "0 - Monitor" is sufficient. The analog input can be used to synchronize and merge the data captured using Kollmorgen Workbench. The first thing to do is adjust the input voltage back to zero; this prefills the offset. The lowpass filter should be set to a filter as low as possible (to avoid noise) but high enough to pass through the command signal. The following settings only hold true when using the analog input mode. The deadzone should be as small as possible (preferably 0.00V). The scale should be set as little as possible to avoid noise in the signal. Take, for example, the case where the motion is between +/- 20 mm. The scale should be set to 2 mm/V with an input of +/- 10 V. When the scale is set to a large value, a minimal amount of noise (in V) will result in a sizeable amount of unwanted motion.

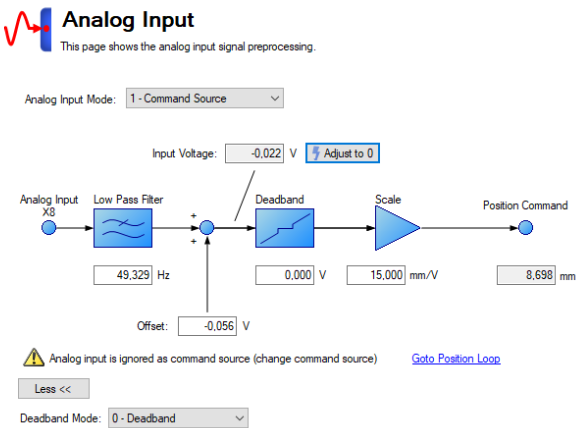

Figure C.7: Kollmorgen workbench analog input settings with relevant parameters.

C.1.8 Analog output

The analog output value can be set to the application for which it is being used without altering the system. The analog output can come in handy when monitoring, for example, the displacement of the system. The analog output cable is connected to connector X8 pin 7 and 8. It is again essential to choose the appropriate lowpass filter and scale. The chosen value (position feedback for example) is scaled and output as a voltage. An example of the settings is shown below.

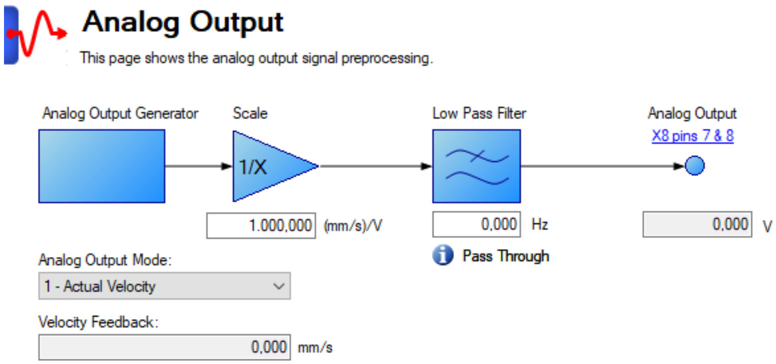

Figure C.8: Kollmorgen workbench analog output settings with relevant parameters.

C.1.9 Digital inputs and outputs

The digital inputs and outputs are being used for several use cases, from the limit switches to the led indicators. The two high-speed digital inputs are used for the limit switches. DIN 1 (X7 pin 10) is connected to "18 - Positive Limit switch", and DIN 2 (X7 pin 9) is connected to "19 - Negative limit switch", which are both active high. Digital input 3 (X7 pin 4) is used to reset a possible fault in the system. The two digital outputs are used for the indicators. DOUT 1 (X7 pin 7 and 8) is connected to the indicator light, which lights up when the axis is enabled (the stage is thus armed). DOUT 2 (X7 pin 5 and 6) is connected to the fault indicator light; when there is a fault in the system, the indicator will light up.

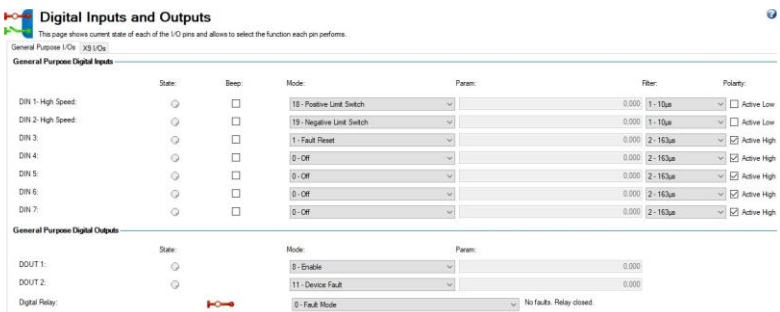

Figure C.9: Kollmorgen workbench digital input and output settings with relevant parameters.

C

C.1.10 Compare engines

The compare engines are not used and will thus not be discussed.

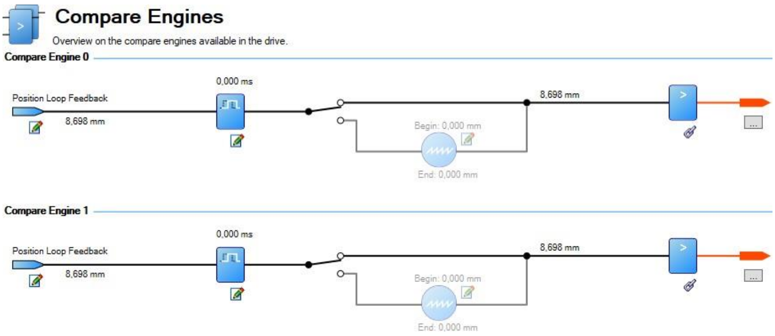

Figure C.10: Kollmorgen workbench compare engines settings with relevant parameters.

C.1.11 Position capture

This particular position capture section is not used and will thus not be discussed.

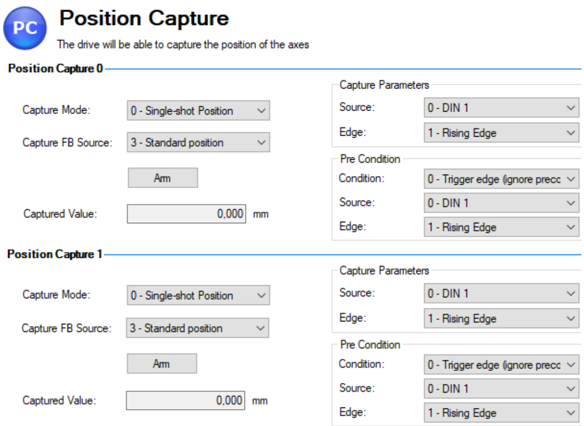

Figure C.11: Kollmorgen workbench position capture settings with relevant parameters.

C.1.12 Motion profile table

The motion profile can be used when the system is in service mode. A further explanation will be given in appendix E.4.

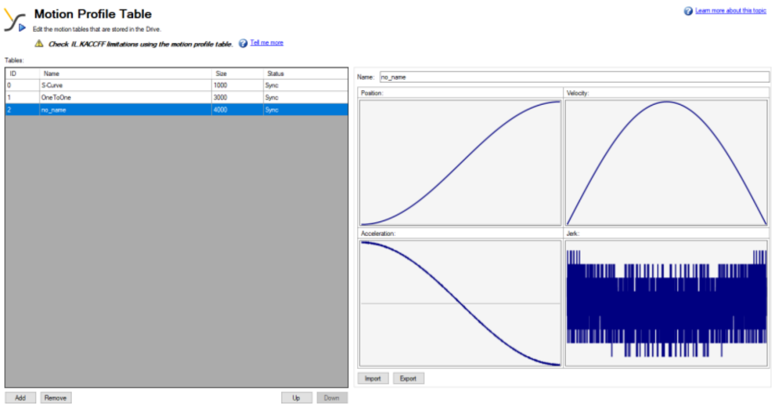

Figure C.12: Kollmorgen workbench motion profile table settings with relevant parameters.

C.2 Axis settings

The axis settings are the motor settings. Do not change these settings without consolidating an expert. Each setting will be discussed individually.

C.2.1 Feedback

The feedback setting configures the connection of feedbacks and loop sources for the axis. Since there is only one feedback system, every feedback should be set to "0 - Feedback 1" see the figure below.

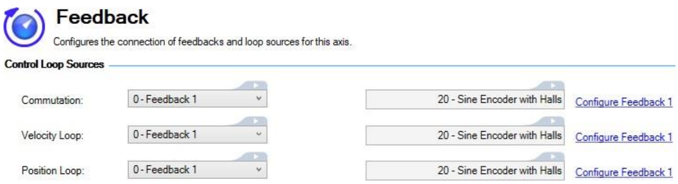

Figure C.13: Kollmorgen workbench axis feedback settings with relevant parameters.

C.2.2 Motor

The most crucial section is the motor section; **the parameters should not be changed**. The continuous and peak current are found in the motor's spec sheet (2.1 Arms and 7.0 Arms). The coil thermal constant determines how long it takes until the coil is at 63 % of the coil temperature. The formula is found to be motor.ctf0 = 1000/(te*2*pi), which results in a coil thermal constant of 2.2105 mHz. According to the spec sheet, the inductance is set to 6.5 mH, and the inductance saturation is set to 225 Arms. There are two motor poles; this value corresponds with the number of pole pairs. The motor has a phase shift of 120 degrees, as discussed in appendix A.1.1. The moving base is approximately 5 kg, according to PM bearings. The force constant, EMF constant, motor resistance, maximum voltage, maximum speed, and pole pitch are all found in the motor spec sheet and are depicted below.

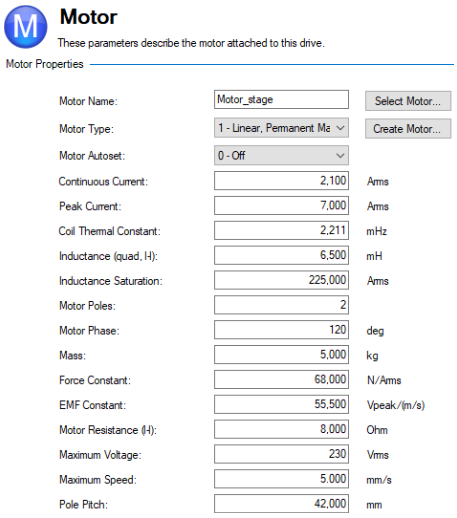

Figure C.14: Kollmorgen workbench axis motor settings with relevant parameters.

C.2.3 Foldback

Foldback determines how fast the motor heats up and is discussed in more detail in appendix B.6. It is crucial to check whether the peak and continuous current values correspond to the previously entered values.

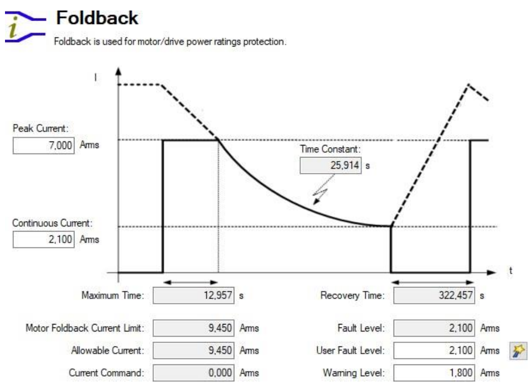

Figure C.15: Kollmorgen workbench foldback settings with relevant parameters.

C.2.4 Brake

No brake is fitted on the system (this would be a mechanical brake). Dynamical braking (braking on the motor), which is purely damping, can be performed by the stage. The brake state should be set to "0 - No brake fitted".

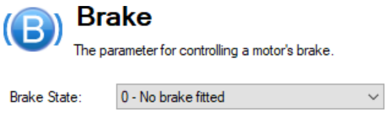

Figure C.16: Kollmorgen workbench brake settings with relevant parameters.

C.2.5 Units

The servo driver is currently configured to use mm instead of meters. It can be changed; however, the effect on the other components isn't evident. The Pole-Pair pitch should be set to 42.000 mm according to the motor section.

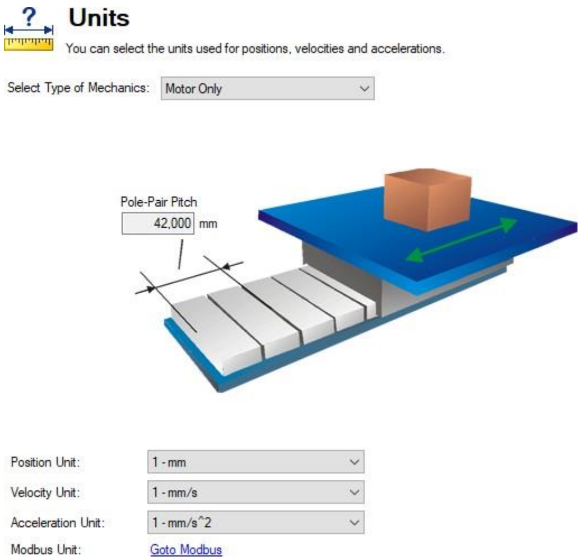

Figure C.17: Kollmorgen workbench units settings with relevant parameters.

C.2.6 Limits

The limits shown are a safety measure and are a combination of the previously entered values. The only new parameters are the user over-speed limit and the maximum position error. When these values are exceeded, a fault will be issued. The limit switches can be tested by moving the stage (make sure the stage is disabled) over the limit switches and see whether the indicator lights up, and a warning will be given.

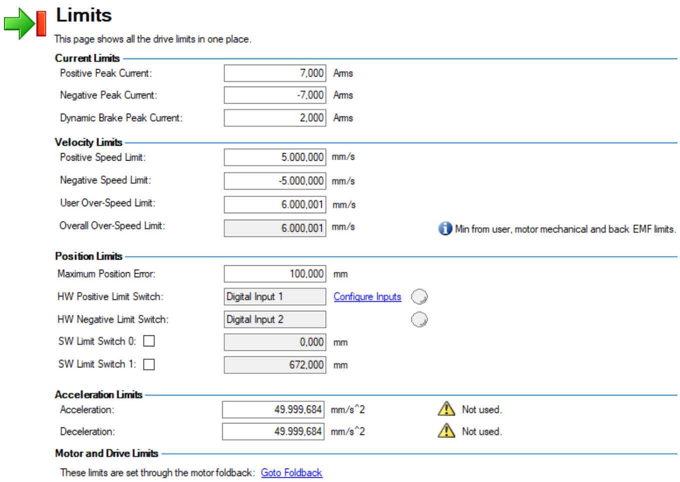

Figure C.18: Kollmorgen workbench limits settings with relevant parameters.

C.2.7 Home

When the stage is turned on, it will start with its homing procedure automatically. Homing is crucial when performing a displacement controlled motion. By homing, it determines the outer limits and finds the center of the track. The type of homing used is the "1 - find limit switch" method. It will move towards the positive limit switch from which it moves back 250mm, which is the (approximate) center of the track. The center of the stage is now the zero position; this is important when a motion moves around zero. The homing procedure can be done manually by clicking the start button. Homing will only start in service mode; therefore, it is essential to start the stage in service mode.

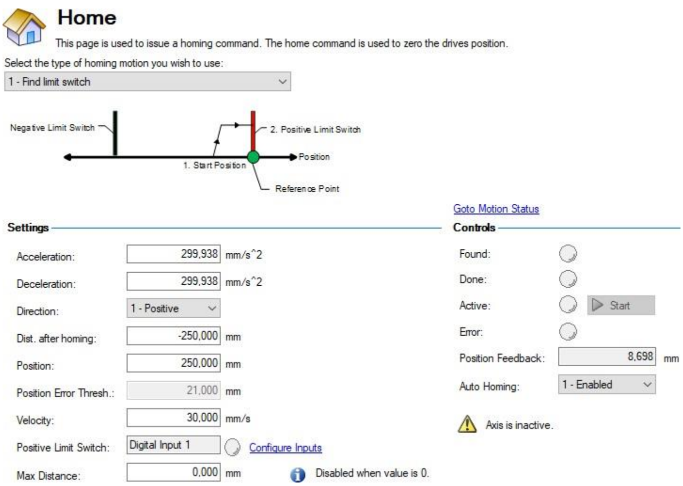

Figure C.19: Kollmorgen workbench home settings with relevant parameters.

C.2.8 Current loop

The working principle of the current loop is described in appendix A.4.1. Therefore, we will not discuss the working principle and only highlight the relevant parameters. The current offset, friction current, and viscous FF gain are set to 0; cogging compensation is also turned off. The following parameters can vary for different testing conditions. Therefore there are two files with mostly used testing conditions (service mode and analog input mode over the full range). For the PI controller, a proportional gain of around 40 V/A is often sufficient.

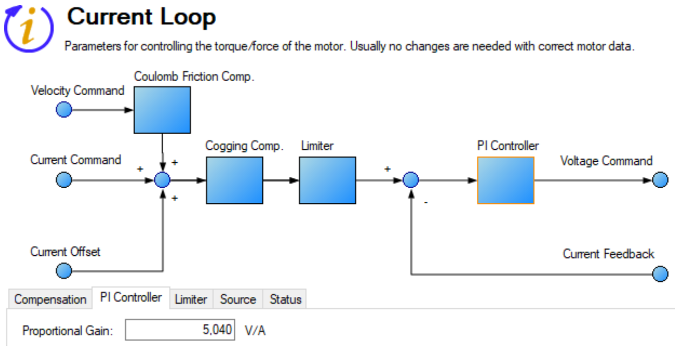

Figure C.20: Kollmorgen workbench current loop settings with relevant parameters.

C.2.9 Velocity loop

The working principle of the velocity loop is also discussed in appendix A.4.2. Only the relevant parameters will be highlighted. The ramp limiter (maximum acceleration) is set to an appropriate value for the use case. The velocity clamp (maximum velocity) is the same as the motors' top speed (5 m/s). The current parameters for different use cases can be found in saved parameters files on the computer (see Appendix E).

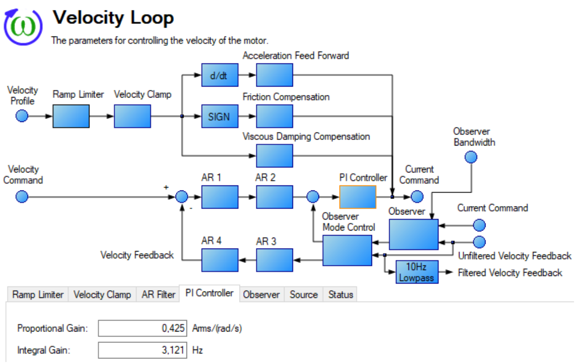

Figure C.21: Kollmorgen workbench velocity loop settings with relevant parameters.

C

C.2.10 Position loop

Again the working principle of the position loop is discussed in appendix A.4.3. The parameters vary for different use cases; therefore, the correct parameter file must be uploaded to the servo driver. When the values are set incorrectly, there is the chance of loud audible noise and possibly damage to the setup. Be cautious when changing these parameters, and do not hesitate to disable the system when there is a loud noise.

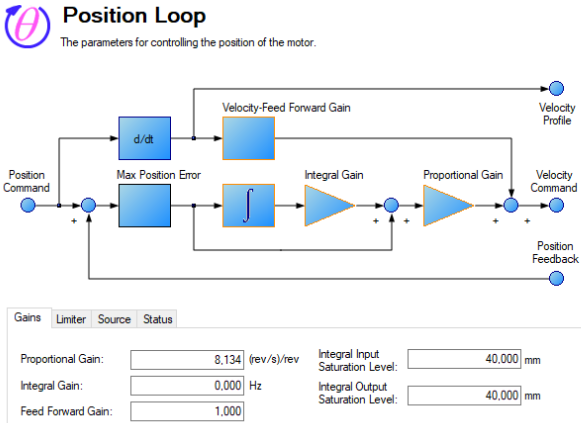

Figure C.22: Kollmorgen workbench position loop settings with relevant parameters.

C.2.11 Programmable limit switches

The setup uses hardware limit switches due to their reliability. There are no software limit switches configured. Software limit switches will not work when the homing procedure is not done correctly. The relevant parameters are shown below.

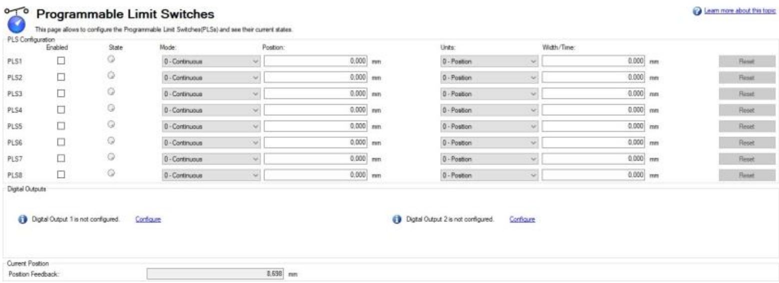

Figure C.23: Kollmorgen workbench limit switches settings with relevant parameters.

C.2.12 Enable/ Disable

The enable/ disable screen gives a good view of the status of the setup. The hardware is always enabled due to a bypass in the system (see electrical wiring, appendix D). The software is disabled by default at startup; the stage must be enabled using the Kollmorgen workbench before use; this is discussed in appendix E. The disable mode is used in such a manner that it will make a controlled stop and then dynamic brake after disabling. The relevant parameters are shown below:

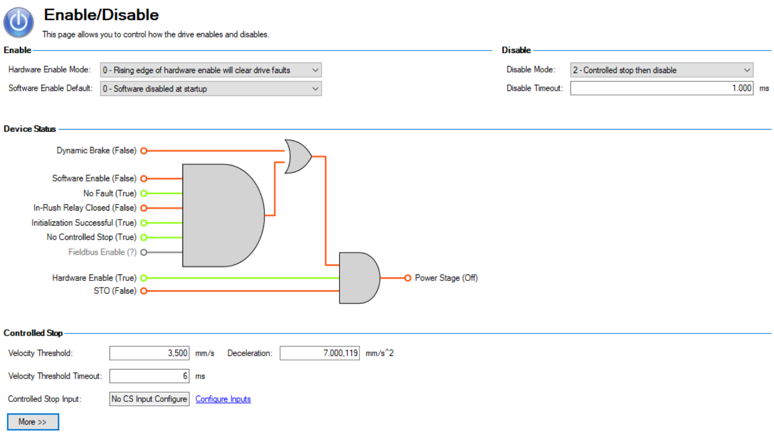

Figure C.24: Kollmorgen workbench enable disable settings with relevant parameters.

Appendix D
Air bearing stage - Electrical wiring

The air bearing stage setup has a lot of electrical components. These components range from power cables, led indicators to a precision optical encoder readhead. These components need to work together flawlessly to ensure a safe system. Since not all the components are directly compatible, some adjustments are made. There is a difference in termination resistance between the optical encoder and the servo driver. Therefore an additional termination resistor box (the stagefixer 4000) is created. In the first section, the electrical wiring in the enclosure is discussed. After that, the two data cables (going from the servo driver to the stage) are discussed.

D.1 Enclosure

The electrical enclosure houses most of the electrical components, as discussed in appendix A.5. The enclosure's primary goal is to remove any electrocution hazard and organize all the cables (see Fig. D.1). A single power cable (3x2.5 mm^2) is fed to the enclosure. The cable goes through an on/off switch, after which it is divided into the components. Inside the enclosure is a 24 V AC/DC power supply unit (Meanwell NDR120-24), which powers all the logical components. The power supply has an overcurrent protection, such that it will recover after the short is removed. An overview of the wiring can be seen in the figure below (see Fig. D.2). The connector X10 is left empty; this will be discussed in section D.2. The safety circuit and the latching relay will be highlighted to clarify the working principle.

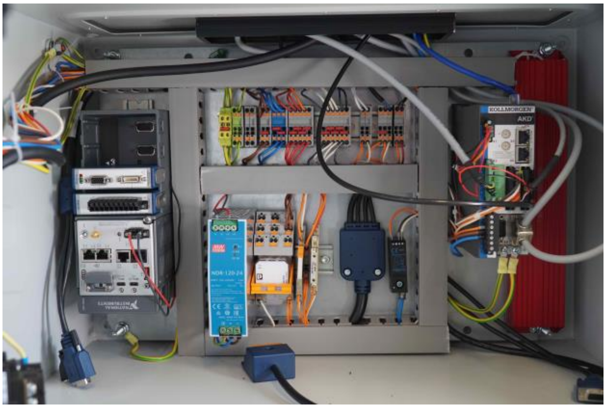

Figure D.1: Inside of the electrical enclosure with all the components. On the right hand side is the servo driver. On the left hand side is a National Instruments CRio which can be used in the future.

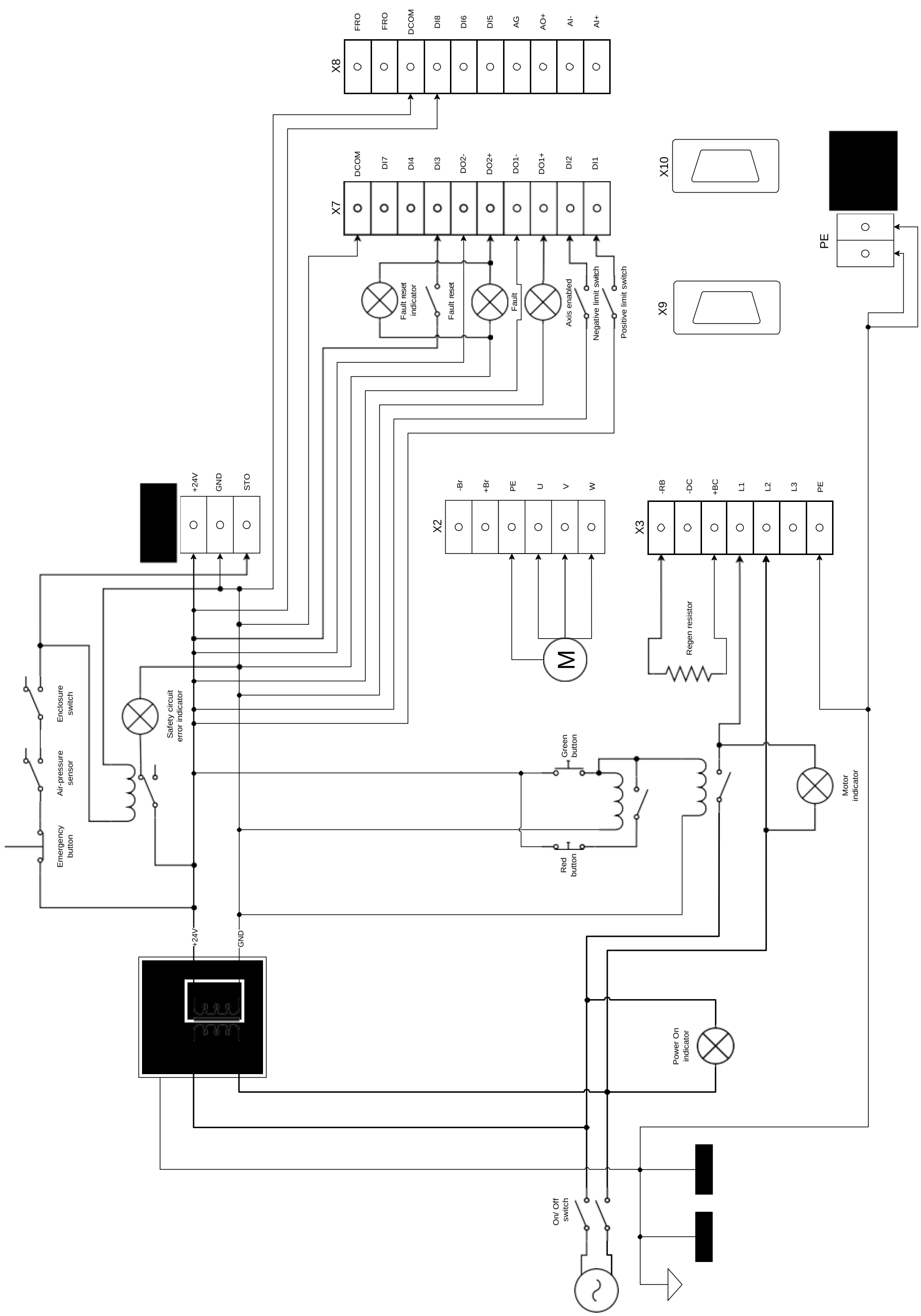

Figure D.2: Electral wiring diagram inside the controller enclosure.

D.1.1 Safety circuit

As discussed earlier, the safety circuit (or STO) is an important feature. When the safety line (24 V) is cut, the motors will stop immediately, and a fault will be issued. The safety circuit line starts by going through an emergency stop, which is a normally closed contact; when the button is pressed, the connection will be cut. After the emergency stop button is the air-pressure sensor, which measures the air pressure supplied to the stage. When the pressure is too low, it will open the contact; when the pressure is sufficient, it will close the contact. It is important to note that the sensor itself is also attached to the ground to use the indicator light on the sensor itself. Lastly is the enclosure switch; this switch is built in the physical enclosure. When the enclosure is opened, the contact will be opened as well. An indicator light is added to the system to make debugging easier. When the safety line is cut, an indicator light will light up. Since the indicator will light up when the line is cut, a relay is added. The relay is used as a normally closed relay.

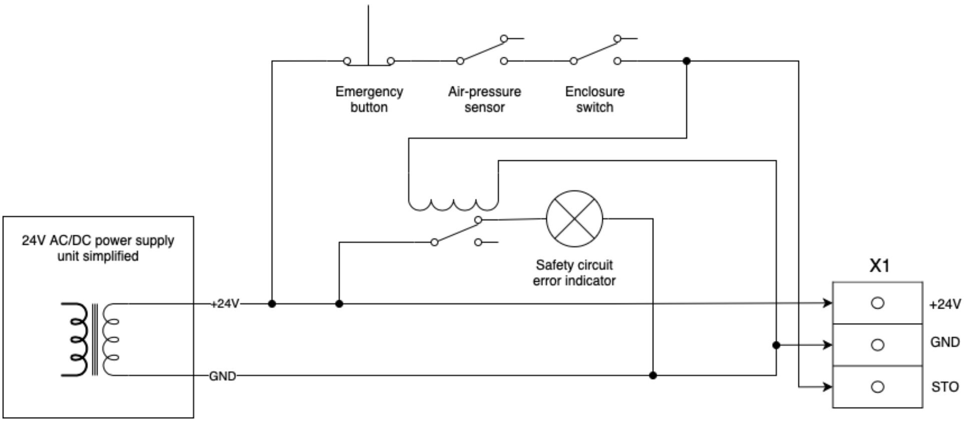

Figure D.3: Electrical diagram of the safety circuit (STO).

D.1.2 Motor power circuit

The servo driver needs two power sources, one logical power source (24 V) and one power source to supply the motors (230/380V). The power source to power the motors is provided to the bus bar. The bus bars'voltage can be seen in the Kollmorgen Workbench application, as discussed in appendix C.1.2. It is an extra safety feature to be able to stop supplying power to the bus. Since there is a large current going through the relay, two different relais are used. The first relay makes a latching circuit, which means the buttons only need to be pressed once to open the circuit instead of keeping them pushed in. The second relay is a larger relay used for larger currents connected to the bus and an indicator light. There are two buttons (a green and a red one) and an indicator light. The green button is connected to the normally open switch; the red button is connected to the normally closed switch. When the green button is pressed, the circuit will open; therefore, 24 V will be supplied to the larger relay. When the red button is pressed, the circuit is interrupted, closing both the small and large relay.

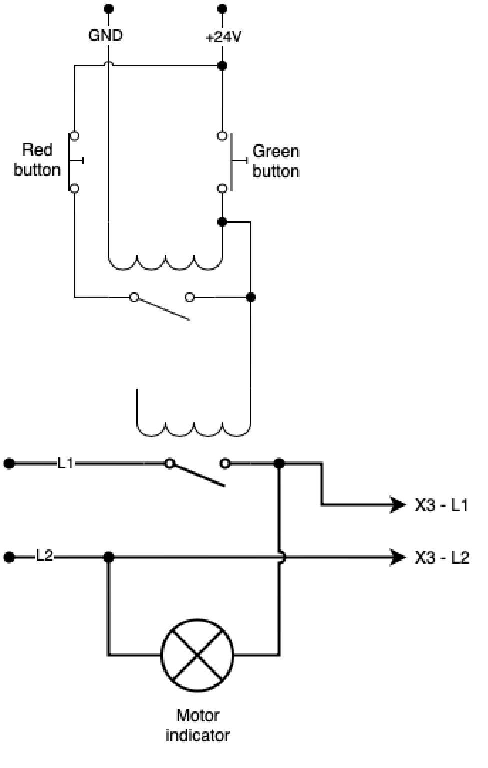

Figure D.4: Electrical diagram of the motor power circuit.

D

D.2 Data cables

There are several essential data cables between the servo driver and the stage itself. However, since the stage is not directly compatible with the servo driver, some of the wires are split to make it compatible, making it somewhat unclear. This section will discuss each cable between the stage and the servo driver. Three cables and an air hose are coming from/ going to the stage. The cables are depicted in figure D.5, which is captured from the air bearing stage manual as provided by PM bearings.

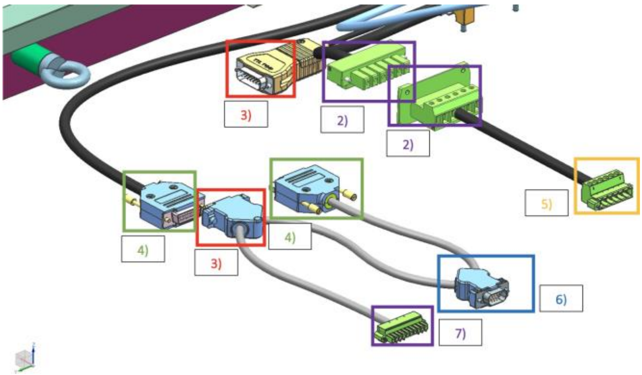

Figure D.5: Cable overview captured from the PM bearings manual.

The first cable is the motor cable (with connector 2), which uses four cores (U, V, W, PE). Since this cable is relatively straightforward (it is going directly into the servo driver), it will not be discussed. However, in the manual provided by PM bearings, an extension cable is depicted; this cable should not be used. The cable is too long, and the shielding is not connected, causing lots of electromagnetic interference. The second cable (connector 3) is the cable of the Renishaw readhead. This cable is quite fragile; some caution is required. At this point, the magic starts to happen. The Renishaw readhead captures the limit switches. Usually, this is transferred directly to the servo driver through the same connector. However, the servo driver requires the limit switches as two digital inputs. Therefore a cable is made between the Renishaw readhead and the AKD servo driver to divide those cores. Another problem is the incompatibility in termination resistance of the AKD servo driver and the readhead; therefore, a termination box is made. The termination box is also discussed below. The last cable coming from the stage is the motors' data cable (connector 4), which provides the hall sensor signals and the temperature sensor. As can be seen from the figure below, the two cables (motor data cable and the Renishaw readhead) are combined into two different cables. One cable is attached to the digital input, which are only three cores (com, positive limit switch, negative limit switch). The other cable is connected to the feedback port (X10) of the AKD servo driver. Since there was insufficient data a new wiring diagram is created and depicted below.

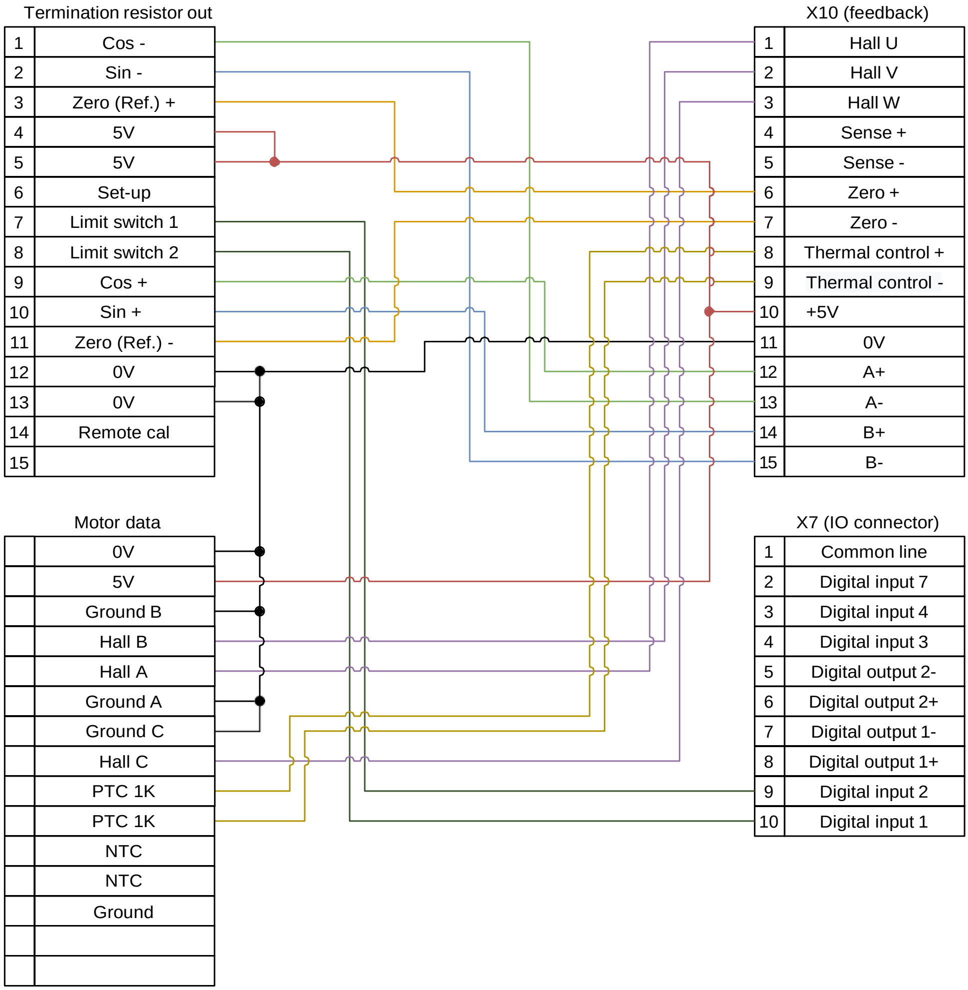

Figure D.6: Wiring diagram of the feedback system (motor and readhead data). This data was not supplied with the stage and is thus measured and documented for future reference.

D.2.1 Termination resistor

Since the AKD servo driver uses a different signal termination compared to the Renishaw Readhead, additional termination resistance needs to be added. A total of five resistors need to be added to make the system compatible. A schematic overview of the termination resistance box is shown below. Three termination resistors (120 ohms) are added between the cosine, sine, and reference to satisfy the recommended signal termination. Two more termination resistors (>10k ohms) are added to ensure that the current does not exceed 20mA. While this subsection is only five lines long, it took a long time to find out what was wrong due to poor documentation.

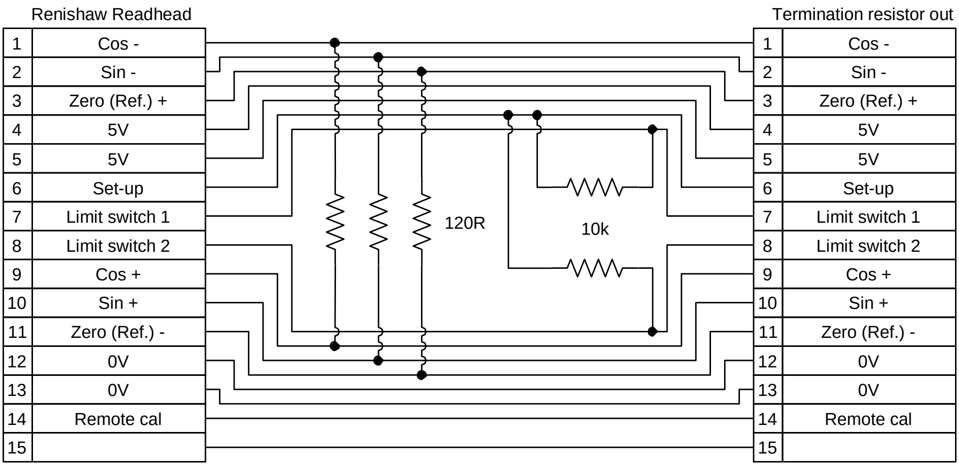

Figure D.7: Wiring diagram of the termination resistors to make the readhead compatible with the servo driver.

Appendix E
Air bearing stage - How to use guide

The linear air-bearing stage is a valuable piece of equipment and needs to be handled with care. Several safety features are built-in; however, the operator is still critical in ensuring a safe working principle. Please read this guide before using the setup and consolidate a trained user when experiencing any problems.

The stage can be used in three different modes using two different input modes. The three different control modes which can be used are force controlled, velocity controlled, and displacement controlled. It is recommended to use the displacement control mode due to the highest level of control. This guide will use the displacement controlled mode as a base. There are two ways of sending the displacement signal to the stage using an analog input and using motion tasks. When using an analog input, a BNC cable is connected to a function generator or any analog output device (as long as it is maximum +/- 10V). The analog signal is then captured by the servo driver, which converts the analog voltage value to a position. The servo driver will move to the desired location with a prescribed maximum acceleration. The second mode uses motion tasks; instead of using an analog input, the desired position is programmed in the servo driver using the software. The servo driver will perform each task (command to go to a particular position) in the given order. Both methods have their pros and cons, which will be listed below.

	Pro	**Con**
Analog input	- Ease of use - Ability to use every type of signal	- Analog signals are sensitive to noise - Due to noise; the system can't be as stiff
Motion tasks	- Motion can be described more precisely - Autotuner can be used for control and can be set stiffer	- Motion tasks can only perform periodic motions - Updating motion tasks takes a small amount of time - Using the motion task as a reference requires an extra step.

Both methods will be discussed in this guide. First, a quick explanation will be given on the hardware aspect. What steps need to be performed to power on the stage and start the motion. Next, a description of the software's basics will be given, after which it will split into two chapters, one explaining the analog input mode and the other describing the motion tasks.

E.1 Hardware

When you are at this point of reading this guide, you should know how the stage looks. Are you sitting next to it? Good.

The first step is turning on the air supply to the stage. The valve to turn on the air-supply is next to the pole on which the air filters are attached. Please do not adjust the air pressure; only open the valve and verify that the pressure is around 4 bar. The stage is now free to move; you can verify this by pushing it with your hand; you should feel no obstacles when moving it.

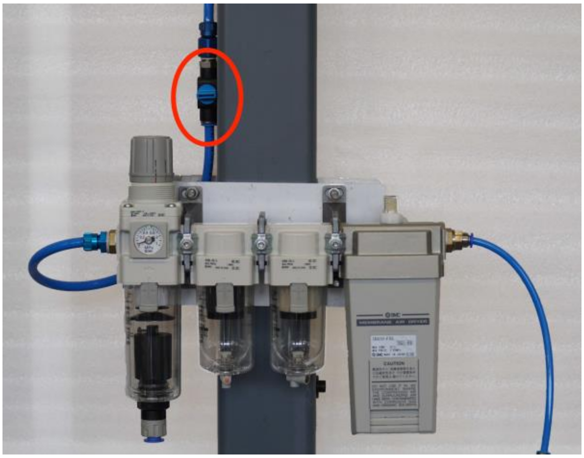

Figure E.1: Air supply line with the valve indicated in red.

The next step is powering on the stage and the computer. Check whether the stage's plug (under the table) is connected to the power outlet; if not, please do so. You can now turn on the stage by turning the red on-off switch on the control enclosure's lower left (see Fig. E.2). A few indicators will light up, the white power button, and probably the red safety circuit error; this is correct.

The indicators/ buttons all have their purpose. You do not need to touch any of the buttons yet.

- Power - this is the main power switch of the system, including all the logical controllers.
- Motor - this is a combination of a switch and indicator. By pressing the green button, the motor is supplied with electricity. Turning on the motor power does not mean that the stage will start to move. It will only supply power to the BUS rails. The indicator will turn on when it is turned on.
- Power on - this indicator will light up when the main power is supplied and the power switch is turned on.

Figure E.2: Outside of the controller enclosure with the interfacing features.

- Axis on - this indicator will light up when the stage is turned on. Please be cautious when the indicator is on.
- Fault reset - when there is a fault in the system, the button will light up; this fault can be reset using this button.
- Safety circuit error - if the safety circuit is cut, this indicator will light up. The three main safety features are discussed below.
- Fault - if there is a fault in the system, the indicator will light up.

When the safety circuit error lights up, there can be several causes. There are three safety features built-in when the indicator does not turn off, check whether one of the safety features is triggered.

1. Safety button - check whether the red safety button is not pressed. You can pull the red safety button to release it. Do not hesitate to push the button when something goes wrong.
2. Air-pressure - when the air pressure is too low, the safety circuit will be cut. Check whether the air pressure is right above 4 bar.
3. Physical enclosure - to prevent any mechanical hazard, an enclosure is fitted around the stage. When the lid is open, the stage will not turn on. Please close the lid to ensure safe working.

You probably want to attach your prototype to the stage. Attaching a prototype is easy using the mounting holes in the moving base. The mounting holes are M4 x 0.7 holes spaced apart, as shown in the figure below. It is essential to note that more bolts and nuts are on the stage; you should never loosen or adjust them since they are meant to adjust the air-bearing itself.

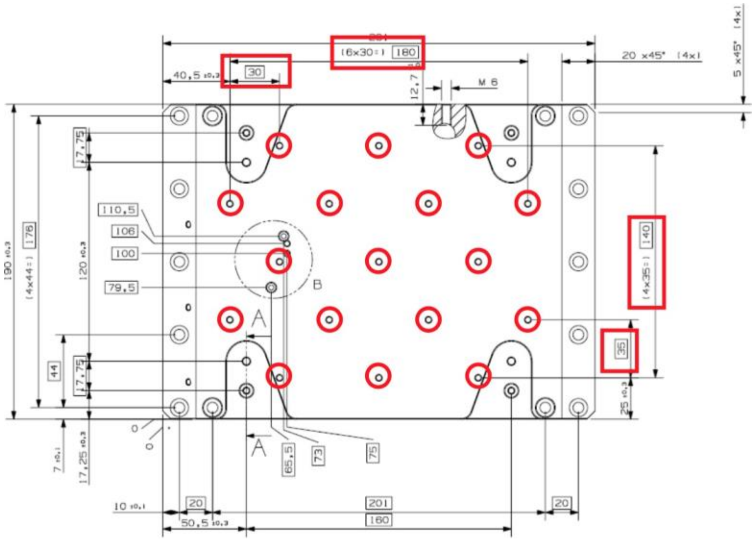

Figure E.3: M4 mounting holes on the stage, the holes encircled with red can be used. The mounting holes are 8mm deep.

E.2 Software

First, we will walk through the basics of the software which is being used. There is one main program we're using to control the stage; Kollmorgen Workbench. Kollmorgen Workbench is a program from AKD to control the servo driver. To get started, log in to the computer; this can be done using your personal TU Delft account and the local admin account (username: ".\localadmin", password: "Stage4000!"). After the computer has logged in, launch Kollmorgen Workbench. You will see a screen like shown below. Select the driver (Stage4000) in the quick start settings and hit the connect button.

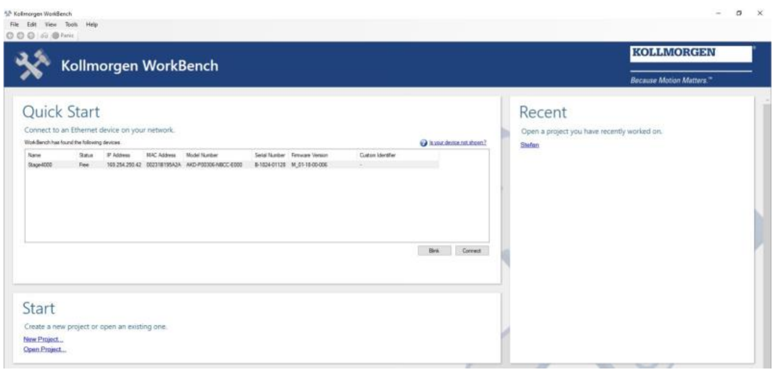

Figure E.4: Startup screen of Kollmorgen Workbench in which the servo driver can be selected and connected.

Possibly you get a popup that asks you whether it should download the local parameters to the host and vice versa. Select "download local parameters to host." Hitting the other button does not influence the system significantly. Now you will see a screen like shown in figure ; welcome to the Kollmorgen workbench. First, a few essential elements will be explained. Don't be afraid; the stage will not start moving without you telling it.

In the figure below, you see the home screen of Kollmorgen. The screen is divided into four essential sections. The usage of each section will be discussed below. Section 1 is the menu and toolbar, section 2 is the device list, and section 3 is the status bar.

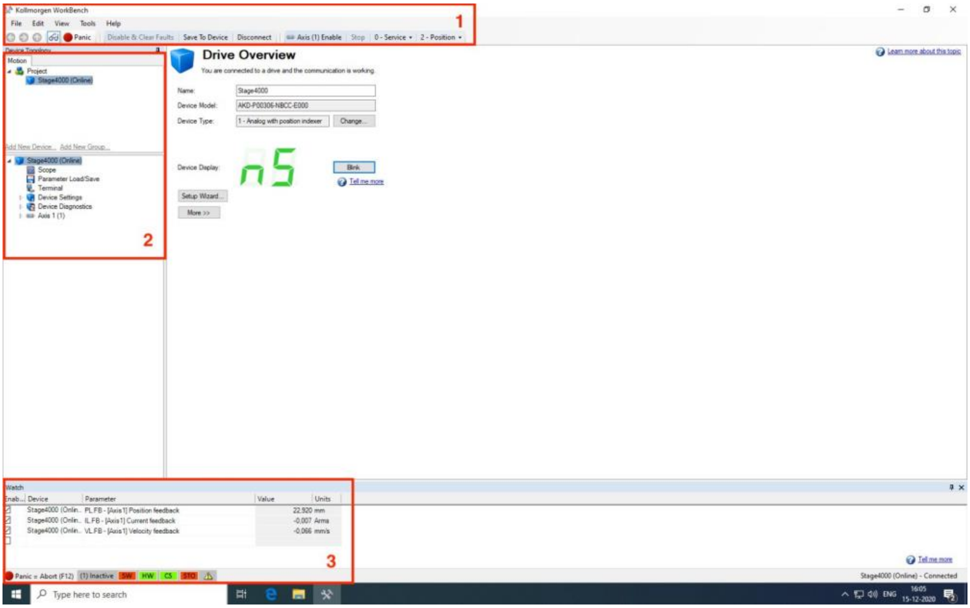

Figure E.5: Home screen of Kollmorgen Workbench with the 3 main sections highlighted in the red boxes.

E.2.1 Menu and toolbar

The upper menu is familiar with programs you've probably used before and will therefore not be discussed in-depth. However, it can be useful to know that you can save your project (with its settings) to a specific file. The toolbar essential when using the stage; it

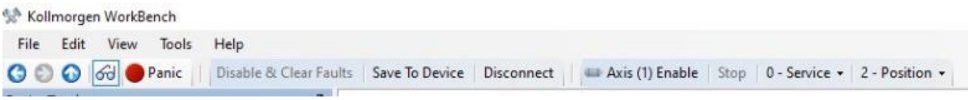

Figure E.6: Menu bar of Kollmorgen Workbench.

holds some of the most used buttons. The buttons will be discussed when going from left to right.

- Back, forward, up; these buttons speak for themselves.

- Toggle watch panel; when clicking the button, the lower watch panel disappears.
- Panic button (F12); this is a critical button; when you press it, the stage will stop immediately and issue a fault. The panic button is an emergency button; only use it when necessary (there is a chance of slamming the end stops when powered off incorrectly).
- Disable & Clear faults; when there is an error in the stage, you need to clear all the faults. Most common faults (overspeed, safety circuit, position errors) can be cleared this way (or by pressing the reset button on the enclosure. A significant fault should be handled by lab support or a trained user.
- Save to device; when you made changes to the device, it can be useful to store them in its memory. When you close the software, all settings won't be lost.
- Disconnect; this button can be used to disconnect the drive. You don't need this button.

- Axis (1) enable; this button is used to enable the stage. Be cautious when pressing this button. Do not press this button yet.
- Stop; it stops the motion command and does not work when the analog input is used as a control signal.
- Command source; using this selector, you can choose which command source you would like to use. Only the Service and Analog mode will be discussed.
- Operation mode; this determines which level of control you want, torque, velocity, or position. It is recommended to use the position mode.

E.2.2 Device list

The device list only shows up when the servo driver is connected (see Fig. E.7). This device list is used to change the parameters. There are four bullets which we'll be discussing and using. **Do not change the axis settings** as this may cause damage to the motors.

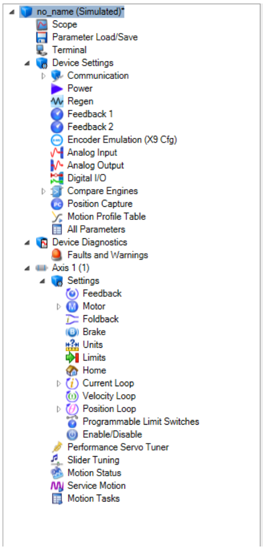

Figure E.7: Device list and settings in Kollmorgen Workbench.

The scope is used to record data inside the Kollmorgen. When you want to record more than one signal (since there is only one analog output), you can choose to use the scope. The scope can record up to 10,000 samples; this is not a whole lot. You can record six different sources; this can be, for example, the analog input, the position command, the position feedback, and many more signals. In the time-base and trigger tab, you can select for how long and with which sample rate the scope should record.

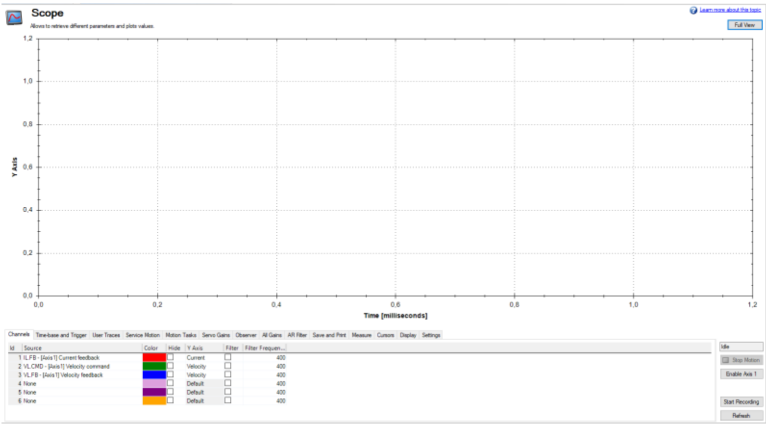

Figure E.8: Scope viewer in Kollmorgen Workbench.

Parameters Load/Save is used to upload the parameters which set the correct settings for the PID loop. This section will be elaborated later on.

Device settings - only two device settings (analog input/output) may be changed. The other settings should not be changed. The analog output can be configured to the desired output. This output is scaled from the selected parameter to a voltage. The analog output can, for example, be used to record the actual position of the stage. Try to scale the analog output to the expected output such that the voltage is as large as possible.

Axis 1 - motion tasks - these motion tasks are one way to control the stage. A more elaborate explanation will be given later on in section E.4.

E.2.3 Status bar

The status bar gives you all the information you need in a blink of the eye. Above the status bar is the watch panel, which shows some parameters. You can set these parameters to the ones you like. A useful parameter is the Foldback current limit (IL.MIFOLD); this shows the maximum allowable current supplied to the stage. The stage can only handle a large amount of current for a short period. This current decreases when the stage is pushed to its limit; when you see this value decaying quickly, you know you are working on the stage's limits. Below the watch panel is the axis status, which shows four blocks. Software enable (SW) tells you whether the stage is enabled by software. Hardware enable (HW) tells you whether the stage is enabled by hardware; this value should always be true. The controlled stop is green unless the system is stopped in software. The safety circuit (STO) should be green as well for the stage to turn on. When you click the axis status, an enlarged view will be shown with all the conditions to be met for the stage to turn on.

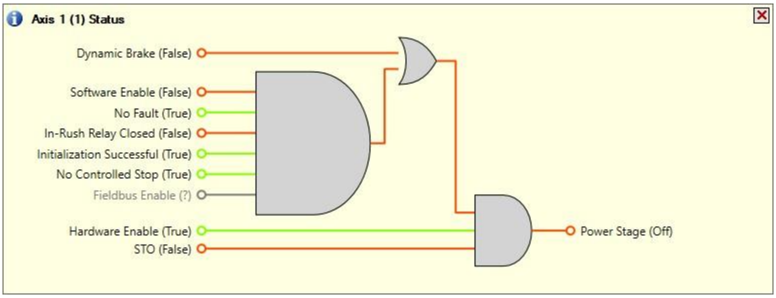

Figure E.9: Axis status as shown in Kollmorgen Workbench.

E.3 Usage

At this point, you know the very basics of the Kollmorgen software and hardware. Now we will do a step by step guide on how to use it. When you are at this point, please check the following:

- The air supply is turned on.
- The main power switch is turned on.

- All the safety conditions are met (air-pressure, the enclosure is closed, and the emergency button is not pressed).
- You know which operation mode you'll be using (motion tasks or analog mode).
- The fault indicators aren't light up.

This guide will now split up into two sections; when using analog control, continue reading. When using motion control, please proceed to Sec. E.4.

E.3.1 Analog mode

The first thing we need to do is import the correct parameter file. To do this, head to Parameters Load/Save and click Load from file. Select the file "Kollmorgen_parameters_analog". The correct parameters for the PID are now imported.

The next thing we need to do is set the analog input settings since we're going to use that. Head to device settings - analog input and fill in the correct parameters. Ensure that the input signal is as large as possible (thus as close as possible to +/-10V) and the analog input mode is set to command source. The scale can now be set to the appropriate value. Do the same for the analog output if necessary. Ensure the analog input is connected to the function generator or signal generator through the BNC connector and start hitting the "Adjust to 0" button. Do the same for the analog output (select the analog output mode and the scale factor).

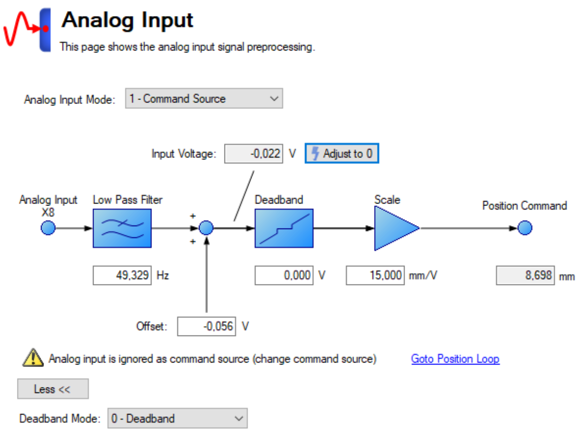

Figure E.10: Kollmorgen workbench analog input settings with relevant parameters.

We're almost done, don't worry. We first need to home the stage (determine where the center of the track is). Follow the following steps:

1. In the upper toolbar, select "0 - service" mode (even though we're going to use analog mode) and "2 - position" mode.
2. Turn on the motor power by pressing the green switch on the enclosure.
3. Press the "Axis (1) enable" button in the upper toolbar.

4. The stage will start to move (and you'll probably hear a high pitch noise), don't worry; it's now homing (determining where the middle is).

5. The stage will now return to the middle of the air bearing track; this is 250mm from each side.

At this point, we can start switching to the analog mode; this is done by changing the control mode in the upper toolbar from "0 - Service" to "3 - Analog". The stage will make an audible noise; this is correct; this is the analog input noise, which is being amplified. You can now start your signal generator and start measuring; good luck!

Some tips and tricks:

- When you're done measuring, disable the stage.
- When you are again starting with a new measurement, the stage may not be at the zero position (0 mm). When you turn on the stage (while it is not at zero) and the input is zero, the stage will jump as fast as possible back. This jump happens with such high acceleration that it may damage your prototype.
- When the situation above occurs, before enabling the axis, switch to "0 - Service" mode and head to the axis settings menu, and click Motion tasks. Now you'll see some motion tasks of which one is probably 0mm. Select this one and hit the start button. The stage will move back to zero, after which you can switch back to analog mode.
- Use the scope to measure data, and include the same signal as you use for the analog output. This way, you can merge the two data streams.

E.4 Motion tasks

he first thing we need to do is import the correct parameter file. To do this, head to Parameters Load/Save and click Load from file. Select the file "Kollmorgen_parameters_motion_task". The correct parameters for the PID are now imported.

The next thing we need to do is set the motion tasks. A motion task describes how the stage moves from one position to another. The motion tasks can be found in Axis 1 (1) - Motion tasks. A motion task needs several input parameters, the position which it needs to move towards, the velocity (which is the maximum velocity), the acceleration, and deceleration. The acceleration and deceleration are used to reach the command velocity.

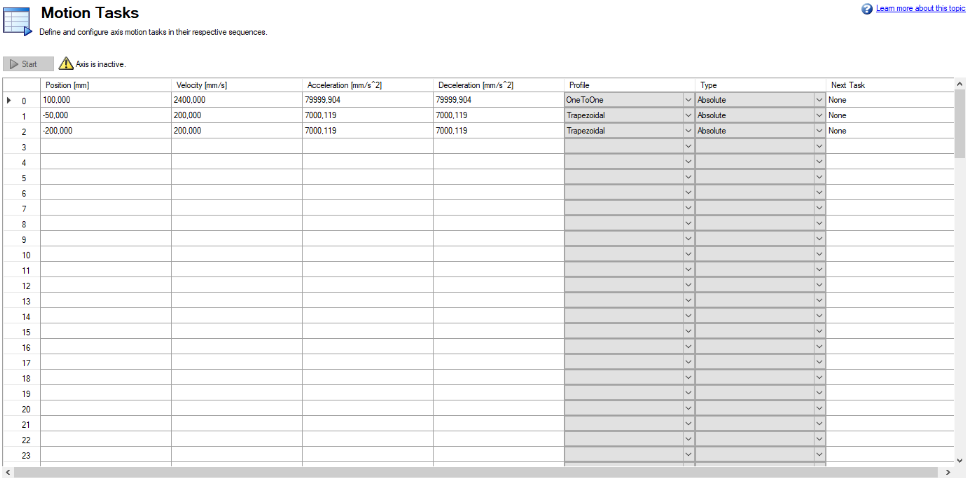

Figure E.11: Kollmorgen workbench motion task table.

When you click a motion task, you get a popup screen to set the relevant parameters. The motion task has a lot of features; only some relevant ones will be highlighted. Please note that using this feature is not recommended when doing a sine sweep. A velocity profile defines the motion task; this determines how the stage will move from one point to another. Usually, the profile is set to trapezoidal; however, a custom motion profile can be made in the motion profile table setting.

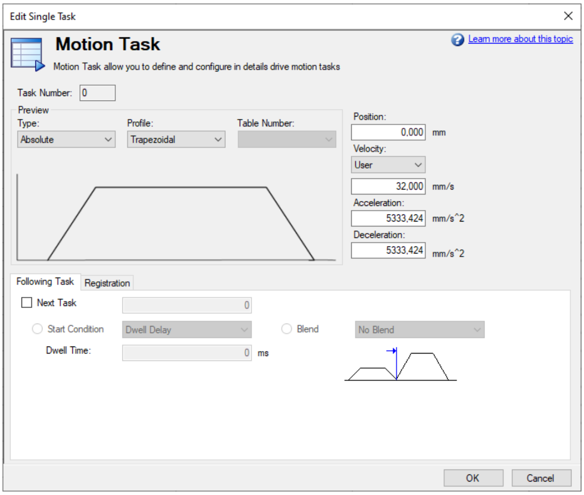

Figure E.12: Kollmorgen workbench motion task popup when creating a new motion task.

To create a custom motion profile, head to the motion profile table tab in the device settings. Opening the page will load the preinstalled motion profiles on the stage. You can also make your custom motion profile using, for example, MatLab. The motion profile describes how the motion moves from point A (located at 0) to point B (located at some value). The position of point B is entered in the motion tasks. The motion profile table only describes the shape of the motion.

The motion profile can be imported as a CSV file with 1000-4000 records. The first value should always be zero, and the last value should always be $2^{32} - 1$. The values should be in ascending order.

Let's walk through a simple example; the stage needs to move from 0 mm to 200 mm with a position profile of $x = 1 - \cos(\omega t)$, which the motion profile is depicted below.

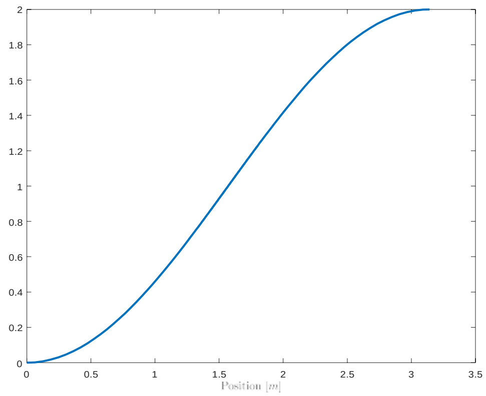

Figure E.13: Motion profile of $x = 1 - \cos(\omega t)$ as described above.

We first create a time vector in MatLab of 4000 samples, ranging from t = 0 to t = pi/omega. This way, we start from 0 and end at the top position. The next thing we need to do is calculate the position for each of the time samples. After doing this, we need to scale the output by first normalizing it to zero (to do this, we divide it by the maximum value). After that, we multiply it with $2^{32} - 1$. This vector is saved to a CSV file, which can be imported as a motion profile table. Do not forget to round the values since decimal values aren'taccepted.

We're almost done, don't worry; make sure the motion tasks are all set and done. We first need to home the stage (determine where the center of the track is). Follow the following steps:

1. In the upper toolbar, select "0 - service" mode and "2 - position" mode.
2. Turn on the motor power by pressing the green switch on the enclosure.
3. Press the "Axis (1) enable" button in the upper toolbar.
4. The stage will start to move (and you'll probably hear a high pitch noise), don't worry; it's now homing (determining where the middle is)
5. The stage will now return to the middle of the air bearing track; this is 250mm from each side.

At this point, we can start performing motion tasks. Head to the motion task page, select the motion task you like to perform, and hit start. The stage will now start moving. Good luck measuring!

Some tips and tricks:

- When you're done measuring, disable the stage.
- When you want to measure using the scope and an external DAQ, consider a cable between the DAQ and the analog output or input. By measuring the same data stream on both the scope and the DAQ, you can merge the data later.
- In the scope settings, you can set a trigger for the scope to start measuring. This way, your measurement will always start at the same timestamp.

Appendix F
Numerical modeling - different load paths

The nonlinear spring used in chapter 4 has two different load paths. Having two different load paths creates a new challenge to the system. First, this load path needs to be cut in two to differentiate the load path for different directions. After that, the load path needs to be fitted to find the correct force-deflection curve. After that, there are two different methods in solving the ODE equation with the load paths. Finally, the potential energy levels need to be calculated for the two different load paths, which bring additional challenges.

F.1 Splitting the load paths

The first step is to split the load path found using Ansys. The output of the Ansys script is a displacement controlled force-deflection curve going back and forth, as shown below. Since the direction is not yet known, the load path is first split at the maximum force.

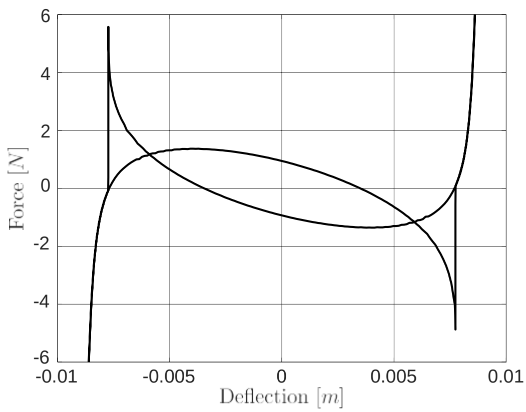

Figure F.1: Force deflection curve as found using Ansys

When this is the first or last index of the dataset, the split point is determined at the minimum. The direction is found by determining the derivative of the displacement points of the force-deflection curve. The split force-deflection curve with the direction drawn in is shown in the figure below.

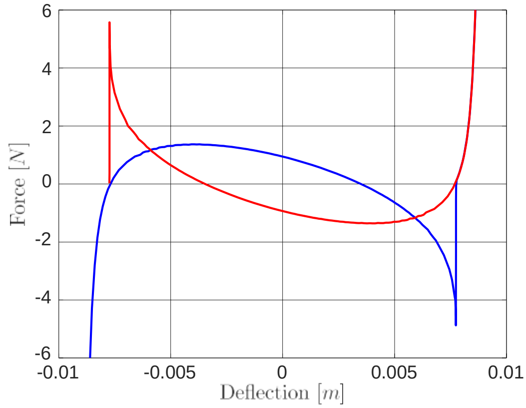

Figure F.2: Splitted force deflection curve with direction dependence.

F.2 Curve fitting the load paths

The numerical data points need to be fitted into a function. This function is used as the spring force in the ODE model. Linear interpolation is used to find the corresponding fitted force function.

F.3 Implementing ODE equations

There are two ways of implementing the new force functions in the ODE solver. The first method uses global variables to determine in which state it is. The second method uses events, which are less prone to errors.

F.3.1 Global variables

In the first method, global variables are used to simulate the two different load paths. Two new functions are introduced in Matlab, "setGlobalK" and "getGlobalK". The function "setGlobalK" is used to set K's value (which describes the load path you are following). The function "getGlobalK" outputs K's value. When using the global variables, an output function for the ODE solver is used. Every time a successful iteration step is completed, the output function determines whether the calculation is still in the correct load path. The output function checks what the current load path (K) is and what the position of the proof mass relative to the frame is. When the proof mass displacement is beyond the different load path's stable point, K is changed (using "setGlobalK"). The ODE function first checks which load path to use by reading the K value through "getGlobalK". A possible danger is the usage of global variables. Global variables are typically not recommended; however, in this case, values between different functions need to be interchanged; therefore, global variables are justified.

F.3.2 Events

The second method to switch between load paths is using events. When using an ODE event, the solver is stopped when meeting a specific condition. In our case, two conditions need to be met. First, the proof mass's position must be beyond the stable point; and the second condition describes that it needs to pass the stable point of the opposite direction. When the condition is met, the ODE solver is terminated. A new ODE solver needs to be started with new initial conditions and a new load path. Using events makes the solver suitable for parallel programming, which isn't the case with global variables. However, the events function is also used for the modified coefficient of restitution. Therefore one might consider using global variables.

F.4 Potential energy

The last and final step is to determine the potential energy of the system. Calculating a nonlinear spring's potential energy is somewhat more challenging than calculating a linear spring's potential energy. We again need the two direction-dependent force-deflection curves as calculated above (see Sec. F.1). The first thing we need to do is to determine the stable positions. At these stable position, the potential energy is assumed to be zero. We start to integrate numerically from one stable point towards the other stable point (see blue line in Fig. F.3). Next, we start to integrate towards the end-stop / stiff side (see red line in Fig. F.3). After combining these two measurements, we find the potential energy curve for one stable point. This procedure is now also done for the other stable point to find the potential energy.

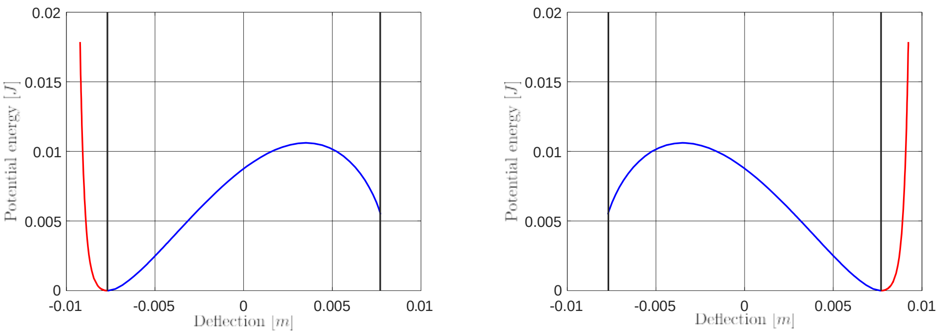

(a) Starting from the left stable point.

(b) Starting from the right stable point.

Figure F.3: Potential energy curves for two stable points. Vertical lines indicate the position of the stable points.

It is important to note that there is an extra step in the data processing when using global variables since snap points aren't stored. When using events, the snap points can be stored; this is where the potential energy curve needs to be changed. One interesting thing to note is the loss of energy when snapping.

Appendix G
Numerical modeling - damping

The most challenging part of the numerical modeling turned out to be the damping force. Multiple types of damping forces are investigated to find what was the best. First, the linear damping coefficient was determined from the prototype. The first simulation only had linear damping, which will be discussed in appendix G.2. After that, a cubic damping term is added (see App. G.3). Due to the inability to estimate the nonlinear damping coefficient, the model was switched to a coefficient of restitution. However, since the coefficient of restitution would assume infinite stiffness in the end-stops, the model is modified to a new model to represent the end stops of the nonlinear flexure (the bounce loss coefficient). First, the method to find the damping factor and coefficient of restitution is discussed, after which each form of damping is discussed.

G.1 Damping parameters

G.1.1 Linear damping coefficient

The first step is to find the linear damping coefficient of the prototype. The logarithmic decrement method is used to find the damping coefficient. First, the logarithmic decrement itself is determined, see Eq. G.1, where δ is the logarithmic decrement, n the number of peaks, x the amplitude of the peaks, and T the period. Next, the damping ratio is determined; see Eq. G.2, where ζ is the damping ratio, c_c the critical damping and c the actual damping. Finally, the critical damping is determined for the system (see Eq. G.3), where m is the mass of the proof mass and ω_n is the eigenfrequency of the system.

$$\delta = \frac{1}{n} \ln \frac{x(t)}{x(t+nT)} \tag{G.1}$$

$$\zeta = \frac{1}{\sqrt{1+\left(\frac{2\pi}{\delta}\right)^2}} = \frac{c_c}{c} \tag{G.2}$$

$$c_c = 2m\omega_n \tag{G.3}$$

The nonlinear spring is measured in the same manner as discussed in chapter 4, using a Keyence LK-H502 laser sensor. The spring is manually given a small perturbation to see how it damps out. The resulting time displacement diagram is shown below.

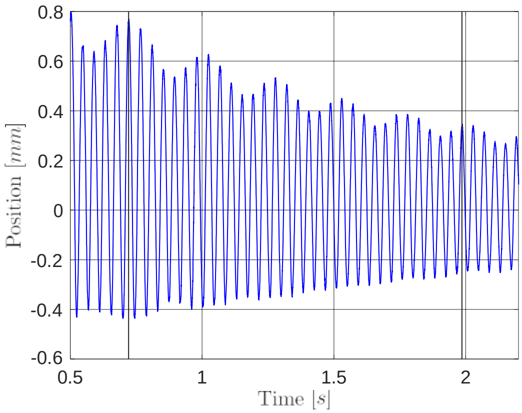

Figure G.1: Position of the unforced system when given a small perturbation to find the damping ratio. Vertical lines indicate the data points which are being used for the logarithmic decrement method

When performing the calculations, the linear damping coefficient is found to be: $c = 0.074483 Ns/m$.

G.1.2 Coefficient of restitution

The next step is to find the coefficient of restitution. The same setup as above is used; however, this time, the perturbation is large enough to snap from one stable state to another. The proof mass displacement is measured using the laser sensor and then numerically differentiated to find the velocity. The velocity is filtered using a lowpass filter at 150 Hz, far below the resonant frequency of 22 Hz. The displacement and velocity are shown in a single figure below. The velocity signal follows two different sinusoidal waves, one with a large amplitude low frequency and a higher frequency and lower amplitude. The higher frequency velocity is due to the proof mass's rotation (which was noted during experimental testing). Therefore only the large amplitude vibration is taken into account. The velocity right before impact is at -0.2116 m/s, depicted by the line and the red dot where it crosses. The velocity after impact is taken as the maximum velocity after the rebound, which is 0.1569 m/s. Using the maximum velocity after impact is not how the coefficient of restitution is defined. However, since we are dealing with end-stops with finite stiffness, the velocity if not directly rebounded after hitting the end-stop. One might argue that the coefficient of restitution is higher since energy is lost due to damping. However, since the damping factor is so small, the influence might be neglected. The coefficient of restitution is found to be 0.74.

G

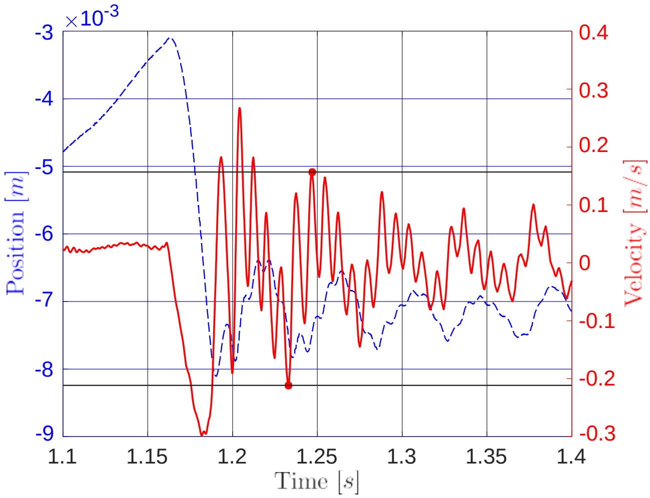

Figure G.2: Data used to find the coefficient op restitution. Both the position (blue) and velocity (red) signal of the proof mass are shown when it is pushed from one stable state to the other.

G.2 Linear damping

The first method used was linear damping, the simplest form of damping. The linear damping is described by equation G.4, where $\dot{u}$ is the relative velocity between the frame and the proof mass.

$$F_d = c\dot{u} \tag{G.4}$$

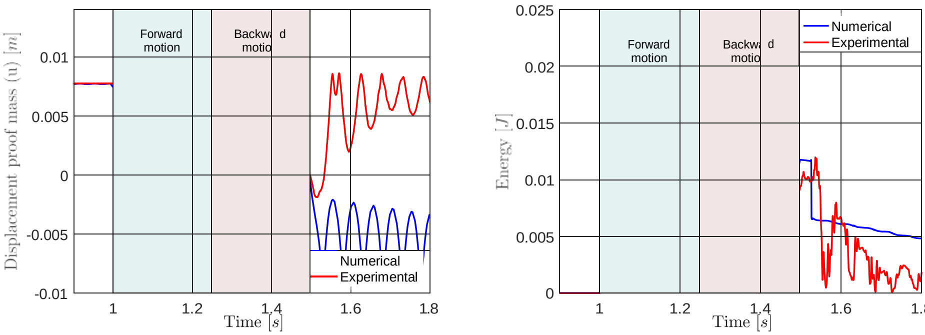

(a) Time displacement signal.

(b) Time energy signal.

Figure G.3: Results when using linear damping with a damping coefficient of $c = 0.074483Ns/m$. The blue lines indicates the numerical result, the red line the experimental result.

There are some interesting things we can make up from the figure shown above. First, the displacement signal is analyzed; after that, the energy signal is analyzed. We can note that the analytical model bounces back way further than the experimental model. More energy is lost when hitting the end stops in the experimental modal than in the analytical model. The next thing to note is the increasing amplitude in the deceleration section, after which it bounces back to the other side. The final position is thus also in the wrong stable state. When looking at the linear model's total energy plot, there are two main things to note. The numerical model's energy is way higher after snapping; this corresponds with the bouncing back behavior, as seen in the displacement plot. The second thing to note is the numerical energy step after the deceleration; this step is due to snapping to the other stable point. During this snap, energy is lost.

Since we now know that the linear damping coefficient is too low, we increase it till there is a good fit between the numerical and experimental displacement. Which is found at a linear damping coefficient of $c = 0.7Ns/m$

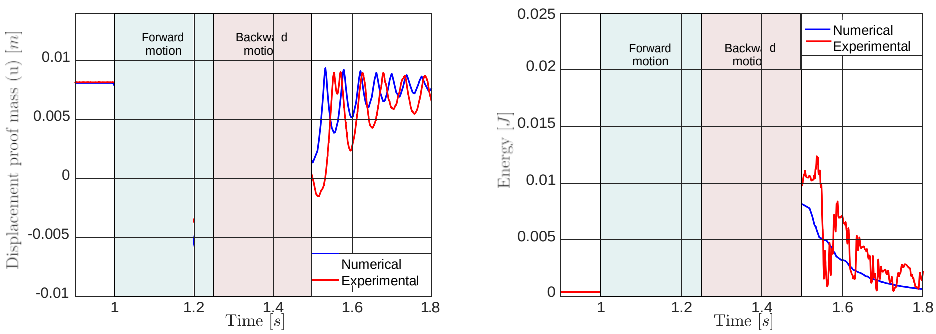

(a) Time displacement signal. **(b)** Time energy signal.

Figure G.4: Results when using linear damping with a damping coefficient of $c = 0.7Ns/m$. The blue lines indicates the numerical result, the red line the experimental result.

We can now clearly see that the damping coefficient has increased. When looking at the displacement figure, the numerical model's proof mass is slower to snap through than the experimental model. The bounce back after the first impact is still slightly higher, but it matches way better than the experimentally found damping coefficient. The model now only snaps two times compared to the three times with the lower damping coefficient. When looking at the total energy plot, it can again be seen that the numerical system is slower than the experimental system. However, the peak energy complies pretty well with the experimental peak energy.

A final step for the linear plot is to see the effect of changing the damping coefficient slightly. The damping coefficient, as found using experimental testing is increased and decreased by 10%. The resulting figure for the displacement is shown below.

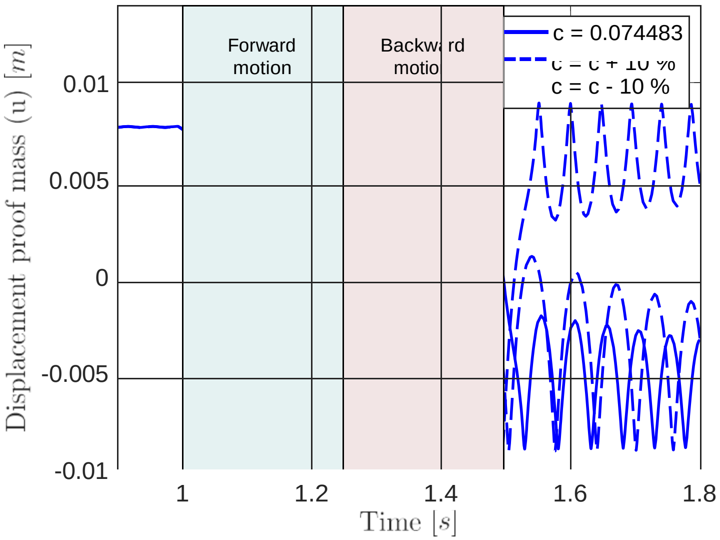

Figure G.5: Sensitivity analysis of linear damping, when the linear damping coefficient ($c = 0.074483 Ns/m$) is increased and decreased slightly.

From the figure above, the sensitivity of the damping can be seen. When the damping coefficient is increased slightly, it will snap back way faster. When the damping coefficient is decreased slightly, it will make an extra snap-through (resulting in five snaps, where the experimental model only showed 2). The linear damping is thus very prone to small errors.

G.3 Nonlinear damping cubic

As a next step, nonlinear damping in the form of cubic damping is added (see Eq. G.5). It was early noted by Rayleigh et al. [35] that linear damping is insufficient when investigating impulse behavior. He, therefore, proposed nonlinear cubic damping. The difficulty in nonlinear damping is finding the nonlinear damping coefficient. Elliot et al. [14] proposed a method to find the nonlinear damping coefficient for a linear system. However, we're dealing with a highly nonlinear system; nevertheless, it is worth trying. The equation results in a negative nonlinear damping coefficient of $c_3 = -0.0812$; however, it is taken as positive.

$$F_d = c_1 \dot{u} + c_3 \dot{u}^3 \tag{G.5}$$

$$c_1 + \frac{3}{4} c_3 \omega_0^2 X_0^2 = 0 \tag{G.6}$$

The system's resulting output when the nonlinear damping coefficient is set to $c_3 = 0.0812$ is shown below.

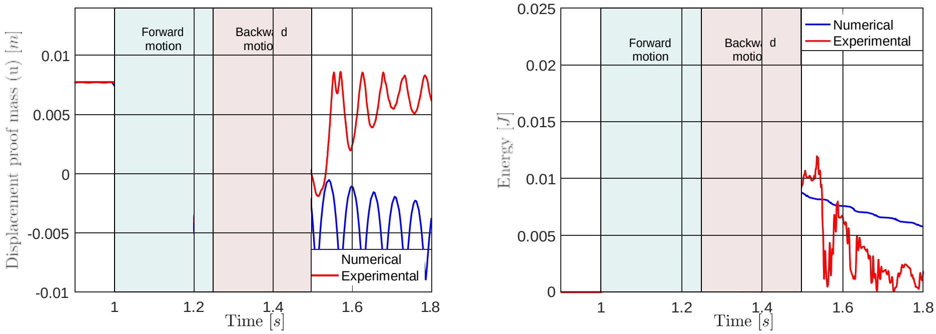

(a) Time displacement signal.

(b) Time energy signal.

Figure G.6: Results when using cubic damping with a linear damping coefficient of $c = 0.074483 Ns/m$ and a nonlinear damping coefficient of $c_3 = 0.0812$. The blue lines indicates the numerical result, the red line the experimental result.

It can be seen from the figure above that the influence of the cubic damping is negligible when using such a low factor. Elliot et al. already discussed that nonlinear systems require different nonlinear damping factors. This experiment confirms his statement. When looking at the nonlinear energy plot, the results are even worse than solely linear damping. There is a third energy spike due to snapping, which doesn't happen in experiments.

Since there is no right way of finding the cubic damping coefficient, it is simulated until it fits the experimental energy data. A new damping coefficient is found at $c_3 = 3$; the resulting displacement and energy plot are again shown below.

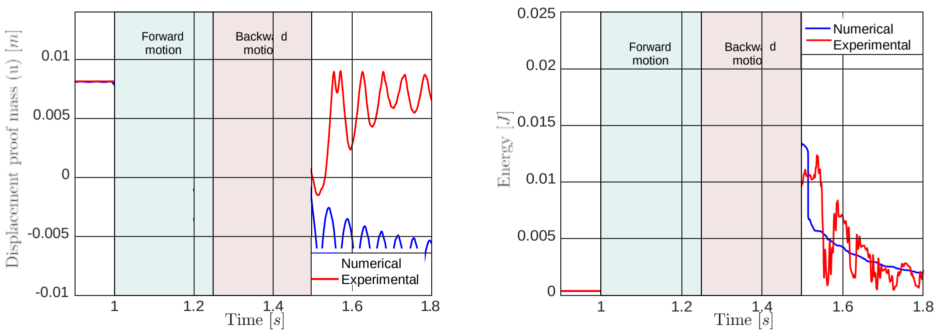

(a) Time displacement signal.

(b) Time energy signal.

Figure G.7: Results when using cubic damping with a linear damping coefficient of $c = 0.074483 Ns/m$ and a nonlinear damping coefficient of $c_3 = 3$. The blue lines indicates the numerical result, the red line the experimental result.

The new result again has the third snap; however, the overall fit is better. The amplitude of the bounce back after the impact is similar to the amplitude of the experimental model. However, one should note that the damping factor is set such that the results fit each other. Therefore the simulation is also compared to different experimental data, from which the total energy is plotted below.

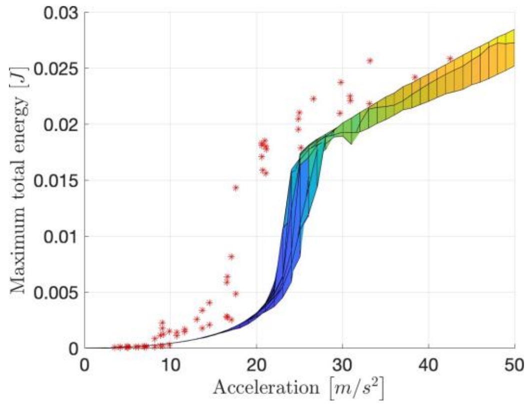

Figure G.8: Maximum total energy when performing a simulation with cubic damping ($c = 0.074483$, $c_3 = 3$), where experimental data is plotted using red dots.

The experimental data comply pretty well with the numerically found results. The difference in snapping acceleration is already discussed in chapter 4. However, one could note that this holds for this specific case; however, it is not clear how well it holds for different configurations.

The final step for cubic damping is to check the sensitivity of the system. The sensitivity analysis is done by changing the nonlinear damping coefficient slightly (increasing/ decreasing 10%).

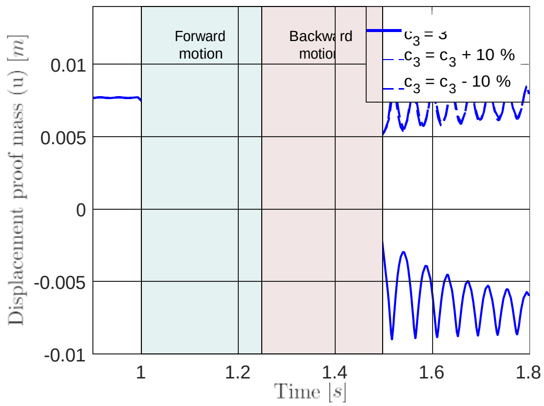

Figure G.9: Sensitivity analysis of cubic damping, when the nonlinear damping coefficient ($c = 0.074483 Ns/m$, $c_3 = 3$) is increased and decreased slightly. Changing the damping coefficient slightly has a great effect on which stable point it ends.

From figure G.9, it can be seen that the nonlinear damping factor is less sensitive. It does influence in which stable point it ends; however, the bounce back behavior and the snapping from one to another state are quite similar. It is interesting to note that only the middle nonlinear damping value snaps one time extra.

G.4 Coefficient of restitution

A method to calculate the behavior when snapping through can be done using the coefficient of restitution. The coefficient of restitution is usually used when the proof mass is hitting a solid object. A commonly used example is a ball bouncing on the floor. The coefficient of restitution describes the relation between the velocity when hitting the floor and the velocity when bouncing back. The coefficient of restitution is already calculated in the section above (see Sec. G.1.2) and found to be 0.74. When the proof mass hits the end stop, at, for example, 1 m/s, the rebound velocity is 0.74 m/s. The resulting figures for the displacement en total energy are shown below.

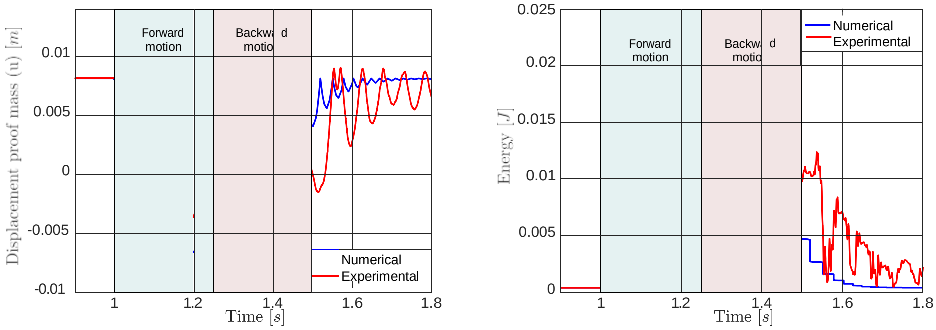

(a) Time displacement signal.

(b) Time energy signal.

Figure G.10: Results when using the coefficient of restitution (CoR = 0.74) with a linear damping $c = 0.074483 Ns/m$. The blue lines indicates the numerical result, the red line the experimental result.

The figure above already shows promising results compared to the linear model. It is beneficial compared to the cubic model since the coefficient of restitution of such a system can easily be measured. Only a laser sensor is necessary, and no dynamic testing has to be performed. Whenever the proof mass goes beyond the stable point, the motion is inverted with a velocity multiplied by the coefficient of restitution in the opposite direction. The motion calculated using the coefficient of restitution follows the experimental signal pretty well. Also, the peak energy levels seem to comply with the experimental data. Next, the sensitivity of the coefficient of restitution is investigated by increasing and decreasing the coefficient slightly.

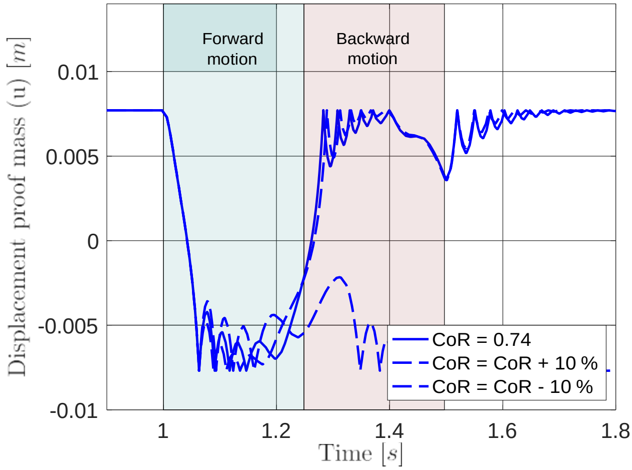

Figure G.11: Sensitivity analysis of coefficient of restitution, when the coefficient of restitution ($CoR = 0.74$) is increased and decreased slightly.

G.5 Bounce loss coefficient

The coefficient of restitution has some crucial drawbacks. The end stops in the systems, in real life, aren't infinitely stiff and can therefore be used to store energy. Take, for example, the displacement diagram in figure G.10. When the proof mass is decelerating in the forward motion, it will be pushed towards the end-stop (negative acceleration). This would mean the proof mass will be pressed in the spring's stiff part, storing energy in real life. However, using CoR, this isn't the case; it is pressed towards the end-stop, which is infinitely stiff, thus not storing potential energy.

Therefore, the bounce loss coefficient is proposed to overcome this problem, where the spring's behavior is conserved, but the principle of the coefficient of restitution is used. Instead of assuming the spring to be infinitely stiff after the stable point, the spring stiffness is used. However, when the proof mass passes beyond the stable point, the velocity is multiplied by the bounce loss coefficient. Below is a figure showing the working principle. The vertical lines indicate where the velocity is multiplied with the bounce loss coefficient. The horizontal line represents the stable point of the spring. Again, the same value as for the coefficient of restitution is used ($BLC = 0.74$).

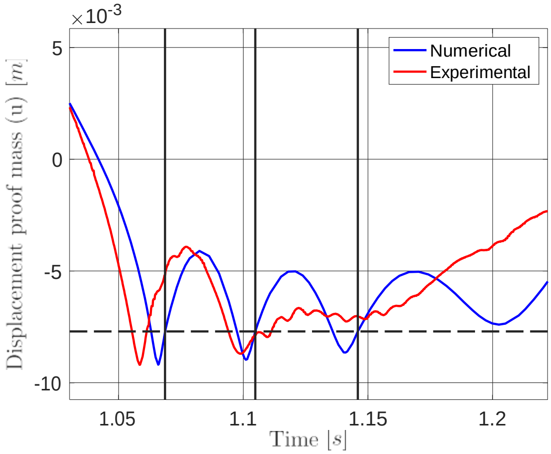

Figure G.12: Working principle of the bounce loss coefficient. The velocity is multiplied by the coefficient of restitution when passing the stable point of the nonlinear spring. The points where the bounce loss coefficient are applied can be seen by the vertical lines. The horizontal line indicates the stable point.

The new method results in the following displacement and energy curve.

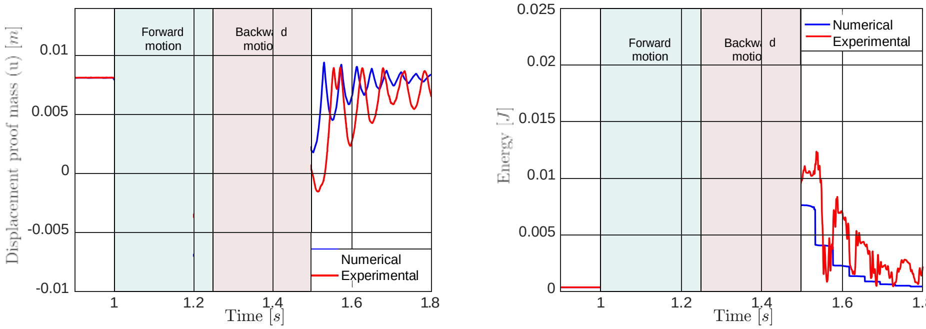

(a) Time displacement signal.

(b) Time energy signal.

Figure G.13: Results when using the bounce loss coefficient ($BLC = 0.74$) with a linear damping $c = 0.074483 Ns/m$. The blue lines indicates the numerical result, the red line the experimental result.

It can be seen from the figure above that the numerical model follows the experimental model better than using the standard coefficient of restitution (see Fig. G.10). The most significant difference is seen in the displacement and energy at the end of the backward motion. The displacement gets closer to the experimental model, and there is also a larger energy peak in the system. Unfortunately, the difference in peak energy is less significant. When only looking at the peak energy output, there is zero to no difference.

The next thing to do is determine its sensitivity to changes to the bounce loss coefficient.

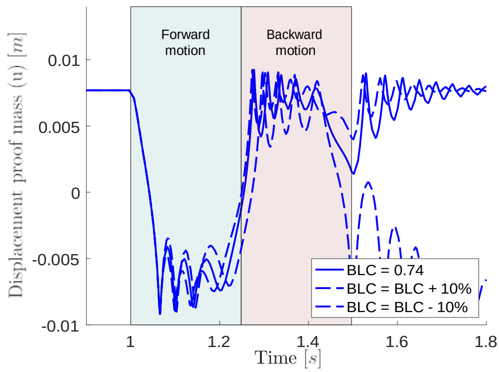

Figure G.14: Sensitivity analysis of the bounce loss coefficient, when the bounce loss coefficient ($BLC = 0.74$) is increased and decreased slightly.

As shown in the figure above, the sensitivity of the BLC seems, less than the CoR. The most significant difference can be seen when the coefficient of restitution is increased by 10%. However, this result is straightforward to explain. Since the coefficient of restitution is higher, it is rebounded with a slightly higher velocity. This higher velocity makes it snap to the other state. When looking at the experimental data, it can be seen that this example is just at the edge of snapping between states at the end of the backward motion. Only a small difference was necessary to snap it to the other state. This results complies with the experimental data, when the excitation is slightly increased, the oscillator snaps to the other state.

A final analysis is to see how close we can get the numerical model to the experimental model for both the CoR and the bounce loss coefficient. For both systems, the CoR/BLC is tuned until it matches the displacement signal as well as possible.

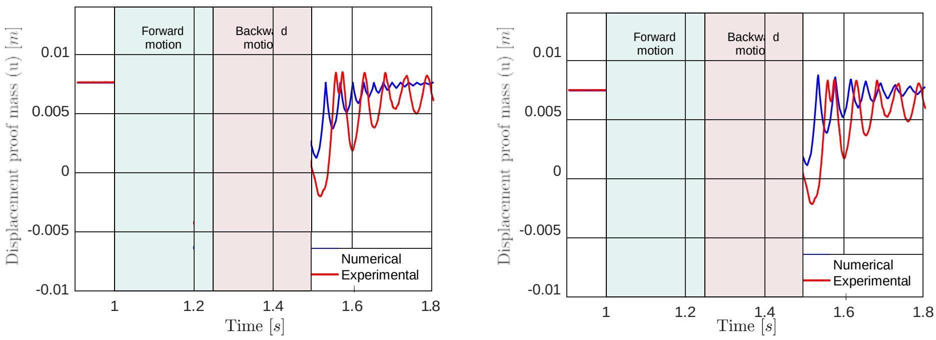

(a) Coefficient of restitution ($CoR = 0.7659$)

(b) Bounce loss coefficient ($CoR = 0.777$)

Figure G.15: Results when comparing the optimal case for the coefficient of restitution and the bounce loss coefficient.

During analysis, it was noted that it was easier to match the BLC than the CoR. The response of the BLC was way more predictable. When the BLC was slightly increased, the peak after the backward motion increased, which wasn't the case for the CoR. The value for the BLC was found to be + 5 %, while the adjusted CoR value was + 3.5 %.

G

Appendix H
Numerical model - parameter tuning

In addition to chapter 4, this appendix investigates the influence of the flexure's design parameters. The same methods, as discussed in chapter 4, is used to find the system's dynamics. The dynamics of the nonlinear oscillator are numerically calculated when moving according to a forced vibration.

First, the two different design parameters, alpha, and beta, will be introduced (H.1). Next, the influence of alpha and beta on the force-deflection curve will be shown (H.2). After that, the resulting dynamical behavior will be shown for different alpha and beta values (H.3). Finally, the found results will be discussed (H.4).

H.1 Design parameters

Two new parameters are introduced, alpha (α) and beta (β), which describe the relationship between design parameters used (see Fig. H.1). Alpha (α) describes the relationship between the spring's length (W_n) and the total flexure length ($W_w + W_n$). Beta (β) describes the relationship between the height of the narrow (H_n) and the wide area of the spring (H_w).

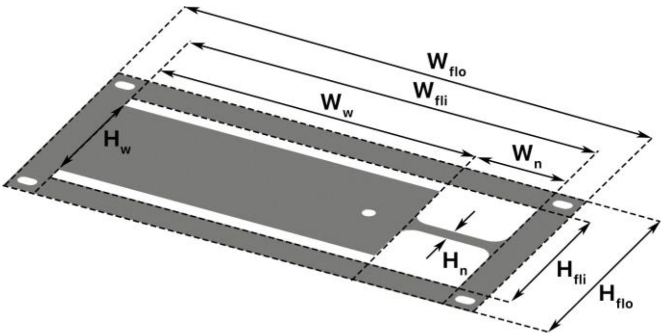

Figure H.1: Flexure when it is not preloaded with the relevant parameters.

$$\alpha = \frac{W_n}{W_w + W_n} \tag{H.1}$$

$$\beta = \frac{H_n}{H_w} \tag{H.2}$$

H.2 Mechanical behavior

The different configurations' force-deflection curve is calculated in the same manner as described in chapter 4.2.1. The parameter alpha is varied from 0.1792 to 0.2688 in 5 steps. The parameter beta is varied from 0.08 to 0.12 in 5 steps. By varying alpha and beta, the force-deflection curve changes, which are shown below.

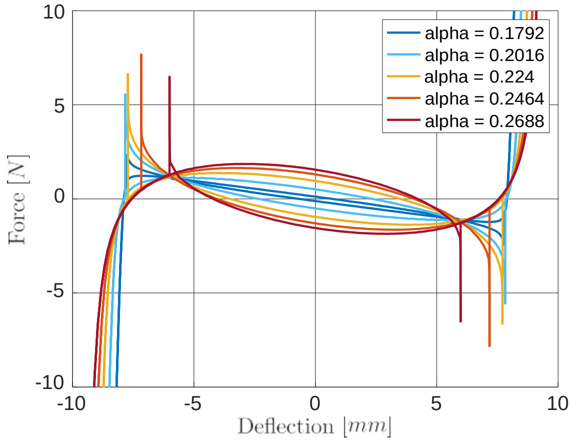

Figure H.2: Force deflection curve when tuning the alpha parameter. When alpha is increased the force needed to snap between two stable states increases as well. The stable point moves outward when decreasing alpha.

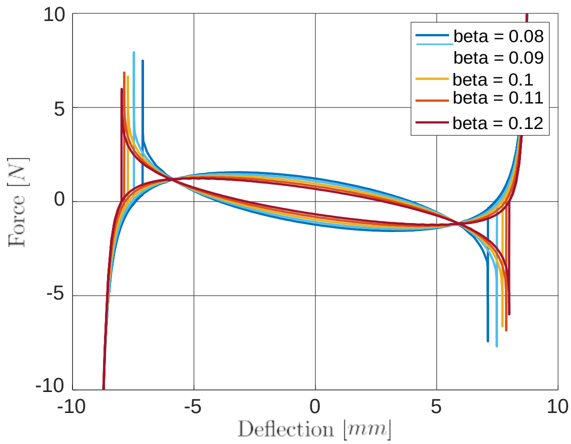

Figure H.3: Force deflection curve when tuning the beta parameter. When beta is increased the force needed to snap between two stable states decreases. The stable point moves outward when increasing beta.

H.3 Results

The alpha and beta parameters are tuned. The figure below shows the total energy for five different values of alpha. The figure below is a slice of the surface plot, as shown in figure H.4a for a large amplitude (amplitude = 1 m).

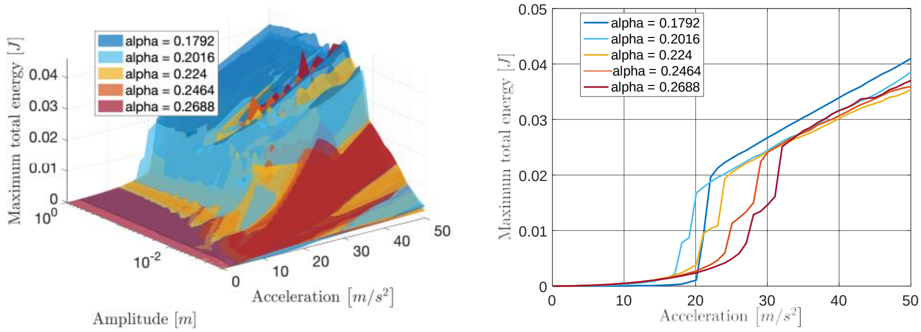

(a) Total energy levels for when the parameter alpha is tuned. By increasing the alpha factor, the peak energy output, and the bandwidth in the acceleration domain decreases. A larger alpha may be beneficial when looking at smaller amplitudes due to the smaller distance between the two stable points.

(b) Total energy levels for when the parameter alpha is tuned for a constant amplitude of 1 m. When alpha decreases, the acceleration bandwidth tends to broaden. However, it is important to note that it seems like there is an optimum for alpha in the acceleration bandwidth. The alpha factor 0.2016 has a larger bandwidth than alpha-factor 0.1792, however, with a lower energy level.

Figure H.4: Force-deflection curves for when parameter alpha and beta are tuned.

The figure below shows the total energy for five different values of beta. The figure below is a slice of the surface plot, as shown in figure H.5a for a large amplitude (amplitude = 1 m). The figure below is a slice of the surface plot, as shown in Fig. H.5a for a large amplitude (amplitude = 1 m).

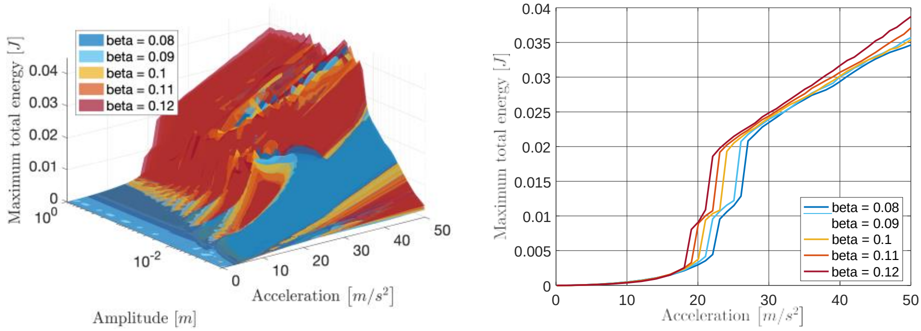

(a) Total energy levels for when the parameter beta is tuned. By increasing the beta factor, the peak energy output increases. When looking at low amplitudes a smaller beta may be beneficial, this may be due to the smaller distance between the two stable points.

(b) Total energy levels for when the parameter beta is tuned for a constant amplitude of 1 m. When beta is increased the acceleration bandwidth tends to be broader with a slightly higher energy output.

Figure H.5: Force-deflection curves for when parameter alpha and beta are tuned.

H

H.4 Discussion

The last step is to investigate what the influence of the alpha and beta factor is. For the discussion, both the force-deflection curves as discussed in appendix H.2 and the results in appendix. H.3 will be used. First, the influence of alpha will be discussed, after which the influence of beta will be discussed.

When alpha increases, the force to snap from one stable state to the other increases. A fair hypothesis would be that the variation where alpha is the lowest would be the first to snap; however, this does not seem to be the case. Alpha factor 0.2016 snaps with a lower acceleration than alpha 0.1792 (despite the lower force needed to snap between stable states). When the alpha increases further, the acceleration at which it snaps increases. Figure H.4b shows that a lower value for alpha may be beneficial. However, when looking at lower value amplitudes, a higher alpha value may be beneficial (see Fig. H.4a); this is probably due to the distance between the two stable points (see Fig. H.4b). When alpha increases, the distance between the two stable points decreases.

There is no apparent difference in the peak energy output for different alpha factors (not including alpha = 0.1792). This difference may be due to the trade-off between potential energy and kinetic energy. A higher alpha leads to a stiffer system. A less stiff system is likely to have more kinetic energy and less potential energy than its stiffer equivalent.

The influence of beta seems to be more simple. When beta is increased, the force necessary to snap between stable states decreases (see Fig. H.5b). This decrease in peak-force leads to less acceleration needed to snap in-between states. When beta is decreased, the relative velocity increases as well, leading to higher total energy. One thing to keep in mind is the system's fatigue; higher velocities may cause more significant impacts and, thus, fatigue in the flexure. When looking for an extensive bandwidth system in the acceleration domain, it is beneficial to increase beta (see Fig. H.5a).

Bibliography

[1] Abdelnaby, M. A. and Arafa, M. (2016). Energy harvesting using a flextensional compliant mechanism. *Journal of Intelligent Material Systems and Structures*, 27(19):2707–2718.

[2] Ahmad, M., Khairul Azwan, I., and Mat, F. (2016). Impact models and coefficient of restitution: A review.

[3] Ali, M., Nguyen gia, T., Taha, A.-E., Rahmani, A. M., Westerlund, T., Liljeberg, P., and Tenhunen, H. (2017). Autonomous patient/home health monitoring powered by energy harvesting.

[4] Ali, S. F. and Friswell, M. (2011). Analysis of energy harvesters for highway bridges. *Journal of Intelligent Material Systems and Structures - J INTEL MAT SYST STRUCT*, 22:1929–1938.

[5] Amin Karami, M. and Inman, D. J. (2012). Powering pacemakers from heartbeat vibrations using linear and nonlinear energy harvesters. *Applied Physics Letters*, 100(4):042901.

[6] Blad, T. W. and Tolou, N. (2019). On the efficiency of energy harvesters: A classification of dynamics in miniaturized generators under low-frequency excitation. *Journal of Intelligent Material Systems and Structures*, 30(16):2436–2446.

[7] Caliò, R., Rongala, U. B., Camboni, D., Milazzo, M., Stefanini, C., De Petris, G., and Oddo, C. M. (2014). Piezoelectric energy harvesting solutions. *Sensors*, 14(3):4755–4790.

[8] Caliò, R., Rongala, U. B., Camboni, D., Milazzo, M., Stefanini, C., De Petris, G., and Oddo, C. M. (2014). Piezoelectric Energy Harvesting Solutions. *Sensors*, 14(3):4755–4790.

[9] Cammarano, A., Neild, S., Burrow, S., Wagg, D., and Inman, D. (2014a). Optimum resistive loads for vibration-based electromagnetic energy harvesters with a stiffening nonlinearity. *Journal of Intelligent Material Systems and Structures*, 25(14):1757–1770.

[10] Cammarano, A., Neild, S. A., Burrow, S. G., and Inman, D. J. (2014b). The bandwidth of optimized nonlinear vibration-based energy harvesters. *Smart Materials and Structures*, 23(5):055019.

[11] Chen, G., Gou, Y., and Yang, L. (2010). Research on Multistable Compliant Mechanisms: The State of the Art. *Proceedings of the 9th International Conference on Frontiers of Design and Manufacturing (ICFDM 2010)*, pages 17–19.

[12] Daqaq, M., Renno, J., Farmer, J., and Inman, D. (2007). Effects of system parameters and damping on an optimal vibration-based energy harvester.

[13] Daqaq, M. F., Masana, R., Erturk, A., and Dane Quinn, D. (2014). On the Role of Nonlinearities in Vibratory Energy Harvesting: A Critical Review and Discussion. *Applied Mechanics Reviews*, 66(4).

[14] Elliott, S., Tehrani, M. G., and Langley, R. (2015). Nonlinear damping and quasi-linear modelling. *Philosophical Transactions of the Royal Society A: Mathematical, Physical and Engineering Sciences*, 373(2051):20140402.

[15] Erturk, A., Hoffmann, J., and Inman, D. J. (2009). A piezomagnetoelastic structure for broadband vibration energy harvesting. *Applied Physics Letters*, 94(25):254102.

[16] Erturk, A. and Inman, D. J. (2011). Broadband piezoelectric power generation on high-energy orbits of the bistable Duffing oscillator with electromechanical coupling. *Journal of Sound and Vibration*, 330(10):2339–2353.

[17] Fan, K., Zhang, Y., Liu, H., Cai, M., and Tan, Q. (2019). A nonlinear two-degree-of-freedom electromagnetic energy harvester for ultra-low frequency vibrations and human body motions. *Renewable Energy*, 138:292–302.

[18] Galchev, T., Kim, H., and Najafi, K. (2011). Micro Power Generator for Harvesting Low-Frequency and Nonperiodic Vibrations. *Journal of Microelectromechanical Systems*, page 5961600.

[19] Geisler, M., Boisseau, S., Perez, M., Gasnier, P., Willemin, J., Ait-Ali, I., and Perraud, S. (2017). Human-motion energy harvester for autonomous body area sensors. *Smart Materials and Structures*, 26(3):035028.

[20] Gupta, R. K., Shi, Q., Dhakar, L., Wang, T., Heng, C. H., and Lee, C. (2017). Broadband energy harvester using non-linear polymer spring and electromagnetic/triboelectric hybrid mechanism. *Scientific reports*, 7:41396.

[21] Harne, R. L. and Wang, K. (2013a). A review of the recent research on vibration energy harvesting via bistable systems. *Smart materials and structures*, 22(2):023001.

[22] Harne, R. L. and Wang, K. W. (2013b). A review of the recent research on vibration energy harvesting via bistable systems. *Smart Materials and Structures*, 22(2):023001.

[23] Hui Fang, L., Hassan, S., Abd Rahim, R., and AbdulMalek, M. (2016). A study of vibration energy harvester. 11:5028–5041.

[24] Kamalinejad, P., Mahapatra, C., Sheng, Z., Mirabbasi, S., Leung, V. C., and Guan, Y. L. (2015). Wireless energy harvesting for the internet of things. *IEEE Communications Magazine*, 53(6):102–108.

[25] Karami, M. A. and Inman, D. J. (2011). Equivalent damping and frequency change for linear and nonlinear hybrid vibrational energy harvesting systems. *Journal of Sound and Vibration*, 330(23):5583 – 5597.

[26] Khan, F. U. and Iqbal, M. (2016). DEVELOPMENT OF A TESTING RIG FOR VIBRATION AND WIND BASED ENERGY HARVESTERS. 35(2):10.

[27] Kwon, S.-D., Park, J., and Law, K. (2013). Electromagnetic energy harvester with repulsively stacked multilayer magnets for low frequency vibrations. *Smart Materials and Structures*, 22(5):055007.

[28] Li, H., Tian, C., and Deng, Z. D. (2014). Energy harvesting from low frequency applications using piezoelectric materials. *Applied physics reviews*, 1(4):041301.

[29] Mainwaring, A., Culler, D., Polastre, J., Szewczyk, R., and Anderson, J. (2002). Wireless sensor networks for habitat monitoring. In *Proceedings of the 1st ACM international workshop on Wireless sensor networks and applications*, pages 88–97.

[30] Mann, B. and Sims, N. (2009). Energy harvesting from the nonlinear oscillations of magnetic levitation. *Journal of sound and vibration*, 319(1-2):515–530.

[31] Nguyen, D. S. and Halvorsen, E. (2010). Analysis of vibration energy harvesters utilizing a variety of nonlinear springs. *Proc. Power MEMS*, 10:331–334.

[32] Oumbé Tékam, G. T., Kitio Kwuimy, C. A., and Woafo, P. (2015). Analysis of tristable energy harvesting system having fractional order viscoelastic material. *Chaos: An Interdisciplinary Journal of Nonlinear Science*, 25(1):013112.

[33] Park, G., Rosing, T., Todd, M. D., Farrar, C. R., and Hodgkiss, W. (2008). Energy harvesting for structural health monitoring sensor networks. *Journal of Infrastructure Systems*, 14(1):64–79.

[34] Penella, M. and Gasulla, M. (2007). A review of commercial energy harvesters for autonomous sensors. pages 1 – 5.

[35] Rayleigh, J. W. S. (1945). *The Theory of Sound, Volume One*. Dover Publications, 2 edition. Section 68a.

[36] Riemer, R. and Shapiro, A. (2011). Biomechanical energy harvesting from human motion: theory, state of the art, design guidelines, and future directions. *Journal of neuroengineering and rehabilitation*, 8(1):22.

[37] Ross, P. E. (2004). Managing care through the air [remote health monitoring]. *IEEE spectrum*, 41(12):26–31.

[38] Safaei, M., Sodano, H. A., and Anton, S. R. (2019). A review of energy harvesting using piezoelectric materials: state-of-the-art a decade later (2008–2018). *Smart Materials and Structures*, 28(11):113001.

[39] Stanton, S. C., McGehee, C. C., and Mann, B. P. (2009). Reversible hysteresis for broadband magnetopiezoelastic energy harvesting. *Applied Physics Letters*, 95(17):174103.

[40] Su, W.-J., Zu, J., and Zhu, Y. (2014). Design and development of a broadband magnet-induced dual-cantilever piezoelectric energy harvester. *Journal of Intelligent Material Systems and Structures*, 25(4):430–442.

[41] Tang, L., Yang, Y., and Soh, C.-K. (2012). Improving functionality of vibration energy harvesters using magnets. *Journal of Intelligent Material Systems and Structures*, 23(13):1433–1449.

[42] Toprak, A. and Tigli, O. (2014). Piezoelectric energy harvesting: State-of-the-art and challenges. *Applied Physics Reviews*, 1(3):031104.

[43] Vullers, R. J. M., v. Schaijk, R., Visser, H. J., Penders, J., and Hoof, C. V. (2010). Energy harvesting for autonomous wireless sensor networks. *IEEE Solid-State Circuits Magazine*, 2(2):29–38.

[44] Wang, W., Cao, J., Bowen, C. R., Zhou, S., and Lin, J. (2017). Optimum resistance analysis and experimental verification of nonlinear piezoelectric energy harvesting from human motions. *Energy*, 118:221 – 230.

[45] Williams, C., Shearwood, C., Harradine, M., Mellor, P., Birch, T., and Yates, R. (2001). Development of an electromagnetic micro-generator. *IEE Proceedings-Circuits, Devices and Systems*, 148(6):337–342.

[46] Wu, X., Lin, J., Kato, S., Zhang, K., Ren, T., and Liu, L. (2008). A frequency adjustable vibration energy harvester. *Proceedings of PowerMEMS*, pages 245–248.

[47] Yang, Z., Zhou, S., Zu, J., and Inman, D. (2018). High-performance piezoelectric energy harvesters and their applications. *Joule*, 2(4):642–697.

[48] Yi, Z., Yang, B., Li, G., Liu, J., Chen, X., Wang, X., and Yang, C. (2017). High performance bimorph piezoelectric mems harvester via bulk pzt thick films on thin beryllium-bronze substrate. *Applied Physics Letters*, 111(1):013902.

[49] Zhang, H., Xi, R., Xu, D., Wang, K., Shi, Q., Zhao, H., and Wu, B. (2019). Efficiency enhancement of a point wave energy converter with a magnetic bistable mechanism. *Energy*, 181:1152–1165.

[50] Zhang, Y., Zheng, R., Shimono, K., Kaizuka, T., and Nakano, K. (2016). Effectiveness Testing of a Piezoelectric Energy Harvester for an Automobile Wheel Using Stochastic Resonance. *Sensors*, 16(10):1727.

[51] Zhou, Z., Qin, W., Yang, Y., and Zhu, P. (2017a). Improving efficiency of energy harvesting by a novel penta-stable configuration. *Sensors and Actuators A: Physical*, 265:297–305.

[52] Zhou, Z., Qin, W., and Zhu, P. (2017b). A broadband quad-stable energy harvester and its advantages over bi-stable harvester: Simulation and experiment verification. *Mechanical Systems and Signal Processing*, 84:158–168.

[53] Zhu, D., Tudor, M. J., and Beeby, S. P. (2009). Strategies for increasing the operating frequency range of vibration energy harvesters: a review. *Measurement Science and Technology*, 21(2):022001.